



**Computational Generation of Wear maps
for H13 Tool steel in Open die Hot forging**

BY

JAMES MARASHI

This thesis presented in fulfillment of the requirements for
the degree of

Doctorate in Engineering (EngD)

Advanced Forming Research Centre
Department of Design, Manufacture & Engineering
Management University of Strathclyde
Glasgow, Scotland, UK

Declaration

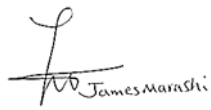
I declare that this submission is entirely my own original work.

I declare that, except where fully referenced direct quotations have been included, no aspect of this submission has been copied from any other source.

I declare that all other works cited in this submission have been appropriately referenced.

I understand that any act of academic dishonesty such as plagiarism or Collusion may result in the non-award of my degree.

Signed:

A handwritten signature in black ink, appearing to be 'James Marashi', with a stylized flourish above the name.

Date: 09/04/19

Acknowledgment

I praise God for all his mercy and grace throughout my life. I would like to thank Professor Xirouchakis, Dr. Zante my supervisors, Jim Foster who helped me throughout the project. I also would like to thank Dr. Yakushina, Liza Hall, for all their technical inputs and Professor Corney, Professor Xichun Luo, Jillian McBryde, Pamela Peacock, Pamela Marshal and Caroline McGuire and all my fellow EngD colleague for their help and advice. Special thank you to Dr. Evans EngD coordinator and all the university and AFRC staff (especially machining and forging team at the AFRC for all their support to make this possible). I would like to offer this to my wonderful fiancée Sophie Stockwell-Marsh, my siblings, loved ones and close friends for all their support and prayers. This work was supported by High-Value Manufacturing Catapult (The Oracle Building, Blythe Valley Business Park, Shirley, Solihull, B90 8AD) established by the Innovate UK through grant 160051, at the Advanced Forming Research Centre, University of Strathclyde (85 Inchinnan Drive, Renfrewshire, PA4 9LJ, United Kingdom).

Abstract

Forging tools are associated with as much as 40% of the costs any forging operation and consequently understanding the causes of their failure is key to improving productivity. The literature suggests that wear is responsible for 70% of failures in hot forging with abrasive and adhesive wear being the main failure modes in open die forging.

Understanding the modes and mechanisms with which wear occurs on worn surfaces and contact faces is essential to minimise or eliminate the product defects and improve the quality. Tool wear phenomena can be understood and represented by wear maps for different materials (generated using a lab-based pin on disc). Such maps illustrate the wear mechanisms and wear progress from mild to transition and severe.

However, some researchers prefer to explain wear behavior using analytical methods instead of empirical wear map. This thesis argues that, firstly, the pin on disc method, often used to generate wear maps, is not reliable, and produces many errors and is not representative of the industrial process. Secondly, wear maps created from a mathematical model alone (i.e. without physical trial cannot truly capture the wear characteristic of the material. As an alternative, this thesis presents a series of abrasive and adhesive wear maps created using modified Archard mathematical model that is validated with a series of physical forging trials.

The Archard mathematical model subroutine was embedded in the DEFORM FE simulation software. A series of FE simulations implemented a full factorial design of experiment with furnace temperature and energy in the screw press as the main variables. The FEA results were validated with a series of physical trials. A similar experiment was repeated after nitriding the tool by 0.1mm case depth. The comparison between the FE simulations and physical trials showed a good correlation of 80-90% for abrasive wear on un-nitrided tools and 70-84% on nitrided tools. While the correlation of 80-85% for adhesive wear on un-nitrided tools and 70-85% on nitrided tools was achieved. These comparisons then were used to produce a series of wear maps.

This novel method of wear map generation can be used to optimise H13 tool steel performance and make the manufacturing process more cost effective. The optimised and predicted wear conditions help to minimise tool wear and improve the quality of obtained parts. Designer by having all the information using FE simulation alongside the wear maps can make the right decision in design and material selection. Potentially this methodology could also be used to compare different die materials, lubricants, and coatings.

Contents

Declaration.....	1
Acknowledgment.....	2
Abstract.....	3
Contents	4
List of Tables	7
List of Figures.....	8
Appendix Figures.....	11
List of Abbreviation.....	13
Chapter 1 Introduction.....	14
1.1.1. Precision forging process design	17
1.1.2. Precision forging process classification.....	18
1.1.3. Die selection based on material properties	21
1.1.4. Tool failure	23
1.1.5. Aim and objective.....	25
1.1.6. Scope.....	27
1.2. Research contribution	28
1.2.1. Tool failure analysis.....	28
1.2.2. Wear model development	28
1.2.3. Tool failure measurement method	28
1.2.4. Wear map construction	29
1.2.5. Die life prediction	29
Chapter 2 Literature review.....	30
2.1. Die Wear Mechanism and Models.....	30
2.1.1. Abrasive wear	31
2.1.2. Adhesion wear	32
2.1.3. Parameters influencing wear.....	33
2.1.4. Tool plastic deformation.....	35
2.1.5. Different wear models in addition to Archard model	36
2.1.6. . Wear map generation	39

2.2.	Tooling material and Coating	42
2.2.1.	Heat treatment.....	42
2.2.2.	Nitriding.....	44
2.2.3.	Gas nitriding	46
2.2.4.	Plasma nitriding	47
2.2.5.	Ion nitriding and Nitrogen Ion implantation	47
2.2.6.	Surface coating	48
2.2.7.	Additive layering	50
2.3.	Discussion.....	51
Chapter 3	Research Methodology	53
3.1.	Experimental Equipment and wear model implementation.....	55
3.1.1.	Wear model.....	56
3.1.2.	Tool design	58
3.1.3.	FE Simulation	59
3.1.4.	The methodology behind adhesive wear Subroutine	61
3.1.5.	Metrology wear measurement technique	62
3.1.1.	Press kinetics.....	62
3.1.1.	Thermal Camera imaging	63
3.2.	Experimental tooling and materials	64
3.2.1.	Forging of Stainless steel 321	64
3.2.2.	Forging of Inconel 718.....	67
3.2.3.	H13 Die material properties.....	69
3.2.4.	Die material surface treatment	71
3.2.5.	Lubricant,.....	71
3.2.6.	Heat transfer and Friction	71
3.3.	Experimental procedure	72
3.3.1.	Wear model calibration.....	72
3.3.1.	Forging trials steps.....	73
3.3.2.	Stainless steel 321 trials.....	74
3.3.3.	Inconel 718 trials	85
3.3.4.	Comparing Simulation wear prediction result to the Practical Wear Measurement.....	89
3.3.5.	H13 Tool Deformation.....	90
3.3.6.	Tool design change	96

3.3.7.	Wear map trials	97
3.3.8.	Wear map construction	100
3.3.9.	Nitrided and coated trials	101
Chapter 4	Results.....	106
4.1.	Tool Deformation	106
4.1.1.	XRF (X-ray fluorescence).....	106
4.1.2.	Simulation.....	106
4.1.3.	Microstructure analysis.....	110
4.1.4.	Process Improvement.....	116
4.1.5.	Abrasive and Adhesive Wear Maps Analysis.....	120
Chapter 5	Discussion and Conclusion	129
5.1.	A computational process for the generation of wear model	129
5.2.	Identification of H13 tool steel failure modes when forging Inconel 718	130
5.3.	Experimental Validation of the proposed wear model.....	130
5.4.	Characterisation of H13 die material	130
5.5.	Development of a repeatable measurement methodology for wear.....	131
5.6.	Limitations of the computationally generate wear maps	131
5.7.	Conclusion	132
5.8.	Future work.....	134
Chapter 6	References.....	135
Chapter 7	Appendix.....	146
7.1.	Appendix A.....	146
7.1.1.	Wear Subroutine	146
7.2.	Appendix B.....	165
7.2.1.	Abrasive and adhesive wear comparison between simulation prediction results and practical measurements using Coordinate measurement machine (on tools without nitriding layer).	165
7.2.2.	Abrasive and adhesive wear comparison between simulation prediction results and practical measurements using Coordinate measurement machine (on nitrided tools).....	174
7.3.	Appendix C.....	184
7.3.1.	Certificates of conformity and material data from the supplier	184

List of Tables

Table 3-1: List of experiments for wear map generation.....	55
Table 3-3: Chemical composition of Stainless steel 321 from COC	66
Table 3-4 :Chemical composition of Inconel 718 from COC.....	67
Table 3-5: Chemical composition of H13 tool steel from COC	69
Table 3-6:Full factorial design of experiments for 321stainless steel trial	74
Table 3-6 Full factorial design of experiments for 321stainless steel trial	75
Table 3-7: The maximum and minimum values from both the CAD and cylinder comparison The tolerances were set at +/-0.05mm as no tolerance has been defined for the parts.....	84
Table 3-9: Full factorial design of experiments	85
Table 3-9: Grinding and polishing steps used to prepare the samples.....	94
Table 3-11:Full factorial design of experiments for wearmap construction.....	97
Table 3-11: DOE plan for wear map construction.....	100
Table 4-1:H13 chemical composition after forging (Wt.%).....	106
Table 4-2: H13 chemical composition (wt.%) from certificate of conformity (COC) compared to the result of X-ray fluorescence analysis.	116
Table 4-3: Five additional abrasive wear were measured by running five additional simulations to fill the empty area of scatter plot.....	121
Table 4-4: Nine adhesive wear values were predicted by the wear model which were compared to the CMM measurement . It showed 16- 23 % error. Then three additional simulations (A-C) was executed to increase the wear map coverage	123
Table 4-5: Nine abrasive wear values measured by the wear model for the nitrided tool . It then was compared to the CMM measurement which indicates 16- 30 % difference between the measured wear values using these two methods.....	125
Table 4-6:Abrasive wear values for four additional simulations.....	125
Table 4-7: Nine adhesive wear values were predicted by the wear model for nitrided tool. It then was compared to the CMM measurement which showed 15- 34 % error.....	127
Table 4-8: Adhesive wear values for four additional simulations on the nitrided tools .	127

List of Figures

Figure 1-1 Hardnes of H series tool steel at different temperatures [81]	22
Figure 1-2:Transition wear map	24
Figure 1-3: Wear Mechanism Map [31]	25
Figure 1-4: Scope of Research.....	27
Figure 2-1: Factors influencing wear and deformation failures [43]	34
Figure 2-2: Fe-C Diagram for steel[66]	43
Figure 2-3: H13 heat treatment procedure	44
Figure 2-4: Iron -Nitrogen diagram[68].....	45
Figure 2-5: Stress strain curves of nitrided steels AISI 4140[70].....	46
Figure 2-6: Approximate relative cost of surface treatment[76].....	49
Figure 3-1: Diagram illustrating the research methodology	53
Figure 3-2 : Four Piece die set consisting of Top die, Bottom die, Insert (with fillet radius of 1.5 mm) and End stop.....	58
Figure 3-3: Tensile sample dimensions [49].....	60
Figure 3-4: a)Screw press schematic b)2100 tonnes Schuler screw press (AFRC).....	63
Figure 3-5: Ark Thermal camera for 200 forging cycles	64
Figure 3-6: Flow stress curve for stainless steel 321 at 950 °C and strainrates of.....	66
Figure 3-7: Flow stress curve for inconel 718 a) 900 °C forging temperature b) 950°C forging temperature c)1000 °C forging temperature d) 1050°C forging temperature e) 1100°C forging temperature f)1150 °C forging temperature and all are at strainrates ranges between 0.001-100 s ⁻¹ [88]	68
Figure 3-8: Tensile test at 250,500 °C temperature and strain rates of 0.01,0.1 s ⁻¹	70
Figure 3-9: Wear model calibration steps	73
Figure 3-10: Forging trial steps	74
Figure 3-11:Fixture for Scanning an insert on Infocus Optical Microscope	77
Figure 3-12: Manual and automated alignments (3 points alignments).....	78
Figure 3-13 :Auto alignments, looped three times and used for measurement of dimples78	
Figure 3-14:An example of repeating scanning of the same part for 3 times without moving the part	79
Figure 3-15: Insert fixed on CMM table with indication of the area of interest.....	80
Figure 3-16: H13 Tool Temperature profile during the measurement.....	80
Figure 3-17:Variation for all 17 parts which were overlayed.....	81

Figure 3-18: The maximum deviation on both sides of the cylinder comparison	82
Figure 3-19: Two ways of calculating maximum and minimum deviation to CAD model	82
Figure 3-20: Thermal change of 321 Stainless steel billets during the CMM measurements.....	83
Figure 3-21: Notch area which was scanned by 0.7 mm CMM's probe	84
Figure 3-22: Tensile sample dimensions [49].....	87
Figure 3-23: Inconel 718 billet thermal change during CMM measurements	89
Figure 3-24: Four Piece die set consisting of Top die, Bottom die, Insert (with fillet radius of 1.5 mm) and End stop.....	91
Figure 3-25: a) Insert image before forging, b) Insert image after forging showing evidence of deformation and adhesion, c) magnified area of the deformation and adhesion	92
Figure 3-26: a) Fillet on the insert which was cut using EDM b) Interested area on the sample	94
Figure 3-27: Schematic of patterns for micro-hardness test	96
Figure 3-28: a) 1.5mm insert b) 2mm insert	96
Figure 3-29. a) CMM Scanning direction on the billet after a forging trial (1050°C billet temperature and 8KJ energy on Screw press); b) CMM analysis aligning carried out for billets 5, 10, 15, 20, 25 which were aligned to the billet 1.	99
Figure 3-30: Nitrided tensile sample dimension.....	101
Figure 3-31 a) Picture of cross section b) Hardness on nitrided tensile samples at different tensile test temperature	102
Figure 3-32: Nitrided Stress strain curves at temperature range of 230-400 °C	102
Figure 3-33: Flow curve comparison between nitrided and un-nitrided H13 tool steel at the temperature range of 230°C-400°C and strain rates of 0.001 ^{s⁻¹} and 0.01 ^{s⁻¹}	104
Figure 3-34: Nitrided tensile sample cross section	105
Figure 4-1: One point was selected with maximum stress concentration and high plastic strain of 0.38 on Deform 3D simulation post processor	106
Figure 4-2: Land thermal camera results at emissivity of 0.8 (±2 °C accuracy) for 200 cycles of forging (0.035 s for each cycle).....	107
Figure 4-3: a) The tensile test at a strain rate 0.1s ⁻¹ and 400 °C b) The result after extrapolation to 0.5 strain using power law for the same tensile test.	108
Figure 4-4: Effective stress results from the simulation: an elastoplastic model shows that the yield stress of H13 tool steel was exceeded during forging.....	108

Figure 4-5: BSE images were taken from the H13 tool samples: a) Before forging, b) After forging	110
Figure 4-6: BSE images of different zones 1) deformation zone, 2) transition between deformation and recrystallization zone, 3) recrystallization zone, 4) transition between recrystallization zone and martensitic zone, 5) martensitic zone.....	111
Figure 4-7 : a) IPF (Inverse pole figure) map which was obtained for the sample before forging, b) misorientation angles distribution histogram for the sample before forging, c) CSL (coincident site lattice) special boundaries distribution histogram for the sample before forging.	112
Figure 4-8: a) IPF (Inverse pole figure) map which was obtained for the sample after forging, b) misorientation angles distribution histogram for the sample after forging, c) CSL (coincident site lattice) special boundaries distribution histogram for the sample after forging.	114
Figure 4-9: a) The colour map showing change of microhardness in different zones using Origin software and b) Comparison between microhardness levels achieved on before forging and after forging samples.	116
Figure 4-10: Fish bone analysis for H13 insert deformation	117
Figure 4-11: Comparison in wear induced using insert with different radius.....	118
Figure 4-12: Effective stress comparison for both 1.5mm and 2mm fillet Inserts	119
Figure 4-13: a) The colour map showing change of microhardness in different zones for R=1.5 mm insert and b) The colour map showing change of microhardness in different zones for R=2 mm	119
Figure 4-14: Abrasive wear for un-nitrided tool.....	122
Figure 4-15: Adhesive wear for un-nitrided tool	124
Figure 4-16 : Abrasive wear on nitrided tool.....	126
Figure 4-17: Adhesive wear on nitrided tool	128

Appendix Figures

Figure 7-1 CMM measurement and simulation prediction comparison at 1050 °C furnace temperature and 5% of energy on screw press(8KJ) for abrasive and adhesive wear (Un-nitrided tool)	165
Figure 7-2. CMM measurement and simulation prediction comparison at 1050 °C furnace temperature and 7% of energy on screw press(11.2 KJ) for abrasive and adhesive wear (Un-nitrided tool)	166
Figure 7-3. CMM measurement and simulation prediction comparison at 1050 °C furnace temperature and 10% of energy on screw press(16KJ) for abrasive and adhesive wear (Un-nitrided tool)	167
Figure 7-4. CMM measurement and simulation prediction comparison at 1085 °C furnace temperature and 5% of energy on screw press (8KJ)for abrasive and adhesive wear (Un-nitrided tool)	168
Figure 7-5. CMM measurement and simulation prediction comparison at 1085 °C furnace temperature and 7%(11.2KJ) of energy on screw press for abrasive and adhesive wear (Un-nitrided tool)	169
Figure 7-6. CMM measurement and simulation prediction comparison at 1085 °C furnace temperature and 10 % of energy on screw press(16KJ) for abrasive and adhesive wear (Un-nitrided tool)	170
Figure 7-7. CMM measurement and simulation prediction comparison at 1120°C furnace temperature and 5 % of energy on screw press (8KJ)for abrasive and adhesive wear (Un-nitrided tool)	171
Figure 7-8. CMM measurement and simulation prediction comparison at 1120°C furnace temperature and 7 % of energy on screw press(11.2KJ) for abrasive and adhesive wear (Un-nitrided tool)	172
Figure 7-9. CMM measurement and simulation prediction comparison at 1120°C furnace temperature and 10 % of energy on screw press (16KJ)for abrasive and adhesive wear (Un-nitrided tool)	173
Figure 7-10. CMM measurement and simulation prediction comparison at 1050°C furnace temperature and 5 % of energy on screw press (8 KJ) for abrasive and adhesive wear (Nitrided tool)	174
Figure 7-11.CMM measurement and simulation prediction comparison	175
Figure 7-12. CMM measurement and simulation prediction comparison	176
Figure 7-13. CMM measurement and simulation prediction comparison at 1085°C furnace temperature and 5 % of energy on screw press (8 KJ) for abrasive and adhesive wear (Nitrided tool)	178
Figure 7-14. CMM measurement and simulation prediction comparison at 1085°C furnace temperature and 7 % of energy on screw press (11.2 KJ) for abrasive and adhesive wear (Nitrided tool)	179
Figure 7-15. CMM measurement and simulation prediction comparison at 1085°C furnace temperature and 10 % of energy on screw press (16 KJ) for abrasive and adhesive wear (Nitrided tool)	180

Figure 7-16. CMM measurement and simulation prediction comparison at 1120°C furnace temperature and 5 % of energy on screw press (8 KJ) for abrasive and adhesive wear (Nitrided tool)	181
Figure 7-17. CMM measurement and simulation prediction comparison at 1120°C furnace temperature and 7 % of energy on screw press (11.2 KJ) for abrasive and adhesive wear (Nitrided tool)	182
Figure 7-18. CMM measurement and simulation prediction comparison at 1120°C furnace temperature and 10 % of energy on screw press (16 KJ) for abrasive and adhesive wear (Nitrided tool)	183
Figure 7-19. Certificate of Conformity for Stainless steel 321.....	184
Figure 7-20. Stainless steel 321 material data from the supplier	185
Figure 7-21. Certificate of conformity for Inconel 718	186
Figure 7-22. Inconel 718 Material data sheet from the supplier.....	187
Figure 7-23. Certificate of conformity for H13 Tool steel	188
Figure 7-24. H13 Material data sheet from supplier	189

List of Abbreviation

K	Dimensionless wear coefficient	m	Shear friction coefficient
μ	Friction coefficient	T	Temperature
P	Contact pressure	σ_y	Yield strength
$\bar{\sigma}$	Flow stress	HV	Vickers hardness
$\bar{\epsilon}$	Effective plastic strain	W	Wear depth
V	Sliding velocity	L	Sliding distance
t, Δt	Contact time (duration of the test)	d_{fin}	Final wear amount
H	Hardness	w	Wear rate
v	Average surface roughness	N	Load
L	Sliding distance	ΔwR	Weight change of Roller

Chapter 1 **Introduction**

Metal forging and forming refer to a group of manufacturing methods by which the given material is transformed into a useful part without a change in the mass or composition of the material. Forging and forming processes are used together with other manufacturing processes such as machining, grinding, and heat treating, to complete the transformation of the raw material to the finished product. The properties are affected by temperature and strain rate. When ductility of material increases by an increase of temperature, yield strength decreases. In cold forming and forging yield stress increases with strain while in hot forming and forging it increases with strain rate. In a simple term forging is a process of plastically deforming a billet between two dies to produce the final product. However, the interaction between the billet and the die is very complicated. The metal flow, friction between tool and billet material interface, the heat generation and transfer during plastic flow, the relationship between process condition and microstructure properties are difficult to predict [5].

Forging is a term that can be used to describe a wide variety of bulk metalworking processes, and forging engineers must consider a variety of workability tests to diagnose forging problems for a wide range of forging operations. The forging process consists of compressive deformation of a piece of metal, the workpiece, between a pair of dies. The manufacturing involved in nearly all mass production requires die and molds, which are used in processes such as injection processing, casting, stamping and forging. However, some of the processes, such as incremental sheet forming, use tools and CNC machines instead of die. Dies and molds, as well as tools, might represent a small amount of investment compared to the value of production, but they are crucial in estimating the costs and quality of products as well as lead times [6]. The main advantage of precision forging over conventional forging is lower material consumption (about 60%) which is due to lack of flash and the fact that part requires minimum machining [7]. The main

disadvantage of the hot and warm die-forging process is that the tools are exposed to high thermal and mechanical stresses. These stresses cause failure of the dies mainly because of wear[8].

Die trial is another crucial factor which can determine the feasibility and lead time of an entire production. This can tie up the production line, so it is very important that this is examined from all different angles. For example, in car manufacturing, for interior components, the complex molds that are used can cost over £300,000 and six to nine months are needed for trial and robust process development using production parts. Given that OEM needs sample parts as well, it is necessary to list the range of activities involved before and after producing a die and mold, including planning, die design, which includes geometry transfer and modification (15%-24% of the time), Tool Path generation (14%-17% of the time), rough machining of the die or EDM electrode is being used (8%-16% of the time), finish machining, which can include pre-finishing when it is required (27%-39% of the time), finishing (13%-23% of the time depending on complexity) and die trial (4%-6 % of the time depending on complexity) [9].

Considering the lengthy and costly trial procedure, having a proper examination method is necessary. Therefore, having a benchmarking procedure in place to examine different die designs, different die materials and suitable surface treatment and process parameters are necessary, which is one of the scopes of this thesis to come up with a cost-effective and robust benchmarking method. Die and workpiece material selection and considering compatibility against one another is an important factor to consider increasing tool life. One of the common considerations in selecting materials is determining the desired mechanical properties. For instance, having a fracture-tolerant component is often an objective that can be achieved by selecting a material with ductility and flaw tolerance, which reduces the possibility of brittle fracture. The compromise is that ductility is often achieved by losing overall strength, wear resistance, and resistance to deformation. To achieve ductility and maintain wear resistance, one may select a surface treating process such as a case-hardening process. In metals, the properties that must be considered to both ensure the desired function and reduce the likelihood of failures include, Tensile strength, Yield strength,

Modulus of elasticity, Ductility (percent elongation), Fatigue strength, Fracture toughness, Hardness, Shear strength, Machinability, Coefficient of friction, Impact strength, Density, Coefficient of thermal expansion, Thermal conductivity, Electrical resistivity [10] etc.

However, this depends on the process too, as in hot forging and die casting, the die suffers from abrasive wear and thermal fatigue, while for cold forging and stamping, the die suffers from high stress and abrasive wear. According to the literature, 70% of tool failure is caused by wear; in this thesis, the focus will, therefore, be on wear and how to predict wear in the design stage. The wear map was constructed in different sliding velocities and contact pressures to aid designers and industries in die wear prediction.

Die life is an important process factor affecting the hot forging industry. This is mainly because of the cost involved in lost productions resulting from die failure, replacement of die blocks, re-sinking of cavities and operative handling of dies. Typically, about 10% of the price of a forged component is attributed to expenses for the dies. It is therefore desirable to increase die life and reduce the cost of the forgings produced. It is known that the lives of forging dies are reduced by wear, mechanical and thermal fatigue, deformation of the substrate, corrosion, and fracture. Wear is responsible for 70% of the tool failure and it was believed in the past that erosion acted as a dominant factor. Oxide layers on the billets were considered a cause of failure in the past while later it was proved that this kind of layer reduces friction and as a result can act as a lubricant. In other words, some of the events accompanying the high-temperature wear like oxidation, debris generation and elemental transfer between two surfaces can act as a wear surface resistant[11]. Hot forging temperatures range from 300-1250°C and this is important for manufacturing complex shape components. Large mechanical and thermal tool loadings result from high contact pressures and high workpiece temperatures during the forging process. Because of thermal loading, tool materials lose their hardness in the surface layer. After the contact release between the workpiece and tools, the tool surface temperature reduces very quickly, which results in re-hardening and creates a white compound layer (When nitrided steel etched with Nital (HNO₃ in alcohol) sublayer turns white)[12].

Because of the radius enlargement, the effects of the hardness increase because of the generation of the white layer, which shows a higher hardness than the base material of the tools. This white layer also called nitride ceramic. Wear investigation can be at different levels, including “Nano, micro, macro” level, and at the higher level it seems more difficult to obtain data for relevant process during wear processes [1]. The micro level is where these problems still occur, while it is different for FEM analysis, where precision of data can be achieved at macro level. The first step of any forging process is to look at forging process design.

1.1.1. Precision forging process design

In precision forging, some parts can be forged in a single set of dies, while others, because of shape complexity and material flow limitations, must be shaped in multiple sets of dies. The most commonly used method of process certification is die trial, in which full-scale dies are manufactured and prototype parts are forged to determine metal flow patterns and the possible occurrence of defects, such as cold shuts, folds, and laps. In the past, different kinds of analysing methods have been employed including the slab method, the slip-line field method, the viscoplasticity method, upper and lower bound techniques, Hill’s general method and, recently, the FEM method [13]. A FEM based software can be used to obtain information about die design and process variables in the forging process. The geometry of finished parts, the type of machinery being used, the quantity or the number of parts to be forged, the application of parts and the overall economy of the process design are important. Hawryluk et.al [14] mentions that the factors related with the forging and operation for the already elaborated industrial forging process are pre-determined and remain constant while author believes that every small change in process parameters, tool setup and different batch of material can change the final output. Die manufacturing is considered as one of the most difficult manufacturing techniques. Even though this technique is being mastered over the years, correct manufacturing of forging parts with complicated shapes which can satisfy the customer high-quality demands requires lots of experience from designing to machining and fabricating [15].

1.1.2. Precision forging process classification

Classification can be based on temperature, forging machines or die set.

1.1.2.1. Classification based on temperature

Precision forging can be classified as hot forging, warm forging or cold forging. In hot forging, the degree of deformation is greater than with the other two methods because of heating the billet to above re-crystallisation, while the formation of scale and low dimensional accuracy and the need for accurate heating systems are the disadvantages of this process. In hot forging, even though deformation can happen in a single operation, the sliding and oxide layers increase the chances of wear after producing a relatively small number of parts. However, this process has a lower wear rate when compared to the warm and cold forging processes.

1.1.2.2. Classification based on forging machines

Precision forging can be classified by forging machines. Two main types, of forging machine are hydraulic press and mechanical press. The other types of press are hammer press, crank press, knuckle joint press, Rack and Pinion press and screw press (which has been used for this work). Selection of a type of press depends on different factors of manufacturing process that the press tool will be employed to perform[5][16].

- Type of process, metal forging, extrusion, impact extrusion, sheet metal
- Press capacity which related to the size of work stoke, type of process
- Length of stroke over which the press deliver force.

1.1.2.3. **Classification based on die set**

Precision open die forging (which is going to be the focus of this thesis) and closed die forging involve a forging process that uses standard flat, V-shape, concave or convex dies in presses and allows grain to flow in one or two directions. The workpiece is compressed on an axial direction or the direction of movement of the upper die, while in close die forging upper die approaches the billet and the billet must fill the cavity where it is being shaped to the desired shape. In other words, depending on the geometry of the dies, a varying amount of lateral constraint can be imposed on the workpiece, a fact that enables forging operations to be classified very broadly into two categories, open die forging and closed die forging.

1.1.2.3.1. **Open die forging**

Open hot forging or upsetting setup includes upper, lower die and billets where billet forced on die to create a shape and on this case to create a notch on the billet. Die set is being placed inside a forging press bolster and heated up to around 230-250°C. Load is different depending on the capability of press and process design. Billets are heated up in a furnace to the forging temperature which is usually in the range of 900-1200°C. Different types of lubricants are being used to reduce the friction between die and billet. A suitable material selection for die and workpiece and proper process design is a key for success in any precision forging. However high stresses on dies caused by high load and fluctuating temperature cannot be avoided which causes die failure. Die failure is categorised as wear, deformation, erosion, thermal and mechanical fatigue but as Wear is responsible for 70% of tool failure and a potential source of high costs; as much as 30% per forging unit in the forging industries[17][18], therefore the focus of this research is on wear prediction. Wear maps can ensure a successful operation when being used as a wear prediction tool supported by FE simulation and physical trials. This thesis also aims to introduce a reliable and repeatable method

of failure measure as well as using the process set up to compare different types of lubricants and coating at an industrial scale.

Open die forging will be the focus of this thesis. Upset forging is sometimes the only suitable forging process when a large amount of stock is needed in a specific location of the workpiece. For many applications, hot upset forging is used as a performing operation to reduce the number of operations or to save metals. In open die forging, metal flow patterns and stress patterns are not highly complex and forgeability is determined primarily by the material structure and process conditions.

Secondly, these are determined by die geometry. Material structure variables include grain structure and texture, crystal structure and the presence of the second phase or solid-solution elements. Material properties include temperatures at which melting, re-crystallisation and phase change of material occur, creep which is a slow time-dependent irreversible process of plastic deformation for a metal material under the influence of stresses which are lower than the yield strength of the material, the variation of flow stress with strain, strain rate, temperature and physical properties such as density, specific heat and thermal conductivity of the workpiece temperature are all very important [19].

In open die forging, the lateral constraint is minimal, and the amount and distribution of lateral metal flow are controlled by factors such as total reduction of the workpiece dimension parallel to the forging direction, frictional boundary conditions, and heat transfer effects. In other words, a complete description of forging, whether an open die or closed die forging, requires specification of various process variables as well as the die geometry and workpiece material. These include speed of forging process, dwelling time, die temperature, workpiece pre-heat temperature, and lubricant. Because of these different variables, one workability test is not enough. Around 30% of press energy is being dissipated to overcome friction [20][8].

1.1.3. Die selection based on material properties

Finding the right material properties for the die is an important part of any precision forming and forging as almost all the forging and forming processes required die (except incremental forming). As mentioned earlier, a large amount of investment goes on manufacturing dies worldwide, therefore die material selection plays an important part. As this thesis is dedicated to hot forging, therefore, die material selection will focus on that. The ASM international book [21] indicates some steps for selecting the material as follows:

- Ability to harden uniformly
- Wear resistance (ability to resist the abrasive action of hot metal during forging)
- Resistance to plastic deformation (ability to withstand pressure and resist deformation under load)
- Toughness
- Resistance to thermal fatigue and heat checking
- Resistance to mechanical fatigue

H series tool steel has a higher resistance towards wear because of the high percentage of chromium, molybdenum, and vanadium. High Chromium content on H series increases the resistance to high temperature and oxidation, molybdenum does not visibly react with oxygen or water at room temperature and bulk oxidation occurs at temperatures above 600°C, resulting in molybdenum trioxide. Trioxide is volatile and sublimates at high temperatures, which prevents the formation of a continuous protective oxide layer and stops the bulk oxidation of metal, which is important in metal formation, molybdenum increases the hardenability. Vanadium can enhance the strength, as well as toughness and plasticity of steel and improves fabrication and service performance [1]. H13 based hot work tool steel is characterized by high resistance to thermal fatigue, thermal checking, good high-temperature strength, excellent toughness, ductility, machinability, air hardenability, resistance to abrasion and high hardness[23].

Tungsten based hot tool work steels have high tungsten contents which provide resistance to softening at high temperatures while maintaining adequate toughness, but it also makes them brittle and to avoid breakage, water cooling of these steels must be avoided. Other types of work steel are low alloy proprietary steel [21]. In hot forging die steels, C, Cr, Mo, and V are principal alloy elements. To guarantee a certain amount of stable carbides and alloy elements are solved in α solution. The VC is very stable carbide when the temperature is around 700 °C and the fact that existence of these types of carbide elevates wear resistivity of steel therefore a great amount of VC is required. Due to the fact that carbides of Cr and Mo are not as stable as VC, Cr and Mo solved in α (α prime) are helpful to improve thermal strength[24]. Alpha prime is a chromium rich phase that is believed to form by spinodal decomposition, although a simple nucleation and growth mechanism at the temperature between 300-550°C cannot be excluded. When formed by spinodal decomposition, alpha prime increases the hardness while reduces impact toughness and increases the embrittlement[25]. Making an alloy is a challenge as metals have different melting point. The general practice is that the initial ingredient will be melted first, and the other metals will be added to the mixture. However, it can be complicated especially when the higher melting point metal is in a smaller proportion. Therefore, different batches of material can have different proportion of chemical composition which makes material selection for forming and forging difficult. As it shows on Figure 1-1 , H series hardness declines as the tool reaches the temperature above 400 °C. For example, H12 has a tungsten which increases the strength of material in hot temperature, but it shows a lower hardness in low temperature compared to the rest of the H series materials. H 13 shows good material properties and good hardness at high temperature.

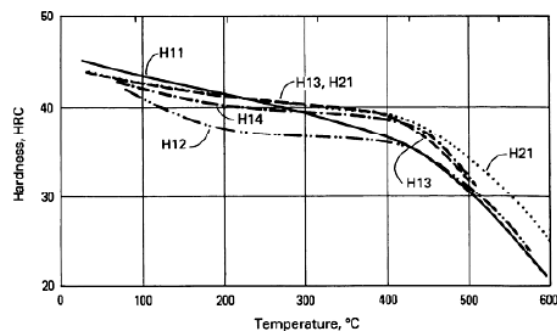


Figure 1-1 Hardnes of H series tool steel at different temperatures [81]

1.1.4. Tool failure

Tool failure can be caused by many factors including overloading, overheating, wear, deformation, thermal cracking, thermal and mechanical fatigue, corrosion, erosion, and fracture. Different material responds differently to the excessive load, the high strain caused by the excessive load can bend or deform the tool material. Overheating could be considered as another factor in die failure as, in hot and warm forging, dies are heated to certain temperatures. However, if such temperatures have not been set properly, this can decrease the resistance of the die towards wear or cause die checking and thermal fatigue. These failure modes are being explained briefly. Predominant failure modes of H13 hot forging tool steel are wear, deformation, thermal cracking mechanical and thermal fatigue and fracture. These failures are caused by multi-impact load, repeated cooling and heating, and elevated temperature friction with processed materials [24]. Proper cooling and eliminating unnecessary processes increases the forging tool life [26]. Wear, which is defined as surface damage or removal of material from one or both of two solid surfaces in a sliding, rolling or impact motion relative to one another, is considered the main cause of tool failure. Wear is responsible for 70% of tool failure and a potential source of high costs; as much as 40% per forging unit in the forging industries which include the tool replacement [1][18][14]. In hot and warm forging operations, surface layers of tools at the tool-workpiece interface are not only exposed to high mechanical stresses but also to severe temperature cycles, which often lead to loss of strength and hardness [27].

1.1.4.1. Tool Wear and Wear Map

Wear, which is defined as surface damage or removal of material from one or both of two solid surfaces in a sliding, rolling or impact motion relative to one another, is considered the main cause of tool failure. Wear is responsible for 70% of tool failure and a potential source of high costs; as much as 40% per forging unit in the forging industries which include the tool replacement [1][18][14]. Wear is categorised as abrasive wear, adhesion wear, delamination wear, fatigue

wear, corrosive wear, and fretting wear. Wear has a close relationship with sliding velocity, contact pressure, hardness, temperature, tool design, and contact time. Many different wear models were presented by different researchers in addition to Archard model which will be explained in chapter 2 of this thesis.

To represent the wear characteristic different wear maps were presented by researcher worldwide. Wear maps can represent the mechanical changes on the worn surfaces of material and the matching part over a range of operating conditions[28]. Knowledge of wear mode and wear mechanisms of the worn surface and counterface is also essential to understand the mechanism of material degradation and chemical effects in the contact[2]. Wear mechanistic maps show the different wear mechanisms for different materials in contact which are based on experimental results[29],[30]. Diagrams which describe the overall behavior of wear are categorised as wear-mechanism map, wear mode map, wear-transition map, and wear-regime map. Wear-mode, wear-transition and wear-regime maps focus on the description of the mode of wear, mild wear, severe wear and the transition between them. Figure 1-2 shows the work of Lim and Ashby et al [3] indicating mild to severe zone for tool steel at different load and speed using an unlubricated pin on disc .

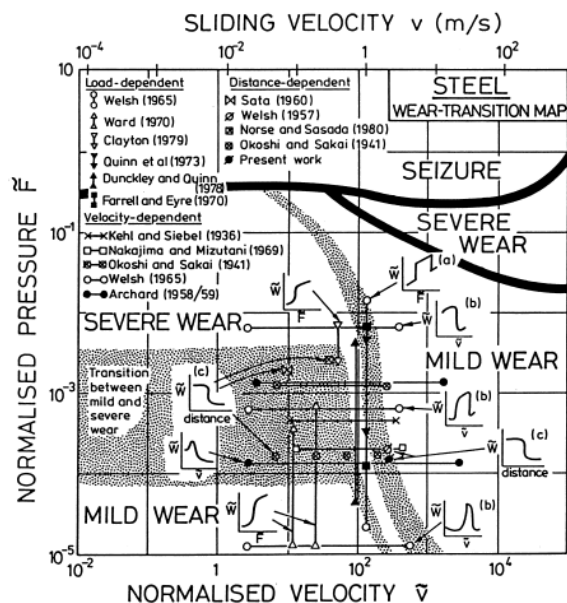


Figure 1-2: Transition wear map

In the case of wear mechanism maps, details of the dominant wear mechanisms are given, and the regions of their dominance are indicated. It can be categorised

as Seizure , melt wear , Oxidation wear and delamination wear like the wear mechanism wear map shown on Figure 1-3 which was produced by Kato et al[31] for steel in unlubricated condition using pin on disc as different load and speed.

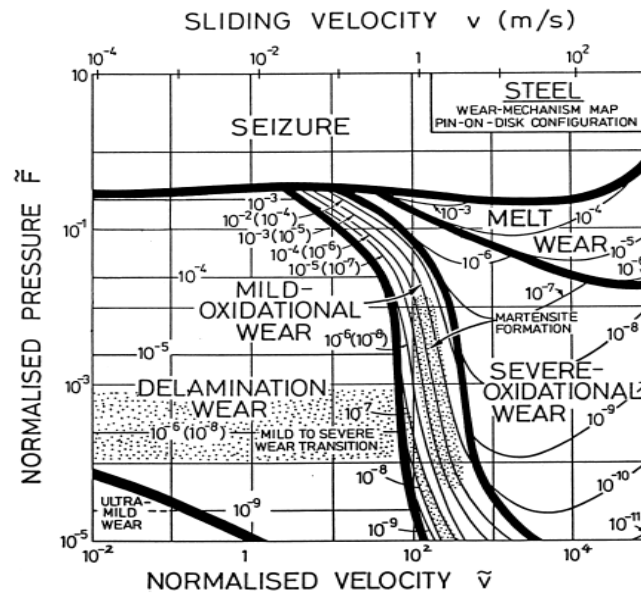


Figure 1-3: Wear Mechanism Map [31]

Researchers have done extended works on this filed which will be reviewed in the next chapter.

1.1.5. Aim and objective

There are many failure modes that contribute to die failure when forging different materials on H13 tool steel at high temperature. Hot forging tool failure modes are categorised as wear, thermal cracking, and deformation, thermal and mechanical fatigue and according to the literature, wear is responsible for 70% of tool failure. The most common faults caused by tool wear are gaps in the filling of the die impression, i.e. incomplete forging, overlaps, flashes, scratches, delamination, cracks etc. This, in turn, affects the functionality of the final product made from the forging[32]. Therefore, the focus of this research is on tool wear by considering that the selection of die material, its hardness and the type of surface tribology (lubrication and tool coating materials being used) are critical for enhancing die life in any precision forging.

The purpose of this work is to identify the dominant failure mode and to model this failure to allow life prediction and to establish a robust method of measurement. The aims are summarised as follow:

1. Generating of series of wear maps using computational model supported by physical trials
2. Establish a cost-effective benchmarking method to test different types of surface treatments

To satisfy these aims the objectives are as follows:

1. Create a computational process for the generation of wear model
2. Characterise the forging process and identify H13 tool steel failure modes when forging Inconel 718
3. Validate the proposed model experimentally
4. Characterise die material
5. Develop a repeatable measurement method
6. Generate Wear Maps for given billet materials and dies
7. Identify the scope and limitations of the computationally generated wear map

1.1.6. Scope

The diagram below shows the research scope,

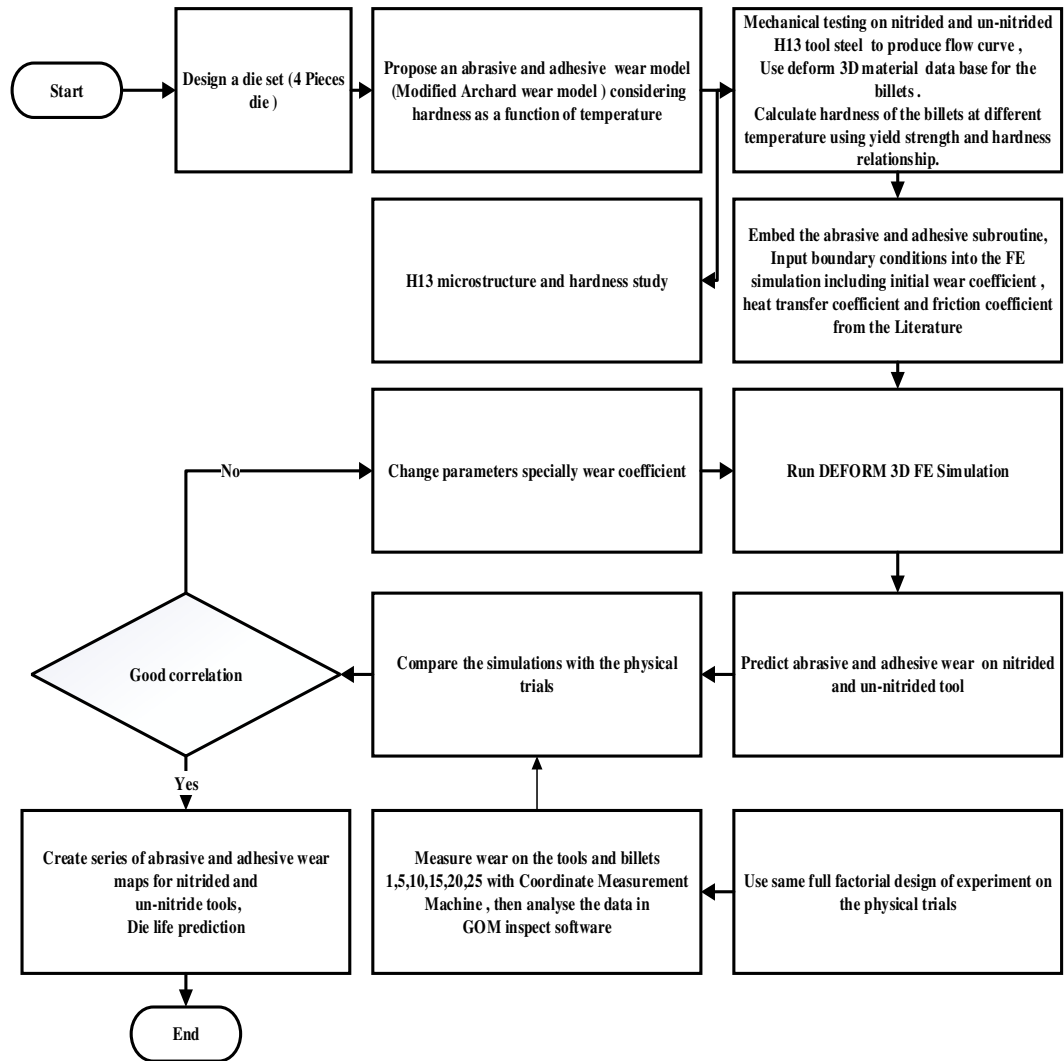


Figure 1-4: Scope of Research

1.2. Research contribution

Author has published a series of journal papers and conference papers which has been explained and referenced throughout the thesis.

1.2.1. Tool failure analysis

Abrasive and adhesion wear was considered as a dominant failure mode when stainless steel 321 was forged on tool steel. However, when Inconel 718 was forged under the same condition H13 tool deformation was considered as a failure mode in addition to abrasive and adhesive wear. These types of failures reflect on the real cases on the industry which cost millions of pounds every year worldwide. This thesis focuses on wear prediction, therefore, tool design was changed to minimise the localised stress and avoid excessive deformation.

1.2.2. Wear model development

A modified Archard wear model was developed and subroutines were embedded in the Deform 3D finite element model for both abrasive and adhesive wear. The wear model considers hardness as a function of temperature. For the adhesion model material removal from the billet instead of the tool was calculated and hardness of the workpiece material at high temperature was calculated. The model was confirmed with a series of practical trials using a die with special design. Then wear was measured, and model parameters were updated accordingly.

1.2.3. Tool failure measurement method

A new failure measurement method was established which allows measuring a tool before and after forging with repeatability of $\pm 5\%$, using a coordinate measuring machine (CMM). This method followed by workpiece measurement mirroring the tool, creating a profile of the change on the billet throughout the forging process to identify the failure. Measuring the changes in workpiece was practical as removing the tool for measurement after every forging

cycle was proven impossible. The limitation of this approach is that the changes on the tool after removing the workpiece will be missed. Therefore, to increase the accuracy tools were measured at the end of each trial to ensure the accuracy of measurements.

1.2.4. Wear map construction

Inputting estimated wear coefficients into the wear model for different temperatures and loads provided estimated wear values for these sets of parameters. Then a series of practical trials were performed to calibrate the model. The new wear coefficients were embedded into the simulations to predict the outcome of the new forging operations. These wear values were used to plot a 3D wear map. This wear map can be used to predict the outcome of the operation under similar process conditions.

1.2.5. Die life prediction

The proposed wear model along with the wear map can be used to predict die life. The possibility to run a cyclic simulation can give a wear result close to the practical trials. The finite element analysis is an effective tool to predict die fill, residual stresses, forming forces, fatigue. In addition, the FEA plays a key role in the construction and optimization of forging tools.

Chapter 2 Literature review

As mentioned earlier tool failure can be caused by many factors including overloading, overheating, wear, deformation, thermal cracking, thermal and mechanical fatigue, corrosion, erosion and fracture. Interaction between the failure modes could be the cause of tool failure and not a specific failure mode[33]. However as mentioned earlier in this thesis the main contributor of tool failure in hot forging is wear which is responsible for 70% of tool degradation.

2.1.Die Wear Mechanism and Models

Each of the various processes by which material can be lost from a surface in service leaves its fingerprint both in the topography of the worn surface and in the size, shape, and number of the particles which make up the wear debris[34]. Wear is temperature dependent and affected by the change of friction caused by sliding velocity and load. The mechanical properties of the material in contact and lubricating properties of many materials start to degrade by an increase of temperature. Contact stress is another important factor and for materials sliding under high contact-stress conditions, where apparent contact stress or pressure approaches the hardness of the softer material frictional heating is assumed to progress evenly over the contact area[35]. It is well known that the type of carbide in addition to the percentage of molybdenum and chromium shows how materials are wear resistant [24]. The maximum temperature, as well as the temperature distribution between the hot forging tool and the work piece, has a major impact on tool life. It is because of the effect of temperature on tool hardness and the fact that the tool surface is heated by conduction from the workpiece as well as the generated heat from friction between the tool and workpiece [36]. In hot and warm forging operations, surface layers of tools at the tool-workpiece interface are not only exposed to high mechanical stresses but also to severe temperature cycles, which often lead to loss of strength and hardness [27]. Wear is categorised as abrasive wear, adhesion wear, delamination wear, fatigue wear, corrosive wear,

and fretting wear. Abrasive wear considered as a dominant failure mode in close die hot forging due to the intensive flow of the material in the presence of abrasive oxide particles[37]. Furthermore, Abrasive and adhesive wear are considered as the dominant failure modes in open die forging which will be explained in more detail. Wear has a close relationship with sliding velocity, contact pressure, hardness, temperature, tool design, and contact time. Wear and friction are somehow interrelated. Coulomb stated that the friction force is independent of sliding velocity other researchers believe that friction is depend on contact area, sliding velocity, surface roughness and temperature [38]. Considerable uncertainty prevails in the description of friction and heat transfer across the tool–workpiece interface, there is always a variation in measured coefficients of heat transfer and this can be considered as a limitation in any research being carried out in hot forging[39].

2.1.1.Abrasive wear

Damage to a component surface arises because of motion relative to the surface of either harder asperities or perhaps hard particles trapped at the interface. Such hard particles may have been introduced between the two softer surfaces as infections from the outside environment, or they may have been formed by oxidation or some other chemical or mechanical process. On the other hand, abrasion can simply take place because the counter face is both rough and harder than a wearing component. The developed models for abrasive wear always consider deformation on the harder surface negligible[40]. The Archard abrasive formula is therefore as follows (equation 2.1):

$$k = \frac{2\tan v}{\pi}, \quad w = \frac{2\tan v}{\pi} \times \frac{F}{H} \quad 2.1$$

Where k, is wear coefficient, w, is wear rate, v is average surface roughness, F is load, H is hardness. Abrasive wear also can happen by removal of material from a surface via plastic deformation. It can cause several deformation modes including plowing, wedge formation, and cutting. The study of abrasive wear been of interest to researchers as one of the main failure modes in machining and forging

industries. K.D. Tozetti et.al [41], Investigated the effect of applied load and abrasive wear sizes on the wear of 2.9% carbon and 19.9% chromium martensitic white cast iron. He used different sizes of abrasive quartz sand and different loads. He realised by increasing load and the size of abrasive the mass loss increases. The Scanning electron microscopy (SEM) result showed that the smaller abrasive grooves appear in the martensitic matrix at lower load while the carbides remained intact. It could be a good experiment to see the effect of sands on wind turbines even though it is a linear progression and abrasive wear is always accompanying with other wear, therefore, it can't be linear. This method is not applicable to forging industries where different materials affected by thermal, sliding wear as well as load, plus wear always accompanied with different types of wear, for example, adhesive wear and never acts linearly. Challen and Oxley [42], studied abrasive wear by considering geometrical functions of contact, interfacial shear strength, stress-strain relationship, deformation mode, and fracture criterion. Their methodology could be applicable for abrasive wear in cutting but not forging as hardness, sliding velocity and contact pressure are important factors in addition to what they considered to be important.

2.1.2. Adhesion wear

Adhesion wear occurs when two solid bodies are sliding against one another and at the asperity contacts at the interface. These contacts may shear due to sliding which results in the detachment of pieces from one surface and attachment to another. This process can be reversed, and the transferred material return to the original surface. The shearing can happen to the original interface or a weakened surface of the contacting bodies. Adhesion wear has a long history, and many tried to come up with an explanation of this phenomenon including Archard. He considered, for the sake of simplicity, the shape to have a hemisphere of the radius and a sliding distance L ($2a$), generating a wear volume of $\left(\frac{2}{3}\right)\pi a^3$. To calculate the wear volume per unit, the wear volume of $\left(\frac{2}{3}\right)\pi a^3$ is divided by $2a$, giving a value of $\left(\frac{1}{3}\right)\pi a^2$.

The wear formula can, therefore, be written as follows (equation 2.2):

$$w = \frac{\pi}{3} \times \Sigma a^2 = \frac{1}{3\pi} \times \Sigma \left(\frac{\pi w l}{H} \right) = \frac{F}{3H} \quad 2.2$$

Where w , is wear rate F , is load, H , is hardness. Plastic deformation of a lubricant scale under the high-stress area can increase the contact area and adhesion to the die. Thick scales stick poorly to billets, pieces of scale can remain coated on the die and increase the wear[8]. Adhesive wear occurs when there is low-velocity sliding friction under high unit pressures in areas of actual contact [37].

2.1.3.Parameters influencing wear

The primary parameters influential to tool wear are toughness and surface hardness at high temperature which reduces during the repeated hot forging process, workpiece deformation and contact pressures, sliding velocity, contact time, sliding length, friction, workpiece and tool temperature, lubrication and methods of tool surface cooling, die design etc. An increase in forging energy and friction between the tool and the workpiece increases tool surface temperature which can increase the chance of adhesion wear as well as thermal cracking. However, identifying the real cause of tool failure is difficult due to the complexity of the interaction between the failure modes. The factors influencing the wear are explained by Artinger and reported by K.Lange on a diagram shown in Figure 2-1[43].

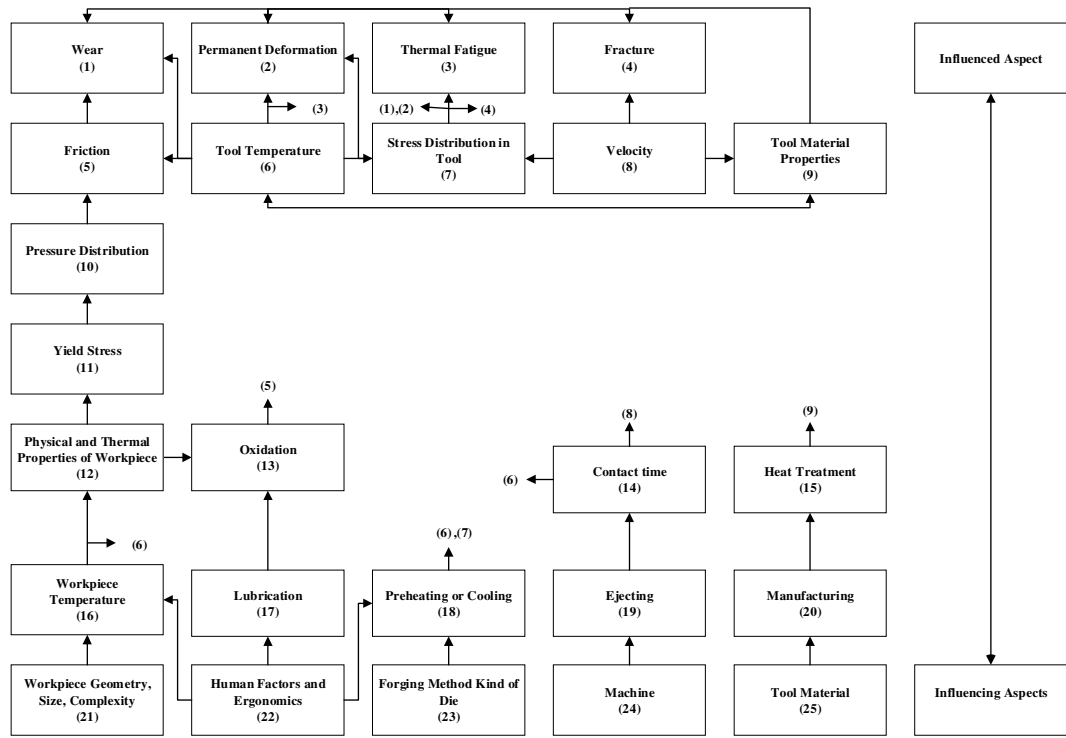


Figure 2-1: Factors influencing wear and deformation failures [43]

It starts with influencing aspects which are workpiece geometry, human factors and ergonomics, forging method on different dies, machining, and tool material what additional surface treatment and operational parameters influences die life. The contact time, sliding velocity, friction, interface pressure and temperature are considered as interactive factor which proves Archard methodology. K. Lange also considers oxidation as a positive and negative influence at the same time, as it can act as a lubricant. However, K. Lange failed to include tool geometry especially the sharp corners in his diagram as an important factor influencing die life while author believes highest mechanical and thermal loading appears on the tool's sharp corners [1]. Sliding velocity, pressure, temperature, hardness are the parameters which interact clearly during the forging and forming process while some other parameters including friction are interacting with the rest of parameters in a different way. Interface friction mechanic is very complex. There are different ways of expressing friction whether through friction coefficient, μ , or friction shear factor, m . σ_n is normal contact pressure, $\bar{\sigma}$ is flow stress Therefore, shear stress τ , is (equation 2.3)[44].

$$\tau = \mu\sigma_n \quad \text{or} \quad \tau = \frac{m}{\sqrt{3}}\bar{\sigma}$$

2.3

Die design is another important factor which interacts with all the parameters including friction. The maximum predicted die wear occurs on the corner of the die with a small radius such as flash geometry, fillet radii, draft angles, and die face contact area where there is not much of friction but high-stress concentration. The other factor is the variation in the lubricant which can be controlled by using lubricant with consistent friction coefficient. The lubricant should be characterised by a high flash point so doesn't lose its tribological properties at high temperature. The lubricant has to have low heat conduction and proper viscosity at the forging temperature[7]. Because the cooling effect and low friction are essential to the long life of dies, the proper selection of lubricant and surface treatment is crucial in the hot forging process[32]. The main function of lubricants is to reduce friction between the die and the workpiece, heat losses from the workpiece during the forging process and die wear[32]. Workpiece complex geometry can have an influence in increasing tool wear as it can increase the stress on different parts of the die especially on sharp corners. Appropriate cooling time after each blow is important as increasing the dwelling time can increase the chance of die failure. The communication between supplier, process design and manufacturing team plays an important role in a successful forming and forging process and producing high quality product.

2.1.4.Tool plastic deformation

In forging the most of the energy for the first blow being used to deform the billet. The elastic deformation of the tool, the friction energy and vibration of the anvil is limited. The second blow is more elastic and plastic deformation is low. The accumulated elastic energy by the tool return as reflection energy, which shows that the first blow is, therefore, more efficient than second[45]. Plastic deformation occurs at regions which are subjected to extreme pressure and temperature in long period of time. The increase of interface pressure to the above

yield strength of the die material during forging causes deformation in die material which usually happens in sharp corners[46]. Both plastic deformation and friction contribute to heat generation. This temperature generation influences the lubricant condition, the metal flow during the deformation and die service life and productivity of the metal forming process [47]. In the forging process most of the mechanical energy is dissipated as heat, this changes the temperature on the part and die. This process increases the possibility of thermal softening and deformation of the die [48]. Plastic deformation is one of the causes of failure of hot forging tools, where the tool deforms to such an extent that parts formed are no longer within dimensional tolerance [4].

After forging 200 Inconel 718 billets on a tool made of H13 tool steel, deformation was evidence which was investigated further using elastoplastic FE model and microhardness, scanning electron microscopy (SEM) and electron backscatter diffraction (EBSD) analysis which will be explained in detail in chapter 5. Anderson et al investigated the cause of deformation on nitrided H13 tool steel which was used for forging an aerofoil component. He found deformation on the substrate below the nitride layer. The tool was nitrided to 0.25 mm case depth[49]. The author believes that 0.25mm case depth has influenced the deformation of sublayer as ASM standard states that excessive nitriding of more than 0.13 mm case depths cause spalling and it increases the chance of deformation on sub layer[50].

2.1.5. Different wear models in addition to Archard model

Many different models were presented by different researchers in addition to Archard model. Considering the factors which are influencing tool wear as presented in Figure 2-1, the author believes that it is impossible to come up which a universal model to predict wear in all the conditions however some models work better than others in multiple conditions. To mention the few:

- 1) J.H Kang et al [51] came up with a new wear model considering the change of hardness during the tempering as shows equation 2.4

$$d_{fin} = \sum_1^n \frac{KPL}{3H} \frac{H}{H(T, t, w_{initial})} \quad 2.4$$

Where d, is the final wear amount K, is the dimensionless wear coefficient, P is the pressure and L is the sliding length. H is the change of Rockwell hardness during tempering which is the function of temperature, cycle, and initial wear. This model can predict wear considering the effect of tempering of the tool but fails to consider the change in hardness due to change in temperature of the die during the forging process.

2)I.Sallit et al[52] proposed a test methodology that enables observation and quantification of the effects of the temperature and the sliding distance on the wear rate of 40CrMoV3 steel against C35E steel, in ambient conditions, and at temperatures between 700 and 850 °C. The wear model proposed to calculate the wear shown in equation 2.5

$$w = \frac{1}{F} \left(\frac{R_R}{R_R \cdot N_R + R_T \cdot N} \right) * \left[R_R - \sqrt{R_R + \frac{\Delta w R}{\pi l \rho}} \right] \frac{1}{\Delta t} \quad 2.5$$

Where w is the wear rate (m²/N); l: width of the roller (m); R_R: radius of the roller (m); N_R: rotation speed of the roller (t s⁻¹); R_T: radius of the track (m); F: applied load on the roller (N); ΔwR: weight change of roller (kg); ρ: density of steel (kgm⁻³); Δt: duration of test (s); R_R ¼ 35.00 x10³ m; l = 5.00 x10⁻³ m; ρ=7.80 x 10³ kg m⁻³.The equation was a breakthrough in considering the friction and sliding distance however his approach was valid only in an ambient condition which is not the usual case in hot forging and he failed to consider the effect of hardness.

3) M. R. Soleymani Yazdi et al [53]used a model shown on equation 2.6 plus the finite volume method for modeling the hot Forging process.

$$Z_i = \frac{1}{3} \sum_{j=1}^n \frac{K_{ij}(T) (\{\sigma_n(t)\}_{tj} \cdot \{u(t)\}_{ij})}{H_{ij}(T)} \Delta t_j \quad 2.6$$

Where Z is the wear depth, u the sliding velocity of the contact surface and σ_n , the normal contact pressure on the contact surface, H , hardness function of temperature and K , dimensionless wear coefficient and t , is time. Even though he proposed a very good model considering sliding velocity and hardness as a function of temperature which agrees with his practical trial, it is not clear the type of wear which he is focusing on. Furthermore, materials respond differently to load and temperature which hasn't been identified in this model.

4) Tulsyan, et al. and Painter, et al [54]. Used Deform finite element model to predict die wear considering coefficients which can be measured experimentally using equation 2.7

$$W = K * \left(\frac{P a V b t}{H c} \right) \quad 2.7$$

However, they failed to consider hardness as a function of temperature. Where W is the wear depth, K , dimensionless wear coefficient, P , contact pressure, V , sliding velocity, t time step, H , hardness of the tool, and a, b, c are experimental constants.

5) D.H. Kim et al [55], proposed a model which was embedded in FE simulation to predict abrasive wear and deformation using equation 2.8.

$$W = \frac{K}{3h(M - weardepth)} \sum_{i=1}^N (\sigma_n V_s \Delta t) \text{Err} \quad 2.8$$

Where W is a wear depth, K is the dimensionless wear coefficient, h is the hardness change of a die towards the direction of wear depth, σ_n is normal pressure, V_s is sliding velocity and Δt is time step.

However, he failed to consider hardness as a function of temperature

2.1.6.. Wear map generation

Wear maps can represent the mechanical changes on the worn surfaces of material and the matching part over a range of operating conditions[28]. Knowledge of wear mode and wear mechanisms of the worn surface and counterface is also essential to understand the mechanism of material degradation and chemical effects in the contact[2]. Wear mechanistic maps show the different wear mechanisms for different materials in contact which are based on experimental results[29],[30]. Wear in conditions of sliding contact can vary over many orders of magnitude. There isn't any universal mechanism of wear and no simple correlation between rates of wear or surface degradation[56]. Identifying the operating point of a sliding contact in an appropriate wear map can assist in establishing the possible or likely modes of surface damage and how close the operating conditions are to any transition between mild and severe regimes of wear. Creating a wear map has always been one of the focuses of researchers worldwide. It started as early as 1941 by Okoshi and Sakai[3], [57] presented a wear map which was produced using the pin on disc method considering wear rate function of speed and pressure. In the early 1980s, a series of diagrams, mostly for the unlubricated wear of steels with different test configurations, was proposed. These include the works of Childs [58], Eyre [59], Marciniak and Otimianowsk and Egawa [3]. Marciniak and Otimianowski [3] wear diagram was similar to the work of Okoshi and Sakai [3], [57] while Childs [58], Eyre [59] and Egawa [3] wear maps showed the boundaries between mild and severe wear behavior within the range of sliding conditions. Welsh [60] presented a wear map summarising the sliding conditions corresponding to mild-wear, severe-wear, and transitions zones. Lewis [61] followed the Welsh approach collected wear data from small-scale and full-scale

Laboratory tests as well as measurements were taken in the field. The data was then presented a series of transition wear maps highlighting a few rail steel wear regimes. The result showed a breakthrough in the field of wear map construction as lab-based data were compared with the field data. However, the lack of data for wear map construction and an error of using lab-based equipment was a limitation

of this method. S Wilson[62] conducted a dry sliding wear experiment at specific temperatures were conducted on a PVD (reactive ion plated) TiN coating deposited onto an austenitic stainless-steel substrate. The coating was worn using a pin on disc sliding at dry condition. His configuration was a low contact load with various sliding velocity. Three wear regimes were identified: at low, temperatures and sliding speeds, mid-range temperature, and higher temperature. The wear map produced to present the data to show the change of temperature at a different speed but as it was done by using lab-based equipment and in dry condition hardly could represent the real-life phenomena. H. So et al[63]. Employed a pin-on-disc configuration for studying the formation and wear mechanism of tribo-oxides on sliding contact surfaces of some steels at the dry condition and under ambient temperature. The sliding speed that he selected was between the range of 0.6 to 8m/s and the pressure of pin on the disc was between the ranges of 0.55 to 8.86MPa. Three wear mechanisms were found from the micrographic results. When the pair were subjected to the small nominal pressure and sliding speed, the wear loss was mainly due to adhesive and abrasive mechanisms. When the nominal pressure was increased to over 4.4MPa and the sliding speed was greater than 3m/s, the wear loss was mainly due to plastic extrusion of material from the pin and the wear became severe. In between these two extremes, the wear mechanism fell in the regime of oxidational wear.

Seung Ho Yang[64] used a silver film to lubricate the bearing steel made of AISI 52100 steel unlike others mentioned above who didn't use lubricant. He used a ball on a disc, lab-based equipment under different pressures and ambient temperature. As a result, three main regimes were clearly identified: (i) elastic/plastic deformation of the silver coating without failure, (ii) mild wear regime after the initial failure of silver coating and (iii) severe wear regime. In the mild wear regime, the contact surfaces were covered with transfer layers of agglomerated wear particles. He discovered that at high speed hardly any film transferred from one surface to another and wise-versa and when the film was transferred acted as a protective layer. This was a good attempt towards the better wear analysis and wear map construction using lab-based equipment. Some other researchers like Ingram et al. [15] and P.Marklund and R. Larsson [65] studied the

effect of contact pressure and sliding distance using a pin on disc method were only able to have an investigation in a relatively narrow (localized) area[15].

2.2. Tooling material and Coating

There are many factors that can help to solve the tool steel failure including the correct process plan and setup, correct use of the press, even lubrication and applying different types of surface treatment. Tool steel surface can be protected by different types of surface treatments, including heat treatment, nitriding, surface coating, and additive layering and overlay welding[15]

2.2.1. Heat treatment

Heat treatment is a process that helps to change the microstructure to the desired results specification. It includes heating the material at high temperature followed by slow or sudden cooling. Heat treatment techniques include annealing, case hardening, precipitation strengthening, tempering, normalizing and quenching. Fe-C diagrams in Figure 2-2 shows two diagrams, the stable Fe-graphite diagram (dashed line) and the metastable Fe-Fe₃C diagram, can be used as the basis for the understanding of the heat treatment of steel. The stable condition usually takes a long time to develop especially in low temperature and low carbon range. Therefore the metastable diagram is of more interest [66]. A₁ is the eutectoid temperature which is the minimum temperature for austenite, A₃ is the lower temperature boundary of the austenite region at low carbon content which is $\gamma/\gamma + \alpha$, while A_{cm}, is the counterpart boundary for high carbon content. The carbon content at which the minimum austenite is attained is called eutectoid carbon content which has 0.77wt %. The ferrite-cementite mixture of this composition formed during cooling has a characteristic appearance and is called pearlite and can be treated as a microstructural creature or microconstituent. Ferrite (BCC) is relatively soft and low-temperature phase, while Austenite (FCC) relatively soft medium –temperature phase, however, both are developed at stable equilibrium phase. Cementite is complex orthorhombic and against the other two develops at metastable phase.

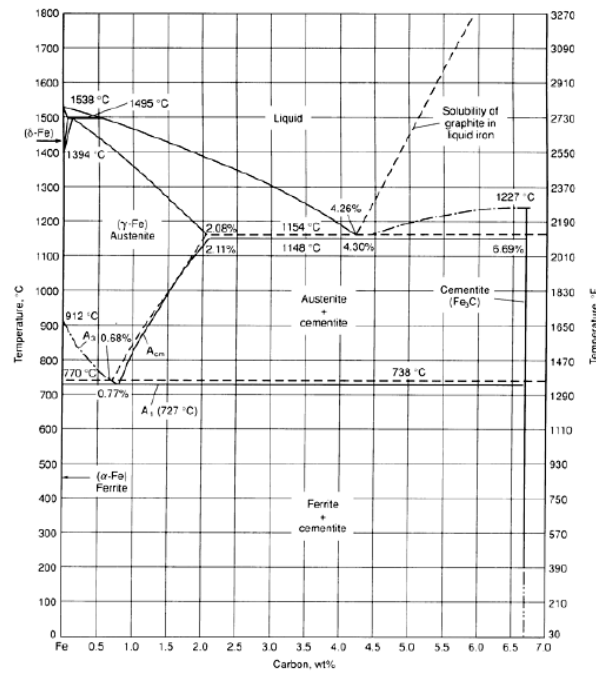


Figure 2-2: Fe-C Diagram for steel[66]

Some difficult to form materials such as hot work die steels like H13 which is being used for this work, can be accurately formed and hardened by austenising, martempering and hot forming to shape immediately after there are extracted from the quench bath, if martempering (which is to delay the cooling just above the martensitic transformation for a length of time to equalize the temperature throughout the piece) temperature is above the martensite transformation temperature for the specific alloy being treated. Because the objective of martempering is to develop a martensitic structure with low thermal and transformation stresses, there is no need to hold the steel in the martempering bath for extended periods. The H13 Heat treatment procedure shown on the diagram (Figure 2-3).

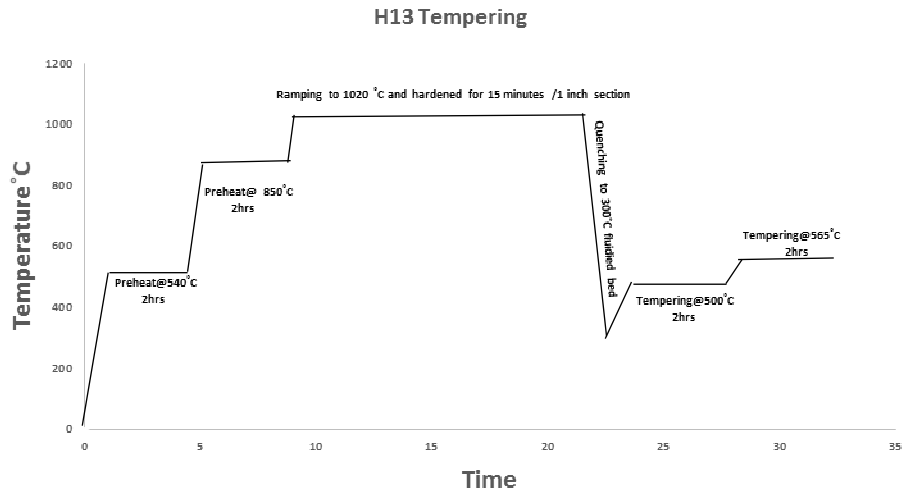


Figure 2-3: H13 heat treatment procedure

2.2.2. Nitriding

Nitriding is a heat process of diffusing nitrogen on the surface of the tool to create the case-hardened surface. During the nitriding process, in the nitride zone, the dynamic pressure appears, which is related to Darken drift velocity (generated by the interdiffusion) and depends on metal viscosity[67]. Nitriding protects the die from wear, deformation, thermal cracking, thermal and mechanical fatigue. Nitriding increases surface hardness and induces compressive residual stresses. Nitriding can be categorised as gas nitriding, salt nitriding, laser nitriding, Ion and plasma nitriding.

The solubility bounds of nitrogen in iron is temperature dependent, and at 450°C the iron base alloy will absorb up to 6 % of nitrogen. However, after this, the surface phase formation on steels inclines to be only epsilon (ϵ) phase. This strongly depends on carbon content. The larger the carbon content, the more potential for the ϵ phase to form. As the temperature is increased to the gamma prime (γ') phase at 490°C, the bounds of solubility begin to decrease at the temperature of 680 °C. The equilibrium Iron- Nitrogen diagram (Figure 2-4) shows that control of the nitrogen diffusion is critical to process success[68].

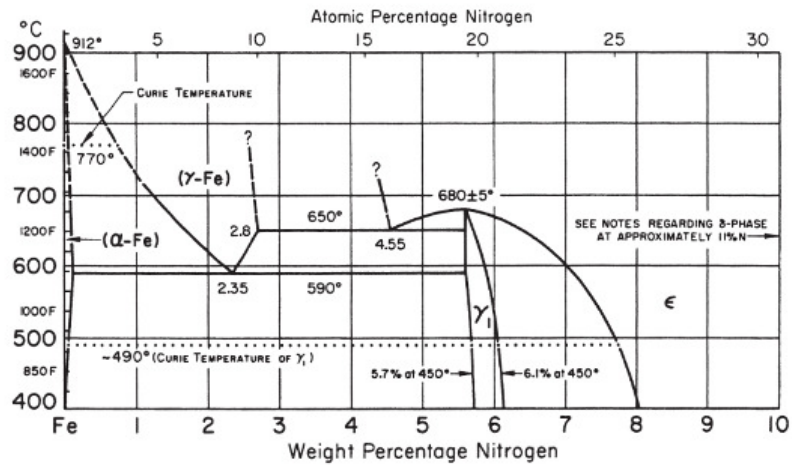


Figure 2-4: Iron -Nitrogen diagram[68]

- Effect of nitriding on yield strength and material flow

Despite small depths of the diffusion layer on the part, nitriding influences yield strength of the material and reduces plasticity and viscosity. The hydrogen during furnace nitriding might have an influence on mechanical properties[69]. V.F. Terent'ev et al reported the change in the mechanical property of material after nitriding. Comparing the material flow after nitriding shows an increase of strength properties of carbon steel 40 by 142 MPa. However, the alloy steel 40X showed decreased strength by 158 MPa. The result showed that for steel 40 elongation decreased from 27.3 up to 20.6 % as well as area reduction of 55 up to 37%. While grade 40X steel showed a different reduction of elongation of 20 up to 1.3% and area reduction of 52 up to 1.3% (Figure 2-5)[70].

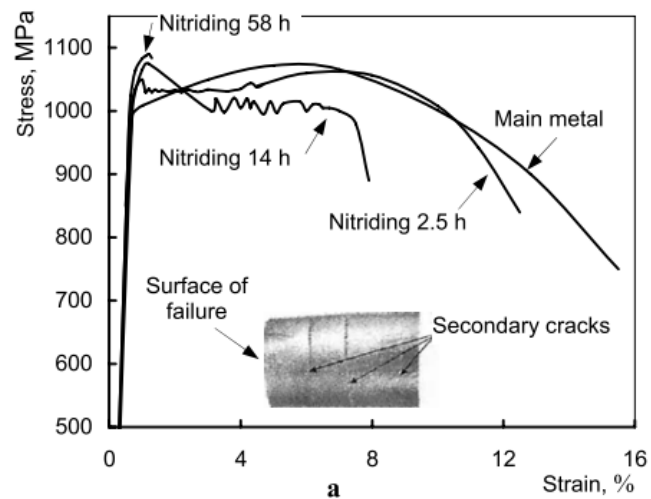


Figure 2-5: Stress-strain curves of nitrided steels AISI 4140[70]

Therefore, the author decided to nitride H13 steel tensile samples, perform tensile tests on these samples and use the material data to run a simulation for the nitrided tool.

2.2.3. Gas nitriding

In gas nitriding, the donor is a nitrogen rich gas, which is usually ammonia (NH_3). The contact between the ammonia source and heated workpiece results in the separation of nitrogen and hydrogen. The nitrogen then diffused on to the surface of the metal and creates a nitride layer. Deepak Kundalkar et al investigated the effect of gas nitriding on thermal fatigue behavior of martensitic steel. He believed that the diffusivity of nitrogen varies with temperature, concentration and diffusion time, depicts the various zones formed during the process of nitrogen diffusion. The results showed the lower is the ratio of the compound layer to the total diffusion depth, the higher is the fatigue life [71]. The downside of gas nitriding are as follow,

- Costly cleaning or grinding to remove the brittle white layer associated with traditional nitriding.
- Gas nitriding case depth is not uniform
- Using ammonia (NH_3) and phosphate for activation will roughen a ground and polished surface.

- Gas nitriding operates at 524 -579 °C and can change the core properties of the material.

2.2.4. Plasma nitriding

Plasma nitriding conveys the high surface hardness and it creates a surface with high resistance to wear, scuffing, galling and seizure. This eliminates costly cleaning or grinding to remove the brittle white layer associated with traditional nitriding. A uniform glow discharge covers all the surface and therefore creates consistent surface hardness and case depth. This is especially noticeable on complex geometries where gas nitriding case depths can be non-uniform. In plasma nitriding (H_2+N_2) is being used instead of ammonia and phosphate. The ammonia roughens the surface. Plasma nitriding has a higher surface hardness and maintains the material's core properties due to the lower processing temperatures around associated with plasma nitriding (482- 510°C). Many different ranges of material can be used for plasma nitriding, including cast iron, mild steel, mold, tool steel, high-speed steel, and stainless steels. In addition, plasma nitriding is environmentally friendly as uses non-toxic precisely controlled gas mixtures.

2.2.5. Ion nitriding and Nitrogen Ion implantation

Ion nitriding is a thermally driven process that produces a relatively deep case depth (100-400 μm) and hardened case layer. While nitrogen ion implantation is a non- thermal (room temperature) and none-equilibrium process unlike Ion nitriding and can produce a thin case depth (1 μm) very hard nitrated layer. The strength of ion nitriding layer is due primarily to formation of transition metal nitride precipitates, while the strength on nitrogen ion implant is due to dislocation pinning[72].

In this thesis plasma nitriding being used after considering all the pros and cons of different types of nitriding. Plasma nitriding is attractive because of its relative high efficiency even at low temperatures. This is a great property for material, such as stainless steels or tool steels, for which this condition is compulsory in order to minimize microstructural variations and, therefore,

maintain the corrosion resistance in the bulk material[73]. Moreover, review of relevant literature shows that precise control of the surface characteristics and composition during plasma nitriding is a challenge, owing to the complexity of this non-equilibrium process. But Pros of this process compared to cons still makes this process better than the rest of the nitriding process. Furthermore, studies reported by Mittemeijer and co-workers have shown the importance of the so-called “excess” nitrogen on the diffusion process [74]. Such increased nitrogen concentrations signify the atomic fraction exceeding the quantity that should be expected in a case that: (i) the alloying elements are fully spent to form nitrides and (ii) the nitrogen equilibrium solubility in an unstrained iron matrix is achieved. Even though the nitriding of AISI H13 hot work tool steel has also been intensively studied but the thickness of layer hasn't been identified. In this work ASM standard < 0.13 mm has been followed [75].

2.2.6. Surface coating

The surface coating is a process of using different materials to cover the substrate to protect the substrate from corrosion, wear, fracture etc. Selecting a correct coating material as well as an appropriate method of applying the coating layer is crucial. The process parameters in which coating layers being applied influence the result. It is therefore important to understand the interaction between the substrate and the additional layer. The additional layer must be effective and not costly at the same time otherwise it increases the cost involved. The additional layer must be suitable for the purpose and cost-effective at the same time. Figure 2-6 shows the relative cost of the different type of surface treatments[76]. This is very important to have a good business case and understanding of the effect of different surface treatments to find a cost-effective solution. The cost evaluation [76] in Figure 2-6 shows the nitriding is considered as one of the cheapest types of surface treatments. That is one of the main reasons that nitriding along with the change of tool design has been proposed as a solution for H13 tool failure in this work.

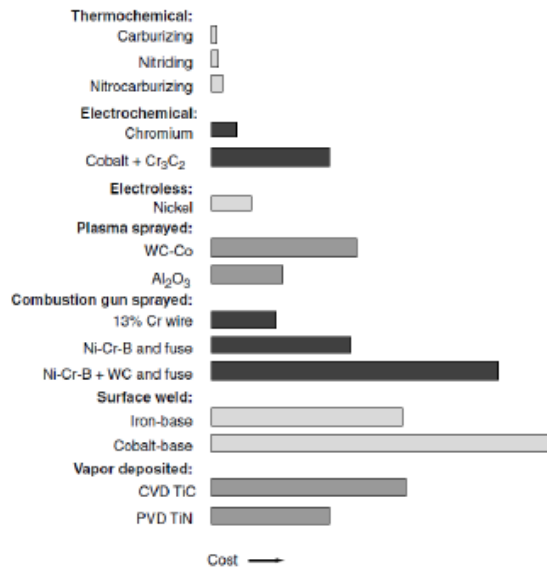


Figure 2-6: Approximate relative cost of surface treatment[76].

Hot forging die surface and the subsurface region are subjected to the severe conditions during forging and by increasing surface hardness the resistance towards these conditions increases. The techniques such as:

1. Physical vapour deposition (PVD), Chemical vapour deposition (CVD)

These methods more commonly used for cold forging but some good results have been reported using these techniques in hot forging[76]. The materials deposited by these techniques are:

- Hard coatings wear resistant coating
Like carbides (TiC), nitrides TiN, CrN, (TiAl) N
, oxides (Al₂O₃) and diamond etc.
- Soft and self-lubricating coatings
Like MoS₂, DLC (diamond-like carbon coating) etc.

2. Thermal spray method

The other method of coating is thermal spraying which is basically spraying a molten or soften material on to a surface like tungsten, tantalum, ceramic etc. The glass coating on the billets which was used on one of the experiments was applied using this method.

All the mentioned coating techniques have their own advantages and disadvantages.

2.2.7. Additive layering

Additive manufacturing is an opposite condition of normal manufacturing when the material being added structures are made by the addition of thousands of extremely small layers which combine to create the product. This method recently being used to repair or protect the material by adding an additional layer of material. There are different methods of metal deposition. The Powder Bed Fusion process includes the following commonly used printing techniques: Direct metal laser sintering (DMLS), Electron beam melting (EBM), Selective heat sintering (SHS), Selective laser melting (SLM) and Selective laser sintering (SLS). One of the methods which have shown a promising result for tool protection is Laser Metal Deposition with powder (LMD-p) which can provide a hard-facing alloy repair to hot forging tools. This is particularly important on complex tool geometries due to their superior wear resistance. The ALM process known as Laser Metal Deposition with powder (LMD-p) can be used to provide a hard-facing alloy repair to hot forging tools. This is particularly important on complex tool geometries due their superior wear resistance. The metal additive deposition allows the bonding of different materials with different chemical composition. This enhances the resistance towards wear, fatigue and other tool failure modes. This method was used in The Advanced Forming Research Centre (AFRC) to establish a low-cost standard test method to evaluate abrasive and adhesive wear on hot forging H13 tool steel dies on an industrial scale 160 kJ Schuler screw press. The author's methodology was used for execution and analysis which shows the practicality of this methodology [77].

2.3. Discussion

The proposed mathematical wear model for predicting die wear by different researchers has shown the extent of research in this field, what are the limitations and that there isn't any universal wear model which can be used to predict the failure for different material under different conditions. Their research results in identifying the parameters influencing the wear are mainly sliding velocity, contact pressure, wear coefficient, hardness, contact time, friction, stress and strain and some other material dependent constants that are calibrated based on the material characteristic. The interaction between different wear influences the results and how to present that is a challenge. Therefore, even though they all have contributed in this field and some they have been used for specific cases they have failed to consider all the main contributors in one wear model and there is hardly any evidence that the real failure data has been fed back to the model to optimise these wear model. Furthermore all the researchers and the experts in wear map construction used lab-based equipment and a similar methodology as summarised below[78],

1. Selecting materials of interest, the mode of contact, contact geometry, the environment in which they contact, and lubricate or unlubricated test condition must be identified.
2. Finding similar or closed to the experimental conditions data from the literature on wear rates and wear mechanisms to use.
3. Identifying the parameters to be used as axes on the wear map. It depends on the dimension of the map whether it is 2D or 3D. It also depends on which type of map is being constructed. Whether it is mechanism map or a surface interaction map (severe, mild and transitions zones) or dominant mode map. Or just give an idea of how a material interacts at a certain speed and load and what is a material interaction with other parameters.
4. Constructing empirical wear maps. It is done by grouping the wear data according to the wear-rate and wear mechanism of data. It is plotted on the two-dimensional map then the boundaries of dominant failure modes are

constructed. In this stage of the produced map is informative and gives a global idea.

5. Now that all data is available finding the correct model which can explain wear on this sliding system will be important. The model then will be calibrated to be used for fields with no experimental data.

due to the uncertainty in Lab based equipment like the pin on disc, a significant error is produced which could hardly be a representative of the real-life forging and it fails to satisfy industrial manufacturing standards. This literature study showed that creating a single process that uses a wear model embedded in Finite element simulation (considering parameters influencing tool wear degradation), practical trials using industrial scale equipment, robust and repeatable failure measurement method to create an industrial wear map (instead of lab-based wear maps) as an output hasn't been developed and could be a breakthrough. This will help the industries to find the effect of the parameters in real life. The methodology that the author used to construct the wear map will be explained further in this thesis.

Chapter 3 Research Methodology

Diagram Figure 3-1 illustrates the research methodology which was adopted for this research. Different tools have been used for this research to create a series of wear model by going through different steps including DMAIC six sigma method, maturation of wear mathematical model and FE simulation, creating a repeatable measurement method. This also could be used for benchmarking.

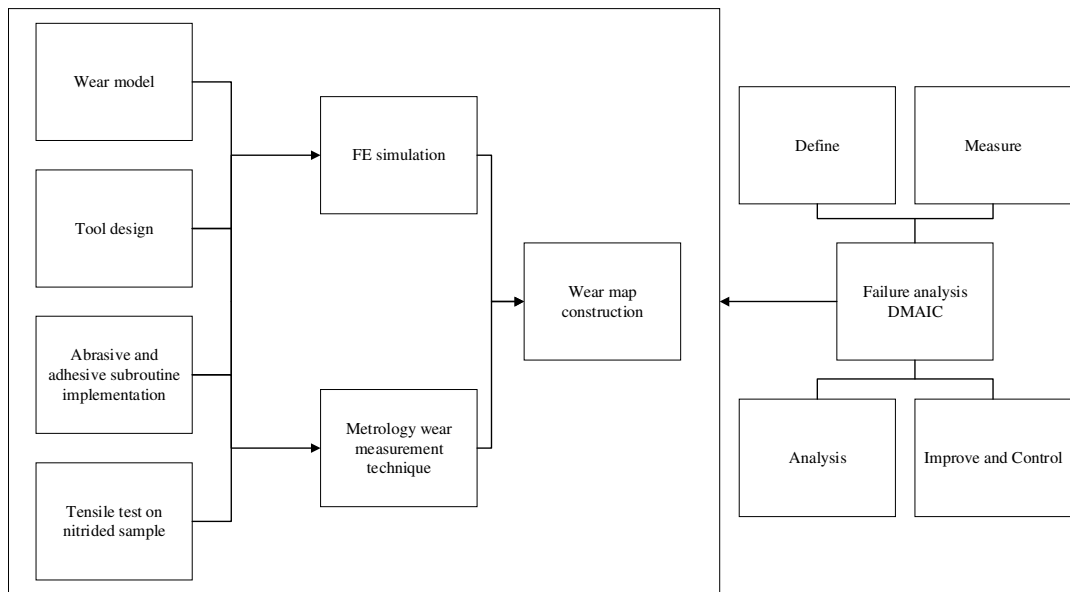


Figure 3-1: Diagram illustrating the research methodology

For failure analysis Define, Measure, Analyse, Improve and Control (DMAIC) process of six-sigma was used which is being used for improving, optimizing and stabilizing. This can be explained as follows:

- Define: Knowing the problem and identifying the goal and outline the target.
- Measure: Decide what parameters need to be quantified, find the best way to measure, collect important data and carry out the measurements by experiment.
- Analyse: Spot gaps between actual and goal performance, establish causes of those gaps, find out how process inputs affect outputs and class development opportunities.

- Improve: Develop prospective solutions, categorize solutions that are easiest to implement, test hypothetical solutions, and implement actual improvements.
- Control: Create a detailed solution monitoring plan, update plan records on a customary basis, and suggest a method of training.

Ishikawa fishbone analysis method was used in the analysis phase of DMAIC to brainstorm for cause and effect of tool failure. The diagram listed different factors which can lead to tool and process failure, including machinery and equipment, people (operators, designers, and all the other personals), design, method, material and surface treatment. A modified Archard wear prediction model was used to predict tool wear which consists of sliding velocity, contact pressure, hardness, wear coefficient and other experimental coefficients. It considers hardness as a function of temperature. A repeatable method of tool failure measurements using CMM was established measuring the change in die and workpiece. Cyclic simulation of forging Stainless steel 321 and Inconel 718 at high temperature followed by practical trial allows understanding wear progression after multiple forging cycles process.

3.1. Experimental Equipment and wear model implementation

Table 3-1 shows the list of experiments conducted to generate a series of wear maps,

Table 3-1: List of experiments for wear map generation

Scoping Study	Simulation	Forging trial	Metrology	Micro Hardness	Tensile test	Microstructure analysis
Inconel 718 billets, H13 Tool steel	Nine rigid plastic simulation as per as DOE (25 cycles)	Nine Forging trials forging 25 Inconel 718 billets on H13 tool steel as per as DOE	CMM measurement of all the Tools and billets 1,5,10,15,20, 25		H13 Samples	
Inconel 718 billets, Nitrided H13 Tool steel	Nine rigid plastic simulation as per as DOE (25 cycles)	Nine Forging trials forging 25 Inconel 718 billets on H13 tool steel as per as DOE	CMM measurement of all the Tools and billets 1,5,10,15,20, 25	On nitrided Tensile samples	Nitrided H13 Samples	On nitrided Tensile samples
Deformation Study	Elasto Plastic simulation			On H13 Tool		Analysis using SEM and EBSD

3.1.1. Wear model

A modified version of the equation 3.1 proposed by Tulsyan, et al. and Painter, et al was used [18]. Hardness was considered as a function of temperature which is the real case in the forging condition. The model uses sliding velocity and the contact pressure between the workpiece and die. Change of Temperature and effect of this change on hardness, sliding velocity, contact pressure, wear coefficient, are the main contributor of die failure. The proposed model considered all these parameters. Constant parameters added has been added to the equation to accommodate the change of parameters. This equation was embedded into DEFORM - FE simulation software and screw press energy, temperature and friction coefficient which contribute in inducing wear were included in addition to the parameters mentioned above. This made this equation the best candidate for this work. The hardness values were taken from the literature at different temperatures. For abrasive wear simulation of H13 steel, the constants of a, b , are considered to be 1 and c is considered to be 2. It showed a reasonable result. To confirm this all the constants were considered 1 and then wear value were compared to the practical trial to ensure this is the case. The result was far from reality therefore c was considered 2 while a, b , were considered 1. Wear coefficient was calibrated with the practical trial instead of using lab-based pin on disc approach and other coefficients are experimentally measured. The initial wear coefficient of 6×10^{-6} for steel was used from the literature. It then was modified prior to simulation and practical trial comparison. The new wear coefficient was used as an input to reach the best correlation between simulation and practical trial.

$$Z = K * \left(\frac{p^a v^b t}{H(\text{die})(T)^c} \right) \quad 3.1$$

The subroutine was implemented for adhesion wear along abrasive wear to give the full picture of wear during the forging process. For adhesion change in

hardness of billet which is a function of yield strength was considered and inputted. As adhesion is mainly caused by material transformation from workpiece to the die surface. Therefore, hardness is workpiece hardness instead of die hardness as it shows in equation 3.2

$$Z = k * \left(\frac{P^d V^e t}{H(\text{workpiece})(T)^f} \right) \quad 3.2$$

Where Z is wear depth (mm) P is contact pressure (MPa), V is sliding velocity (mm/s), H is workpiece hardness function of temperature (Rockwell hardness), k is dimensionless wear coefficient which is calibrated by the practical forging trials and t is step time (second), *d*, *e*, and *f* are constants which are material dependent and for Inconel 718 considered to be 1[54].

3.1.2. Tool design

Four-piece die set was designed consisting of a top die, a bottom die, insert and end stop shown on Figure 3-2. The radius of the insert's fillet as shown in Figure 3-2 was set at 1.5 mm which was modified 2mm to reduce the stress concentration and avoid deformation of the tool. The fillet was designed in such a way to introduce shear stress when billet slides on the tool during the forging process. This increases the amount of induced wear. The end stop stops the billet to move to the +X direction and creates a mark on the back of the billet to aid in overlaying CMM scans of the billets for metrology analysis.

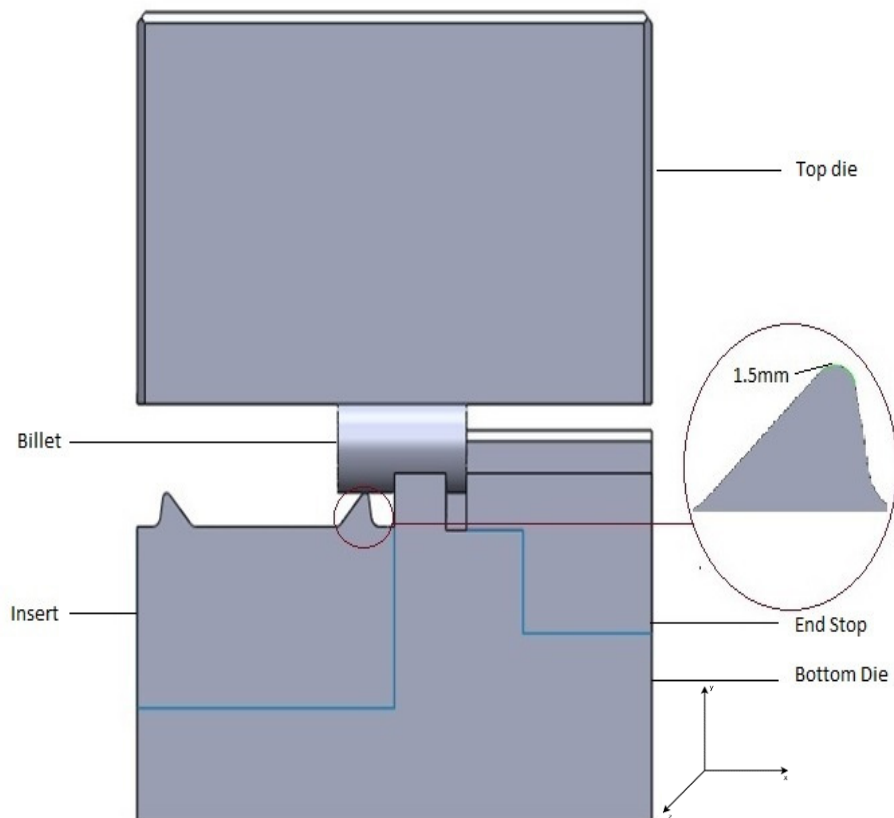


Figure 3-2 : Four Piece die set consisting of Top die, Bottom die, Insert (with fillet radius of 1.5 mm) and End stop

3.1.3.FE Simulation

DEFORM is a Finite Element Method (FEM) simulation system designed to analyse various forming and heat treatment processes used by metal forming and related industries. DEFORM user-friendly interface provides easy data preparation and analysis, fully automated and optimised remeshing system tailored for large deformation made this software candidate for this work [79]. Nonlinear continuum mechanics FE simulation which allows large deformation was used. Large deformation is the lack of elasticity in metal manifested by the fact that when the material is freed from stress it fails to return to the initial undeformed configuration, and instead, permanent deformations are observed. Linear continuum mechanics is valid for processes with a small strain and therefore small deformation [80]. However, linearization naturally leads on to the Newton–Raphson iterative solution, which is the fundamental way of solving the nonlinear equilibrium equations occurring in finite element analysis. The empirical model was validated for open die forging where large displacement was not considered.

The flow stress data for H13 tool steel was taken from tensile tests which were performed at the AFRC (Advanced Forming Research Centre in Inchinnan) by Anderson et al [49] for strain rates of 0.01s^{-1} and 0.1s^{-1} at a temperature range of 250-650 °C using a Zwick/Roell Z250 machine. E21 ASTM standard was followed for the test using samples with the dimensions shown in Figure 3-3. The samples were cut using EDM from the same material which was used for the tool. The flow stress data was extrapolated by the author to a strain of 0.5 using the power law.

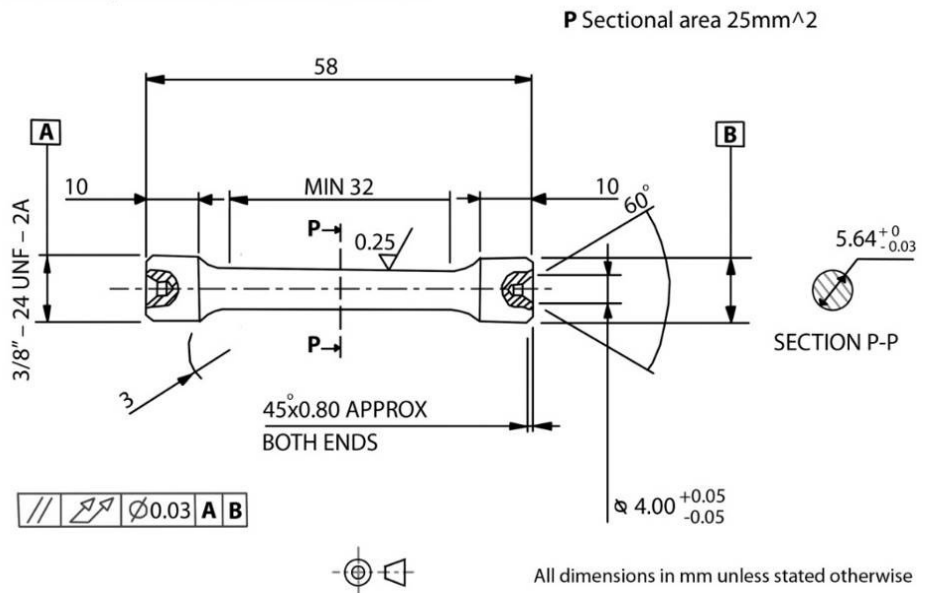


Figure 3-3: Tensile sample dimensions [49]

The flow stress model of Tabular data format was used (equation $\bar{\sigma} = (\bar{\epsilon}, \dot{\bar{\epsilon}}, T)$ 3.3) On the simulation in which flow stress is a function of effective plastic strain, effective strain rate, and temperature.

$$\bar{\sigma} = (\bar{\epsilon}, \dot{\bar{\epsilon}}, T) \quad 3.3$$

$\bar{\sigma}$ = Flow stress

$\bar{\epsilon}$ = Effective plastic strain

$\dot{\bar{\epsilon}}$ = Effective strain rate

T = Temperature

Hardness values for different temperatures were taken from the literature [81]. The tetrahedral mesh size of 0.6 mm was used on the contact area to increase the accuracy of the simulation. The Euler-Lagrangian incremental procedure where

the mesh node point moves with corresponding material points was used [82]. Billet temperature was set based on DOE (Design of Experiments) and bottom die temperature set to 230 °C, while the Top die temperature set at 250 °C. The reason behind the temperature differences between top and bottom bolster is the mechanical setup of the Schuler screw press to prevent jam between the bolsters[4]. The screw press works based on the energy input so energy on screw press was set based on DOE. Die material data was taken from the result of tensile tests. The billet material data was taken from the Deform database (Figure 3-7). The friction coefficient of 0.3 for un-nitrided tool and 0.29 for plasma nitrided tool as by the increase of hardness after plasma nitriding the friction coefficient reduces [83]. The heat transfer coefficient of 11 N/sec/mm/°C [84] was used for the nitrided and un-nitrided tool. The bottom die was constrained on the Y-axis.

3.1.4. The methodology behind adhesive wear Subroutine

For adhesion subroutine implementation, equation 3.2 was used (Summary of the subroutine has been added to Appendix B).

The hardness of slug (i.e. Inconel 718) for different temperatures was calculated based on the relationship between yield strength of the material and their hardness ($HV = 3\sigma_y$). These values were registered as a function of temperature in a text file. Dimensionless wear coefficient (k) is calibrated by forging trial so subject to several changes during the calibration process. While d, e and f coefficients are calibrated based on the materials. It is considered 1 for steel.

3.1.5. Metrology wear measurement technique

For Scanning using CMM, the insert was fixed to the CMM and manually aligned using the top, left and front surfaces. The alignment was repeated automatically three times. A scan line was then taken across the surface of the block. The scan was done using an SP25 probe and points were recorded every 0.05mm. Approximately 400 further scan lines were taken, with spacing between each line of 0.05mm. This generated a file containing the coordinates of approximately 290000 points, covering the area of interest on the part. The coordinates were then loaded into the GOM Inspect software to create a surface mesh. Then the created surface could be compared before and after the forging trial.

3.1.1. Press kinetics

The screw press uses the friction, gear, electric, or hydraulic drive to accelerate the flywheel and the screw assembly, and it converts the angular kinetic energy into the linear energy of the slide of ram for the driving stroke one of the driving discs is pressed against the flywheel by a servo motor. The flywheel, which is connected to the screw either positively or by a friction slip clutch, is accelerated by this driving disc through friction. The flywheel energy and the ram speed continue to increase until the ram hits the workpiece. Thus, the load necessary for forming is built up and transferred through the slide, the screw, and the bed to the press frame.

When the entire energy in the flywheel is used in deforming the workpiece and elastically deflecting the press, the flywheel, the screw, and the slide stop. At this moment, the servomotor activates the horizontal shaft and presses the upstroke driving disc wheel against the flywheel. Thus, the flywheel and the screw are accelerated in the reverse direction and the slide is lifted to its top position[5]. Figure 3-4 a)shows the screw press schematic b) shows 2100 tonnes Schuller screw press in Advanced Forming Research Center.

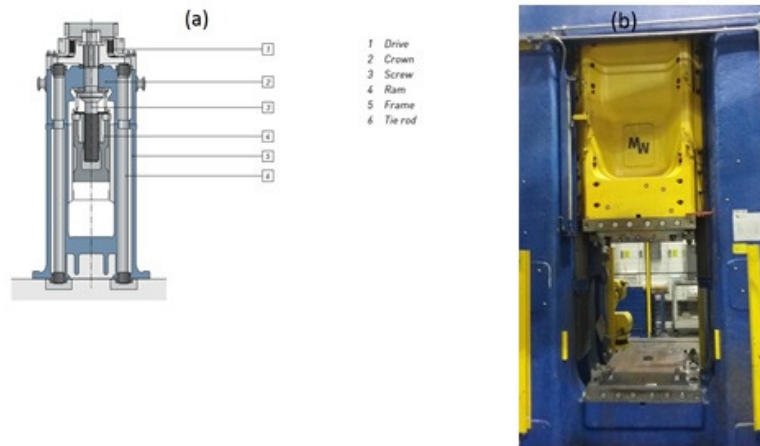


Figure 3-4: a)Screw press schematic b)2100 tonnes Schuler screw press (AFRC)

3.1.1. Thermal Camera imaging

The usual case is to use a thermocouple to measure the direct change of temperature or interface temperature. Thermocouples can be positioned inside the tool or spot welded on the surface of the tool[27]. However, none of these was feasible in this work. The reason was inaccessibility of die because of using screw press for forging . Therefore land thermal camera was used to record the change of temperature on the tool surface.

The land thermal camera was calibrated and used for thermal reading. Arc thermal camera of range 0-500°C, which has an accuracy of $\pm 2\%$ / $\pm 2^\circ\text{C}$ and high-resolution image[85] was compared with the thermocouple reading. An example of thermal camera reading with the emissivity of 0.8 is shown in Figure 3-5. The reading was taken when the billet was out of the view to avoid the effect of illumination.

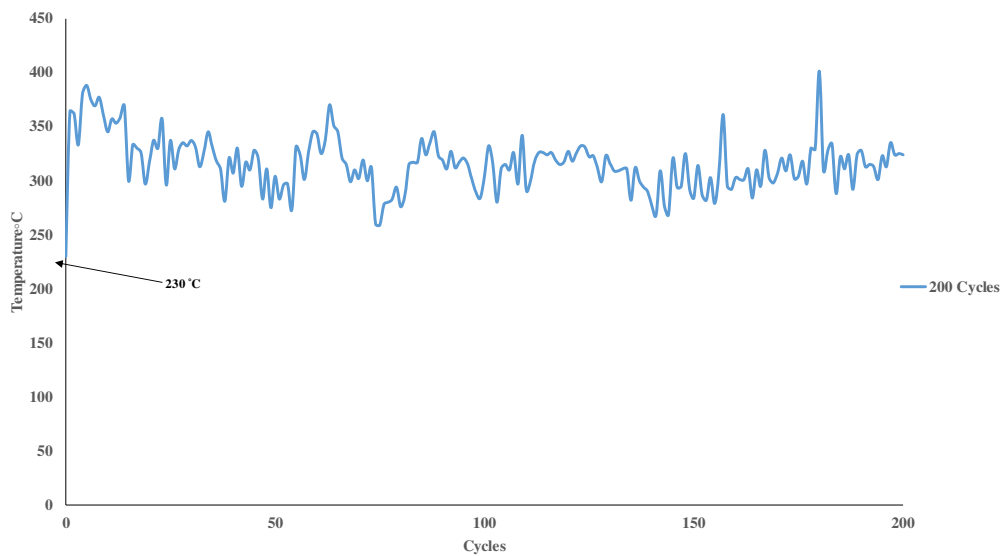


Figure 3-5: Ark Thermal camera for 200 forging cycles

3.2. Experimental tooling and materials

This section will explain the property of:

- Materials which were used for the forging trials,
- The surface treatment which was applied,
- The press which was used,
- Die Surface treatment
- The lubricant which was applied,
- Heat transfer and friction between die and workpiece
- As well as additional equipment which was used for monitoring thermal changes.

3.2.1. Forging of Stainless steel 321

Stainless steel AISI321 was selected for initial forging trials. The rules that apply to the hot upset forging of carbon and alloy steels are also applicable to stainless steel; that is, the unsupported length should never be more than two times the diameter because it might buckle or bend, forcing metal to one side and preventing the formation of concentric forging. Exceeding this limitation can cause non-uniformity around the axis of the forging and encounter edges splitting

of the upset on its outside edges. Die wear increases with the elevated temperature strength of alloys. Different types of stainless steel include austenitic stainless steels, Martensitic stainless steels and Ferritic stainless steels.

- **Austenitic stainless steels**

This kind of stainless steel is more difficult to forge than straight chromium types but is less susceptible to surface defects. Such steels can be forged at higher temperatures (above 930°C) than the Martensitic type because they do not undergo major phase transformation at elevated temperatures.

- **Martensitic stainless steels**

These have high hardenability to the extent that they are generally air hardened. Precautions must, therefore, be taken in cooling and forging of Martensitic steels, especially those with high carbon content, to prevent cracking. They should be cooled slowly to about 590°C. The maximum temperatures for these steels are low enough to avoid the formation of δ -ferrite and to avoid cracking.

- **Ferritic stainless steels**

Ferritic straight-chromium stainless steel exhibits no increase in hardness upon quenching. The degree of work hardening depends on the temperature and the amount of metal flow. The Ferritic stainless steel has a broad range of forgeability, which is restricted at higher temperatures because of grain growth and structural weakness but is closely restricted in finishing temperatures only for type 405. Type 405 requires special consideration because of the grain boundary weakness resulting from the development of a small amount of austenite [86].

Stainless steel 321 is austenitic stainless steel with a titanium content of five times the carbon content. It has a good creep strength and a large amount of titanium makes it resistant to chloride-induced pitting and increases the hardness. A large amount of titanium makes these types of a material harder and increases the chance of creating wear on tool steel. Table 3-2 shows the chemical composition of stainless steel 321 which

was used for forging trial in the Advanced Forming Research Center. The chemical composition of the material was taken from the certificate of conformity (COC Appendix C)

Table 3-2: Chemical composition of Stainless steel 321 from COC

Composition	Wt. %
Titanium (Ti)	0.70
Chromium (Cr)	17-19
Manganese (Mn)	2.00
Silicon (Si)	0.75
Nickel (Ni)	9.0-12.0
Phosphorus(P)	0.045
Sulphur(S)	0.03
Carbon(C)	0.08
Nitrogen (N)	0.1

Flow stress curve of stainless steel at a temperature of 950°C forging temperature and strain rates of 1s⁻¹ and 63 s⁻¹ shown in Figure 3-6 was taken from DEFORM 3D data based.

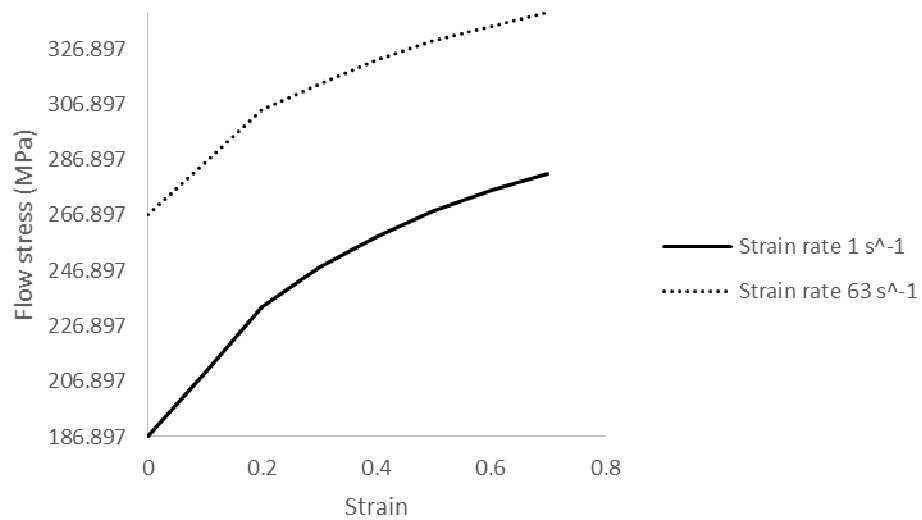


Figure 3-6: Flow stress curve for stainless steel 321 at 950 °C and strain rates of 1s⁻¹ and 63s⁻¹

3.2.2. Forging of Inconel 718

INCONEL® alloy 718 is a high-strength, corrosion-resistant nickel chromium with forging temperature of 900°C to 1120°C [87]. This type of material can easily be shaped into a complex parts when age hardened. Its welding and post welding characteristic are great as well as its resistance to crack. The easy and economical way of fabricating this material makes this material popular for manufacturing different parts especially airfoil blades . Therefore Inconel 718 was used for second parts of this thesis. Table 3-3 shows the material composition of Inconel 718 which was taken from certificate of conformity (COC) . Inconel flow stress data in Figure 3-7 was taken from DEFORM 3D material data . It shows the flow stress at temperature range of 950-1150°C and strain rate ranges between 0.001-100s⁻¹ .

Table 3-3 :Chemical composition of Inconel 718 from COC

Composition	Wt.%
Nickel (Ni)	50.00 - 55.00
Chromium (Cr)	17.00 - 21.00
Niobium (Columbium) (Nb)	4.75 - 5.50
Molybdenum (Mo)	2.80 - 3.30
Aluminium (Al)	0.65 - 1.15
Copper (Cu)	0.20 - 0.80
Iron (Fe) Balance	Iron (Fe) Balance



Figure 3-7: Flow stress curve for inconel 718 a) 900 °C forging temperature b) 950°C forging temperature c)1000 °C forging temperature d) 1050°C forging temperature e) 1100°C forging temperature f)1150 °C forging temperature and all are at strainrates ranges between 0.001-100 s⁻¹[88]

3.2.3. H13 Die material properties

Martensitic H13 tool steel is inclined to lose their mechanical properties, however, the formation of an important oxide scale at the workpiece surface leads to the degradation of a part of its substrate. In the same way, the oxidation of the die and delamination wear can considerably reduce the tool life. At last, a too thick oxide scale on the die surface can influence the flow of the hot material and can delay the cooling effect of the die on the forged piece. All these observations can be concluded to a bad contribution of the oxides in forging. During the hot metal forming process, the forging tools are submitted to thermal and mechanical cyclic stresses. Under such working conditions, tools are usually damaged through complex and interactive mechanisms under cyclic loadings like abrasive, adhesive, thermal and mechanical fatigue and plastic deformation [8][89]. Table 3-4 shows the chemical composition of H13 tool steel from certificate of conformity COC.

Table 3-4: Chemical composition of H13 tool steel from COC

C	Si	Mn	Cr	Mo	V
0.4	1	0.4	5.2	1.4	1

Anderson et al[49] performed tensile test using ASTM E21 standard followed using a Zwick Z250 screw press at the Advanced forming research center facility. The pre-load of 250N was applied during heating to compensate for thermal expansion of the press. However, because of early fracture in a tensile sample the data had to be extrapolated by authorising the power law. The tensile test shown in Figure 3-8 was done at 250,500 °C temperature and strain rates of 0.01 s⁻¹, 0.1 s⁻¹ and 500,600 °C and strain rate of 0.01.

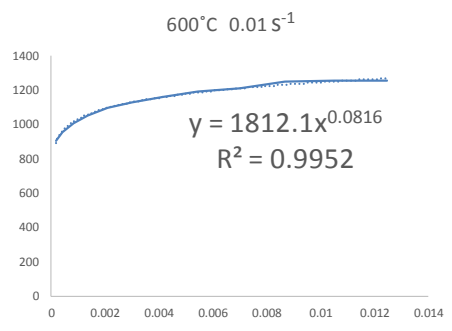
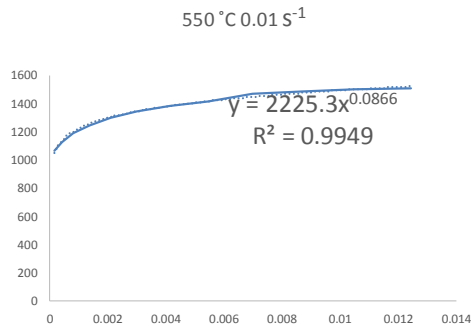
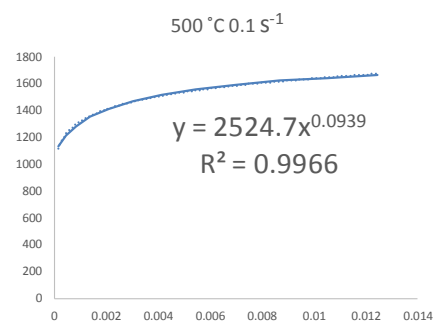
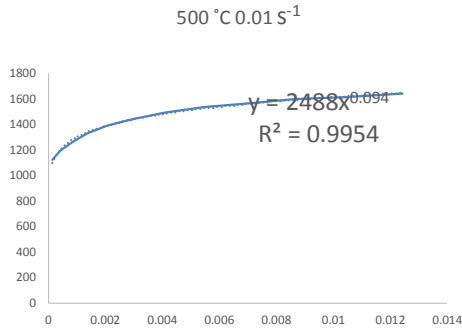
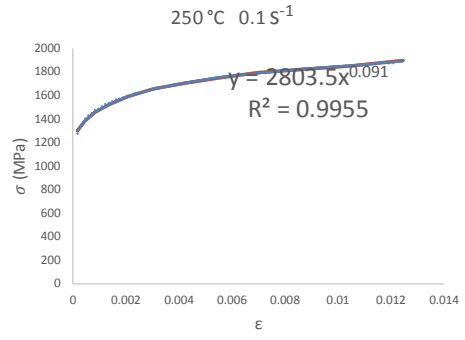
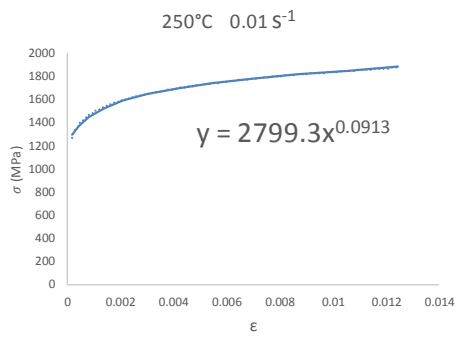


Figure 3-8: Tensile test at 250,500 °C temperature and strain rates of 0.01,0.1 s⁻¹
Tensile test results for temperatures of 550,600 °C and strain rate of 0.01 s⁻¹

3.2.4. Die material surface treatment

The forging trials were performed mainly on dies without surface treatments, except for a nitrided trial. Nitriding case depth depends on time and temperature and method of the nitriding, however, while increasing the case depth can increase the surface hardness it can increase that chance of spalling and crack initiation. ASM international [21] suggests that the case depth shallower than 0.13 mm provides the better protection, therefore, die for nitrided trial was plasma nitrided to the case depth of 0.1mm.

3.2.5. Lubricant,

The main difference between the cold and hot forging lubricant is the temperature range in which lubricants have to function and it makes the lubricant selection extremely difficult, because of the high temperature of forging using organic based graphite are not suitable as they burn. The soap-based lubricants will melt at this temperature. Therefore water-based graphite, synthetics, and glass-based lubricant are suitable. The graphite layer remains on the dies after evaporation of other aqueous (solution in which the solvent is water) solution[5]. Water-based graphite lubricant with 10% solid content was used for forging trials. The graphite layer cools the die surface as well as reducing the friction between the die and the workpiece.

3.2.6. Heat transfer and Friction

For determining friction factor for shear factor m as shown in equation 2.3, usually ring compression test is being performed considering both lubrication and cooling effect. Appropriate heat transfer coefficient has to be selected between the workpiece and die when running a simulation. In metal forming, the magnitude and distribution of temperature according to Altan et al. depends on the initial temperature of die and workpiece, heat generation due to plastic deformation and friction at the die and workpiece interface, heat transfer between the workpiece and dies and environment considering the cooling effect of air and lubricant.

However, in forging, the metal flow is a nonsteady state. The length of contact time and the nature of the heat transfer at the die and workpiece interface influences the temperature considerably [5]. The heat transfer coefficient of 11 N/sec/mm/°C and the friction coefficient of 0.3 was selected for hot forging simulation. The simulation result showed a good agreement with a practical forging trial when Stainless steel 321 and Inconel 718 was forged on H13 tool steel.

3.3. Experimental procedure

To establish a measurement method the first step was to create measurable amounts of wear. Therefore, the design of experiments was used for simulations to find an optimum setting for forging trials. Deform 3D software was used for the simulation. The wear model was implemented in simulation using random wear coefficient which was calibrated using practical trial. For establishing the setup and increasing the amount of wear, different types of billet materials were used like aluminum, stainless steel 316, 321. However only stainless steel 321 showed some trace of wear. Later, decided to use Inconel 718 which is harder compared to stainless steel 321 and because of the popularity of using this type of material for aerofoil manufacturing. Different methods of measurements were experimented to measure tool and workpieces using Infocus optical microscope (Alicona) and CMM.

3.3.1. Wear model calibration

The wear models (equation 2.4, 2.5) were calibrated using simulation and practical trials. The steps shown on the diagram were taken for the calibration. a, b, c, d, e, f, are material dependent while k (wear coefficient) depends on load, contact pressure, temperature, sliding velocity, hardness, friction, and many other factors. It must be measured practically.

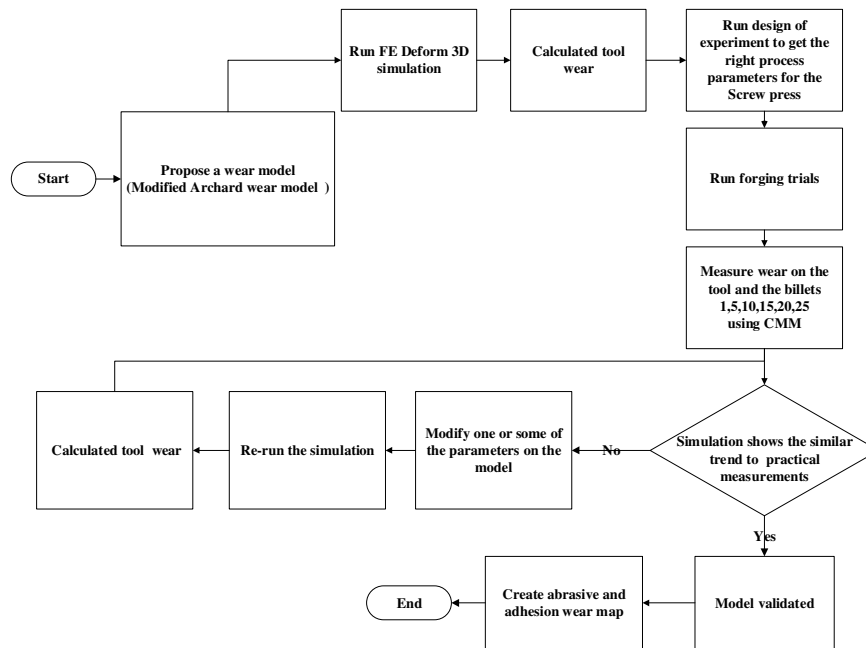


Figure 3-9: Wear model calibration steps

A random wear coefficient was used based on the literature. Abrasive and adhesive wear then were predicted using the FE simulation. These wear values were compared to the wear values which were measured on the tools and parts after forging trials. Based on this comparison the wear coefficient was updated to reduce the error between FE simulation wear prediction and measurement wear on the tool and parts. Following this methodology, the k values were calibrated for all the trials.

3.3.1. Forging trials steps

The forging trial steps started by picking up the billets one by one from the rack and placing them inside the furnace. There are 36 holders inside the rotating stage of the furnace. The billets soaked for 15 minutes inside the furnace before forging. The insert is sprayed by water-based graphite lubricant before picking a billet from the furnace and placing it on the insert and forge it. Forging duration for each billet was 0.035 second . After forging the billet was removed and placed inside a tray. Then these steps were repeated for the rest of the billets. Figure 3-10 shows the mentioned steps of the forging trials.

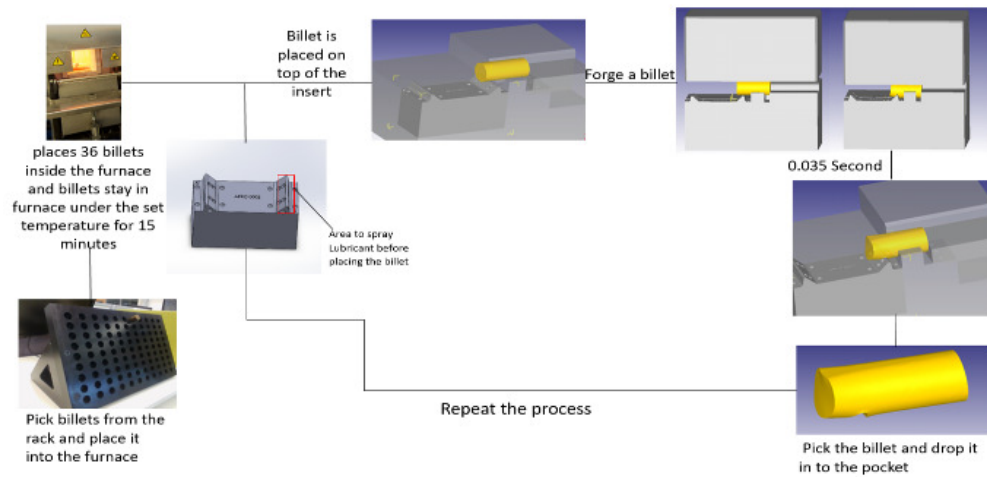


Figure 3-10: Forging trial steps

3.3.2. Stainless steel 321 trials

3.3.2.1. Design of experiments for 321stainless steel trials

To establish a measurement method the first step was to create measurable amounts of wear. Full factorial design of experiment was used on 321 Stainless steel simulations (Table 3-5) to find the optimum setting for the experiments to create the maximum wear.

Table 3-5: Full factorial design of experiments for 321stainless steel trial

Mini tab software was used for 8 runs and 3 levels which means 24 total runs. 80.46% of the variation in Wear could be explained by the model. Mini tab software was used to find the optimum setting.

Table 3-6 Full factorial design of experiments for 321stainless steel trial

Run	CenterPt	Blocks	Billet T	Energy	Lubricant
1	0	1	1050	15	No
2	0	1	1050	10	Yes
3	1	1	1150	5	Yes
4	0	1	1050	10	No
5	1	1	950	5	No
6	1	1	950	10	Yes
7	1	1	950	5	Yes
8	1	1	1150	5	No
9	0	1	1050	10	Yes
10	1	1	1150	15	No
11	1	1	950	15	No
12	1	1	1150	15	Yes
13	-1	2	950	10	No
14	-1	2	950	10	Yes
15	-1	2	1050	5	No
16	0	2	1050	10	No
17	0	2	1050	10	Yes
18	0	2	1050	10	No
19	-1	2	1150	10	Yes
20	0	2	1050	10	Yes
21	-1	2	1050	5	Yes
22	-1	2	1050	15	Yes
23	-1	2	1150	10	No
24	-1	2	1050	15	No

3.3.2.2. 3D Finite Element Simulation

Deform 3D software was used for the simulation. A rigid plastic simulation model was used for wear measurements and elastoplastic model for stress and strain measurements. The flow stress data for H13 tool steel was taken from the tensile test which was performed at the AFRC facilities for stain rates of $0.01s^{-1}$ and $0.1s^{-1}$ at the temperature range of 250-650 °C[49]. The flow stress data were extrapolated up to a strain of 0.5 by the author using the power law. Stainless steel 321 flow stress data were taken from the Deform FE softwear database. The hardness for stainless steel 321was calculated using the relationship between hardness and yield strength at high temperature, Vickers hardness results were converted to Rockwell hardness to be inputted into simulation [90]. The tetrahedral mesh was used for die set and billet considering smaller element size on critical contact areas. The subroutine for adhesive and abrasive wear which introduced in research methodology section on this thesis was activated. A friction coefficient of 0.3 and a heat transfer coefficient of 11 N/sec/mm/°C was used. Cyclic simulation for different runs of the design of experiments was performed. The result was inputted in Minitab to find the trial settings which can create a

measurable amount of wear. Minitab results showed that billet temperature of 950°C, 10 % energy on screw press, and using lubricant creates maximum wear on the tool.

3.3.2.3. **Forging trials**

100 Stainless steel 321 billets were forged on H13 tool steel. Billets were placed inside the furnace to soak for 15 minutes. The screw press was set on 10% of energy and the point of impact was set on 60mm. Graphite water-based lubricant (with 10 % solid content) was used to lubricate the die before and after forging of each billet. Then the billets were placed on the die and forged in turns. Later, the tool and some of the forged parts were taken to the metrology lab to be measured.

3.3.2.4. **Tool and workpieces measurement procedure**

3.3.2.4.1. **Tool measurement procedure**

Three methods of measurements were initially proposed for tool wear measurements:

- GOM ATOS

The ATOS series of industrial optical 3D scanners [91] uses blue light to provide detailed scan of the complex geometries at high speed. ATOS captures full surface geometry of the object precisely in a dense point cloud or polygon mesh. However, it fails to capture the shiny surface. To improve the process anti shine spray being applied on the surface. However not automated procedure of applying this type of material on the surface means high level of variation on the thickness of the applied layer. As in wear study we are looking at the micron level therefore this method of measurement will be questionable.

- Infocus Optical Microscope (Alicona)

An Alicona Infinite Focus G4 Optical Microscope was used, which can produce a surface scan with repeatability of 1.2 % according to type 1

repeatability study. It has a large range of different illumination sources, which makes the measurement of slope angles exceeding 80° possible. The part was secured on a fixture (Figure 3-11) which was placed on the Alicona tray to reduce the vibration and increase the accuracy[92].



Figure 3-11: Fixture for Scanning an insert on Infocus Optical Microscope

- MITUTOYO CRYSTA APEX C coordinate measurement machine (CMM)

In a later stage, a MITUTOYO CRYSTA APEX C coordinate measurement machine (CMM) was used to scan the insert before and after the forging trial.

Probing speed of 3mm/s to 6mm/s scan was used. Description of coordinates as follow:

- CS1: manual alignment: align base plane ZX to 3point plane on the front face of the block. The 3 point line on left-hand side face & 3point line on the top face intersected to create origin in XZ. Left line aligned to z-axis. Coordinate system rotated 180deg around the Z axis
- CS2-4: auto alignment, looped 3 times: align base plane to 15-points plane on the front face of the block. 7point line on top face & 7- points line on the left face, intersected to create origin in XZ.

Left line aligned to the Z axis. Coordinate system rotated 180deg around Z axis.

- CS5: manual alignment used for measurement of dimples on angled face only. 3-points line measured left to right on angled plane, intersected with front plane measured for CS4 to create origin in XY. X axis aligned to 3- points line as shows on Figure 3-12.

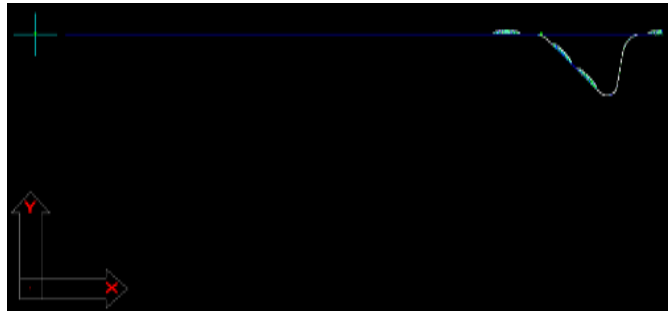


Figure 3-12: Manual and automated alignments (3 points alignments)

- CS6: auto alignment, looped 3 times, used for measurement of dimples on angled face only. 5-points line measured left to right on angled plane, intersected with front plane measured for CS4 to create origin in XY. X axis aligned to 5-points line, Figure 3-13.

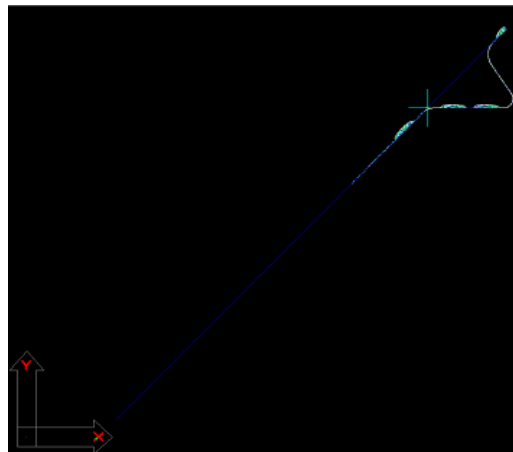


Figure 3-13 : Auto alignments, looped three times and used for measurement of dimples

For Scanning using CMM, the insert was fixed to the CMM and manually aligned using the top, left and front surfaces. The alignment was repeated automatically three times (Figure 3-14).

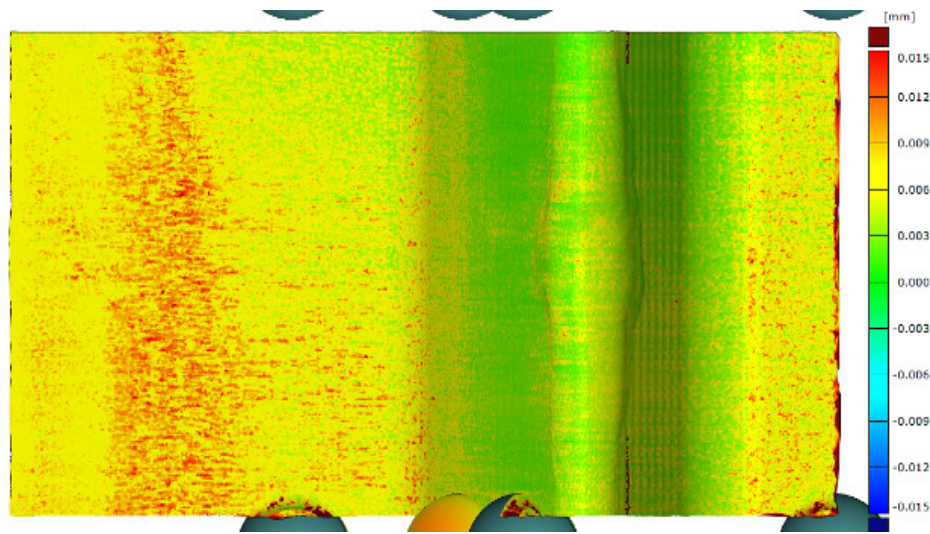


Figure 3-14: An example of repeating Scanning of the same part for 3 times without moving the part.

A scan line was then taken across the surface of the block. The scan was done using an SP25 probe and points were recorded every 0.05mm. Approximately 400 further scan lines were taken, with spacing between each line of 0.05mm. This generated a file containing the coordinates of approximately 290000 points, covering the area of interest on the insert (37 x 20 mm) and for dimples 15 points (3 circles of 7, 5, 3 points) x 8 spheres (Figure 3-15). The coordinates were then loaded into the GOM Inspect software to create a surface mesh. Then created surface could be compared before and after the forging trial[92].

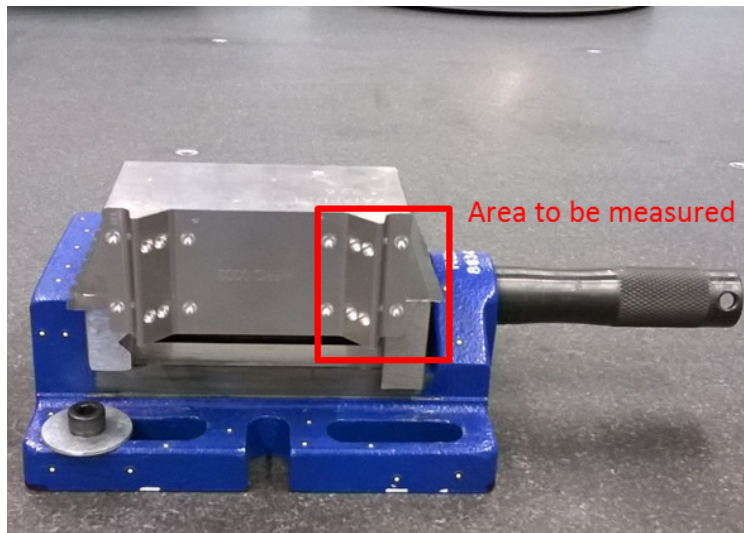


Figure 3-15: Insert fixed on the CMM table with indication of the area of interest

The coefficient of thermal expansion for H13 tool steel is $11 \times 10^{-6} \text{ K}^{-1}$, part size is 100mm x 70mm x 45mm, and therefore expansion is approx. $1 \mu\text{m}$ on the 100mm length per 1°C temperature change Figure 3-16.

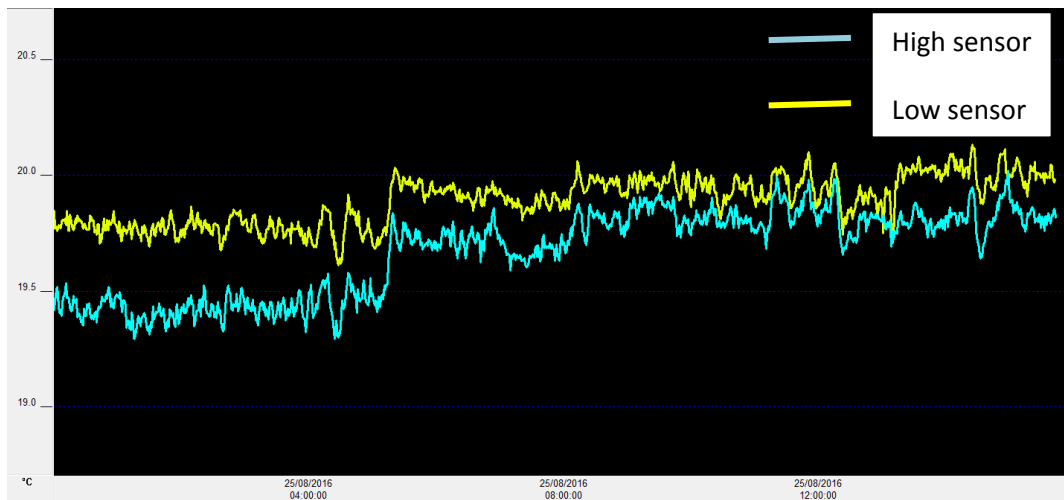


Figure 3-16: H13 Tool Temperature profile during the measurement

3.3.2.4.2. **Workpiece measurement procedure**

For Billet measurement 0.7 mm CMM's probe was used for measurement.

- One billet was measured 17 times. The part was left in position and the CMM program run repeatedly overnight. The measured points were then loaded into the GOM ATOS software, converted to meshes, aligned and loaded into a stage file (following the process described in more detail in the inspection procedure in the checklist section of this document). The range of variation across all 17 parts can be seen below in Figure 3-17. This shows variation under 10 microns for most of the surface.

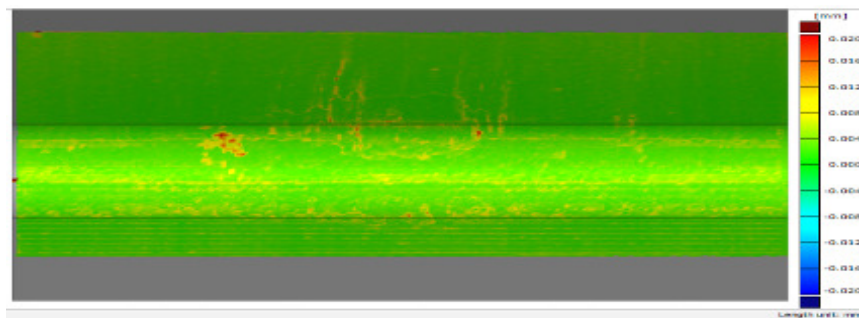


Figure 3-17: Variation for all 17 parts which were overlaid

The stage file compared the measured billets against both a CAD model and a best-fit cylinder. The max deviation on both sides of the cylinder comparison was outputted as shown on Figure 3-18.

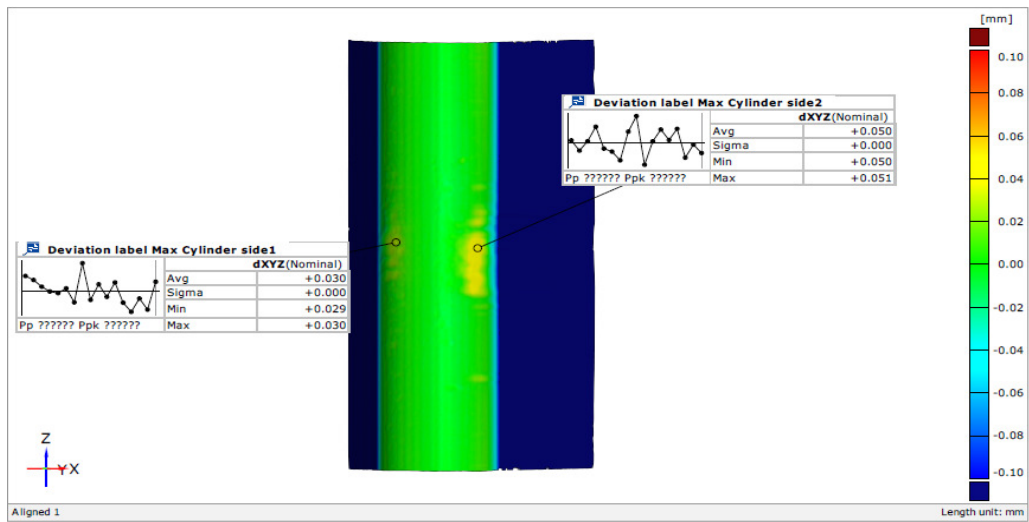


Figure 3-18: The maximum deviation on both sides of the cylinder comparison
 The maximum and minimum deviation to CAD was calculated in two ways, as shown Figure 3-19. The first method took the max and min deviation points across the full mesh and the second took the max and min points in the main area of interest i.e. the central area of the part.

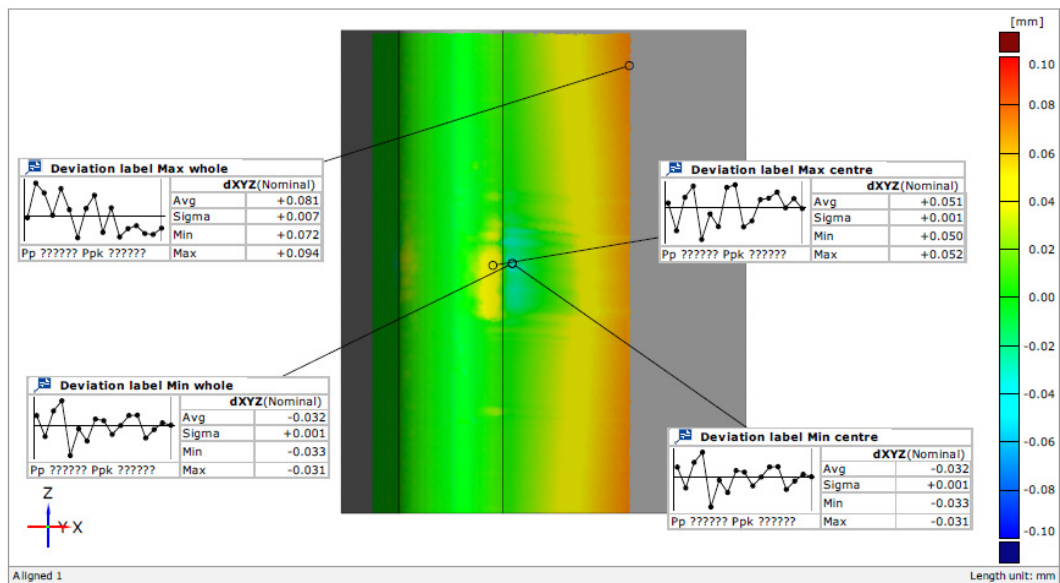


Figure 3-19: Two ways of calculating maximum and minimum deviation to CAD model

The coefficient of expansion for Stainless steel 321 is $13 \times 10^{-6} \text{ K}^{-1}$, part size is 25mm \varnothing x 50 mm, and therefore expansion is approximately 0.6 μm on the 50mm length per $^{\circ}\text{C}$. Figure 3-20 shows the thermal change during CMM measurement. The temperatures were recorded by the high sensor and low sensors on CMM panel. Because the CMM is quite high and the top is near to the air con vent, therefore one sensor is down at the level that the part sits at and another one is up near the top of the machine just to make sure there isn't a huge difference between the two.

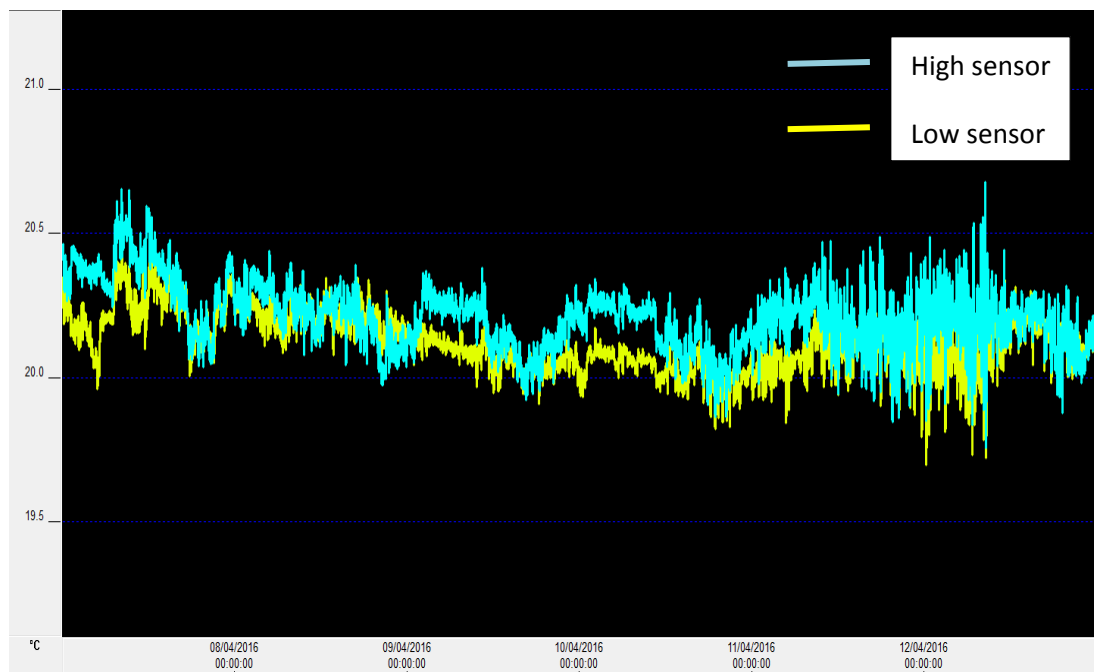


Figure 3-20: Thermal change of 321 Stainless steel billets during the CMM measurements

The maximum and minimum values from both the CAD and cylinder comparison were then used in the type 1 study shown in Table 3-7. The tolerances were set at $\pm 0.05\text{mm}$ as no tolerance has been defined for the parts. This shows that the measurement is repeatable, with the only measurement that is unacceptable being the one which finds the max deviation to CAD using the whole surface of the part.

This point is at the very edge of the part. This is the area that will have the greatest variation in the measurement, meshing and aligning process, but is also the area that is of least interest. Standard deviation i.e. square root of the sum of all the measurement deviations divided by number of measurements-1. Six sigma, is 6 x the sigma value and %Var is six sigma divided by the total tolerance range (in this case 0.1) then multiplied by 100 to get it as a percentage.

Table 3-7: The maximum and minimum values from both the CAD and cylinder comparison The tolerances were set at +/-0.05mm as no tolerance has been defined for the parts

Upper Tolerance Limit (UTL)	0.050	0.050	0.050	0.050	0.050	0.050
Target	0.030	0.050	-0.032	0.051	-0.032	0.081
Lower Tolerance Limit (LTL)	-0.050	-0.050	-0.050	-0.050	-0.050	-0.050
Tolerance Range	0.100	0.100	0.100	0.100	0.100	0.100
	Deviation label Max Cylinder side1	Deviation label Max Cylinder side2	Deviation label Min centre	Deviation label Max centre	Deviation label Min whole	Deviation label Max whole
AVERAGE	0.030	0.050	-0.032	0.051	-0.032	0.081
Sigma	0.0005	0.0002	0.0006	0.0008	0.0006	0.0072
6 * Sigma	0.0031	0.0015	0.0034	0.0050	0.0034	0.0430
% Var	3.09%	1.46%	3.37%	4.99%	3.37%	42.97%

Scanning speed of 3mm/s was used, CMM scanned approximately 62500 points in area of (12mm x 6.5mm) and 4mm deep.

Figure 3-21 shows the notch area that was scanned using 0.7mm CMM prob.

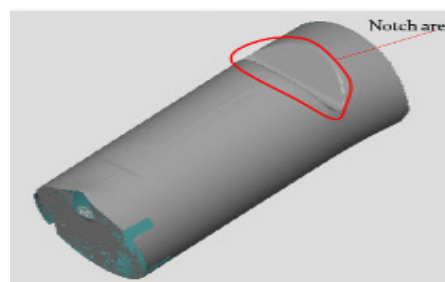


Figure 3-21: Notch area which was scanned by 0.7 mm CMM's probe

3.3.3. Inconel 718 trials

3.3.3.1. Design of experiments for Inconel 718 trials

Full factorial design of experiments was used on simulation to find the optimum trial setup. Billet temperature and screw press energy were considered as two variables with three levels (Table 3-8).

Table 3-8: Full factorial design for Inconel 718 experiments.

StdOrder	RunOrder	PtType	Blocks	Billet Temperature	Screw Press Energy
6	1	1	1	1085	16
13	2	1	1	1085	8
18	3	1	1	1120	16
8	4	1	1	1120	11.2
17	5	1	1	1120	11.2
12	6	1	1	1050	16
15	7	1	1	1085	16
11	8	1	1	1050	11.2
9	9	1	1	1120	16
7	10	1	1	1120	8
10	11	1	1	1050	8
2	12	1	1	1050	11.2
14	13	1	1	1085	11.2
4	14	1	1	1085	8
5	15	1	1	1085	11.2
1	16	1	1	1050	8
3	17	1	1	1050	16
16	18	1	1	1120	8

3.3.3.2. 3D Finite Element Simulation

A rigid plastic simulation model was used for wear measurements and elastoplastic model for stress and strain measurements. The simulation setup was used as per a design of experiments result. Inconel 718 flow stress data was taken from the Deform database. The hardness for Inconel 718 was calculated using the relationship between hardness and yield strength at high temperature, Vickers

hardness results were converted to Rockwell hardness to be inputted into simulation [93]. Nine simulations were performed. The wear values were inputted in Mini tab to create a measurable amount of wear. 1050°C billet temperature and 10% energy on screw press showed the maximum wear. Hardness values for different temperatures were taken from the literature (Benedyk J.C 2008). The tetrahedral mesh size of 0.6 mm was used on the contact area to increase the accuracy of the simulation. The Euler-Lagrangian incremental procedure where mesh node point moves with corresponding material points was used (Euler-Lagrange 2008).

3.3.3.2.1. H13 Material Data

The flow stress data for H13 tool steel was taken from tensile tests which were performed at the AFRC (Advanced Forming Research Centre in Inchinnan) by Anderson et al [49] for strain rates of $0.01s^{-1}$ and $0.1s^{-1}$ at a temperature range of 250-650 °C using Zwick/Roell Z250 machine. E21 ASTM standard was followed for the test using samples with the dimension shown on Figure 3-22.

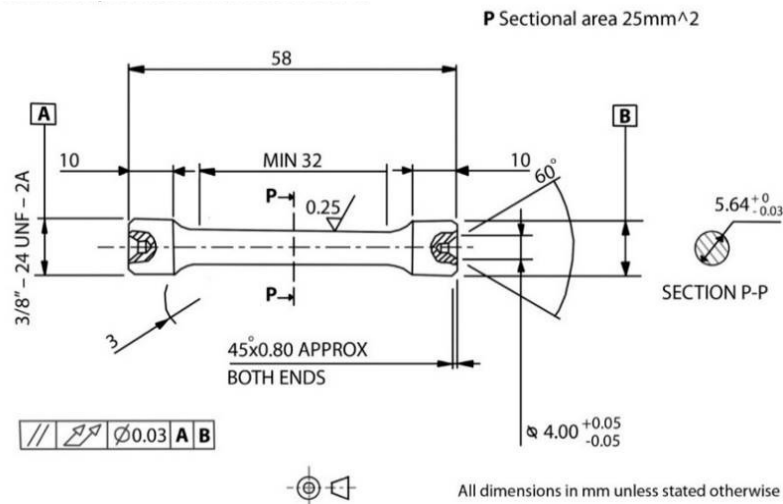


Figure 3-22: Tensile sample dimensions [49]

The flow stress model of Tabular data format was used ($\bar{\sigma} = (\bar{\epsilon}, \dot{\bar{\epsilon}}, T)$ 3.4) on the simulation in which flow stress is a function of effective plastic strain, effective strain rate, and temperature.

$$\bar{\sigma} = (\bar{\epsilon}, \dot{\bar{\epsilon}}, T) \quad 3.4$$

$\bar{\sigma}$ = Flow stress,

$\bar{\epsilon}$ = Effective plastic strain,

$\dot{\bar{\epsilon}}$ = Effective strain rate,

T = Temperature.

3.3.3.3. **Forging trials**

The same forging trial procedure was used as of forging 321 stainless steel billets on H13 tool steel. Land thermal camera with the temperature range of 0-500 was set up and emissivity of 0.8 was used.

3.3.3.4. **Tool and workpieces measurement**

3.3.3.4.1. **Tool measurement procedure**

For H13 tool measurement the same procedure as previous trials were used.

3.3.3.4.2. **Workpiece measurement procedure**

The coefficient of expansion for Inconel 718 is $12.8 \times 10^{-6} \text{ K}^{-1}$, part size is 25mm \varnothing x 50 mm, and therefore expansion is approximately 0.6 μm on the 50mm length per $^{\circ}\text{C}$. Figure 3-23 shows the thermal change during CMM measurement of the Inconel 718 billets. The temperatures were recorded by the high sensor and low sensors on CMM panel.

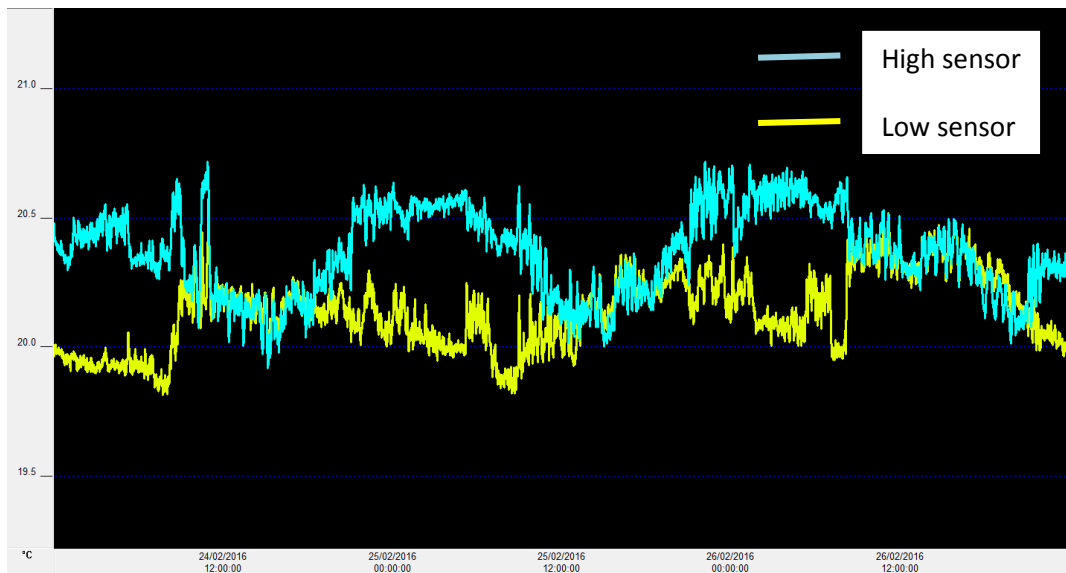


Figure 3-23: Inconel 718 billet thermal change during CMM measurements

3.3.4. Comparing Simulation wear prediction result to the Practical Wear Measurement

To compare the simulation wear results with CMM measurement wear results, multiple profiles were created on the worn surface of the tool after cyclic simulation. The position of the profiles was identified by X, Y, Z coordinates of the start and end point of profiles. Then these values were used to create the section on CMM measured surface. This could increase the accuracy as the wear values were taken from a similar area. The downside of this method was that it couldn't be representative of maximum wear on the tool as the profiles couldn't cover all the worn surface. Therefore, another method was proposed and used by taking all the wear results of the worn surface from the simulation and finding the minimum and maximum wear value. This then was compared to the highest and lowest wear value results from the CMM measurement after measuring tool before and after forging trial. The other issue was that measuring tool after each forging cycle was not feasible as the tool must be removed from the screw press and placed again. It would create an additional variable and would be very time to consume [94]. Therefore, the new method of measurement method was proposed to measure the workpiece instead of tool assuming that the change in the shape of the notch in workpiece shows the change on the tool during the forging cycles.

This method reduces the cost involved in the operation and minimises the variables and therefore increases the accuracy. Then the measured workpiece can be compared to the measured tool at the end of the forging cycles to confirm the accuracy of the procedure.

3.3.5.H13 Tool Deformation

As much as die material selection is important in protecting the die from the failure, workpiece material selection also has a huge influence on tool life because of interaction between the two materials. Nitriding and surface coating can improve die resistance to wear, deformation, heat checking, thermal fatigue, and mechanical fatigue by increasing surface hardness and reducing the friction between die and workpiece [95], [96]. However, from studying all the factors and interaction between them which influence the tool life it is clear, that there is no general recipe for increasing tool life[43]. For the project hardened and un-nitrided H13 tool steel without any coating layer was used to investigate the deformation behavior of H13 tool steel. A four-piece die set, including top die, bottom die, insert and end stop was used as shown in Figure 3-24. The radius of the fillet on the insert was 1.5 mm.

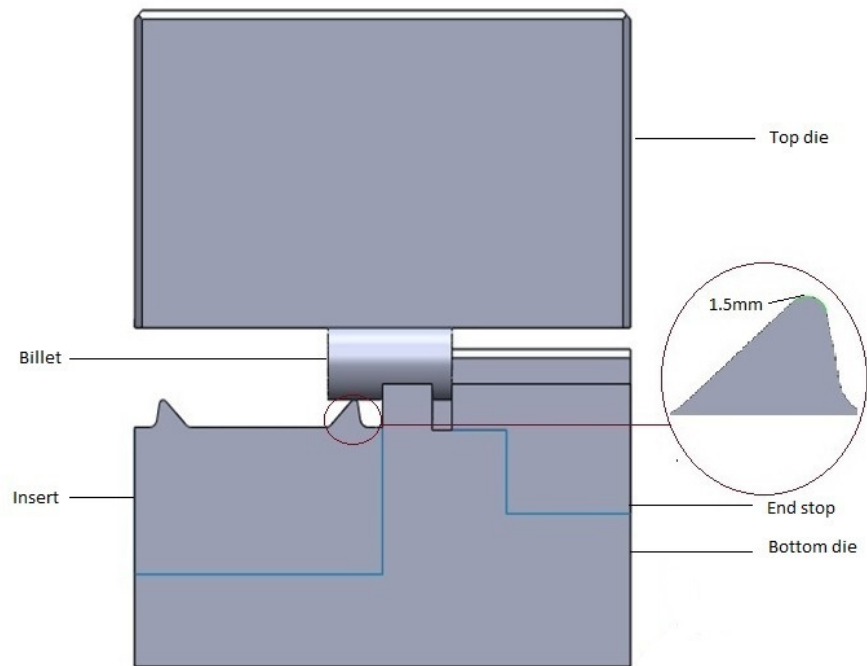


Figure 3-24: Four Piece die set consisting of Top die, Bottom die, Insert (with fillet radius of 1.5 mm) and End stop

Following the forging cycle, the insert showed evidence of deformation and adhesion (Figure 3-25b). Forging dies deform elastically during the forging process. However, plastic deformation is irreversible and results in die failure [97]. Therefore a further investigation was necessary to understand H13 tool steel behavior under elevated temperature and excessive load[98]. The understanding of the non-uniform deformation and work hardening of the material is of critical importance. Deformation at high temperature on the tool is down to localised stress and strain and the increase of dislocation density which initiates the recrystallization [99]. Tempered hot work tool steels microstructure (i.e. tempered H13) consist of tempered martensite with high dislocation density [100]. This piece of work is devoted to investigating the deformation on hardened H13 tool steel by using different types of analysis including nonlinear continuum 3D FEM simulation, Vickers micro-hardness analysis, SEM and EBSD analysis.

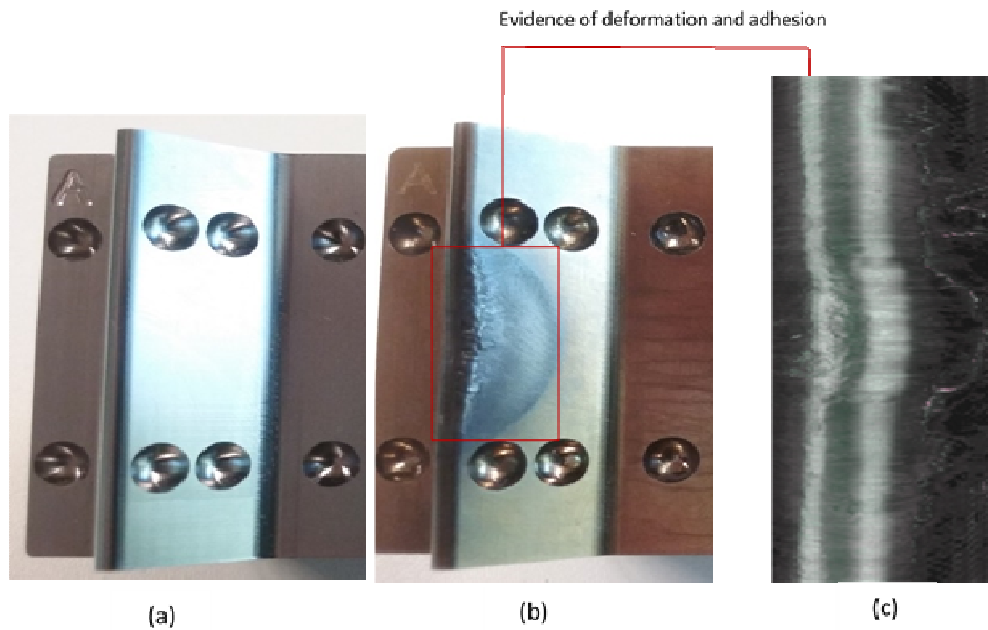


Figure 3-25:a) Insert image before forging, b) Insert image after forging showing evidence of deformation and adhesion, c) magnified area of the deformation and adhesion

3.3.5.1. Experimental setup to investigation tool deformation

3.3.5.2. Simulation

The result of 3D Deform simulation showed high localised stress and high strain of 0.38 on the sharp edge of the tool. Therefore, microstructure and microhardness study were necessary. The first step was to perform an elastoplastic simulation using 3D Deform software. Nonlinear continuum mechanics allows large deformation. Linear continuum mechanics is valid for processes with a small strain and therefore small deformation[101]. The flow stress data for H13 tool steel was taken from tensile tests which were performed at the AFRC (Advanced Forming Research Centre in Inchinnan) by Anderson et al. (Anderson et al., 2013) for strain rates of 0.01s^{-1} and 0.1s^{-1} at a temperature range of 250-650 °C using Zwick/Roell Z250 machine. E21 ASTM standard was followed for the test using samples with the dimension shown in Figure 3-22. The samples were cut using EDM from the same material which was used for the tool. The flow stress data was extrapolated by the author up to a strain of 0.5 using the power law. The flow

stress model of Tabular data ($\bar{\sigma} = (\bar{\varepsilon}, \dot{\varepsilon}, T)$) 3.4)

format was used on the simulation in which flow stress is a function of effective plastic strain, effective strain rate and temperature (1). Hardness values for different temperatures were taken from the literature [81]. The tetrahedral mesh size of 0.6 mm was used in the contact area to increase the accuracy of the simulation. The Euler-Lagrangian incremental procedure where the mesh node point moves with corresponding material points was used [82]. The simulation was run in two steps to consider loading and unloading. An elastoplastic simulation model (elastoplastic die and plastic billet) was used for the simulation. The billet temperature was set at 1050 °C and the bottom die temperature to 230 °C, while Top die temperature set at 250 °C. The reason behind the temperature differences between top and bottom bolster is the mechanical setup of Schuler screw press to prevent jam between the bolsters. The screw press works based on the energy input so 16 KJ which is equivalent to 10% of the total 160KJ capability of screw press was used. Die material data was taken from the result of tensile tests. The billet material data was taken from the Deform database. The friction coefficient of 0.3 and the heat transfer coefficient of 11 N/sec/mm/° C was used. The bottom die was constrained on the Y-axis.

3.3.5.3. Experimental setup for microstructure study

For Metallurgical study, the methods defined by Voort and Manilova for tool steel was used [102]. The four steps which were taken as follows:

3.3.5.3.1. Setup for SEM imaging analysis

For microstructure analysis, SEM technique was used instead of a microscope to have a high-resolution and statistically accurate evaluation of the signification deformation that was observed on the tool after forging. Two metallographic samples were prepared from deformed and non-deformed inserts. The fillet of the inserts was cut using EDM then both samples were mounted, ground and polished

as it shows on Table 3-9 . Then mounted samples were placed in vibromet with 0.02 μ m Master Met2 suspension diluted with distilled water for 20% amplitude overnight.

Table 3-9: Grinding and polishing steps used to prepare the samples

Surface	Abrasive / Size	Force [N]	Base Speed [rpm]	Relative Rotation	Time[min]
CarbiMet SiC	P120 grit SiC water cooled	27	240-300		3
CarbiMet SiC	P240 grit SiC water cooled	27	240-300		3
CarbiMet SiC	P400 grit SiC water cooled	27	240-300		3
CarbiMet SiC	P800 grit SiC water cooled	27	240-300		3
CarbiMet SiC	P1200 grit SiC water cooled	27	240-300		3
UltraPol*	9 μ m MetaDi Supreme Diamond*	27	120-150		10
TriDent*	5 μ m MetaDi Supreme Diamond*	27	120-150		8
Microcloth*	0.05 μ m MesterPrep Alumina suspension	27	120-150		5

= Raten = Specimen Holder *Plus MetaDi Fluid Extender as desired

Then, both the samples were investigated in an SEM (Quanta FEG 250) in turn to produce a backscattered electron (BSE) image from the highlighted area. Figure 3-26a, shows the fillet of the insert which was cut using EDM and Figure 3-26b shows the area of interest on the sample.

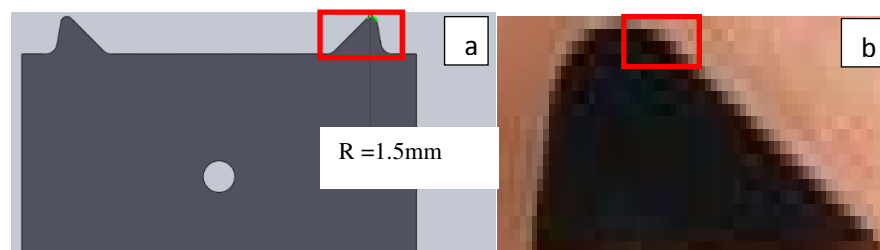


Figure 3-26: a) Fillet on the insert which was cut using EDM b) Interested area on the sample

3.3.5.3.2. **Setup for EBSD analysis**

From the BSE analysis, it was clear that different zone will have a different boundary and therefore different misorientation angles within the grains. To identify this EBSD analysis for microstructure simulation on both the samples were used. It uses indexing to detect bands with different misorientation. It shows how different crystals in the grains are tilted in different axis. The EBSD analysis (HKL system) have been carried out. For EBSD investigations 15 kV voltage, scanning step size of 0.2 μm and 4 \times 4 binning was chosen. The exact area shown in Figure 3-26 was selected for EBSD analysis eliminating the resin mounting area.

3.3.5.4. **Experimental setup for microhardness study**

A Dura Scan 70 G5 Vickers microhardness tester was used to characterise local scale hardness distribution. 25 hardness measurement (5 \times 5 matrix) were taken at depth of 0.6mm from the edge of the sample using 0.12 mm between each indentation with an applied force of 0.5kg/f. The schematic on Figure 3-27 shows the patterns for the hardness test. Then Origin software was used to map the microhardness, considering the distance between the indentations in X-axis and Vickers hardness in Y-axis.

3.3.5.5. **X-ray fluorescence non-destructive analytical technique**

X-ray fluorescence analysis was used to investigate the chemical composition of the adhesive layer on the H13 tool insert.

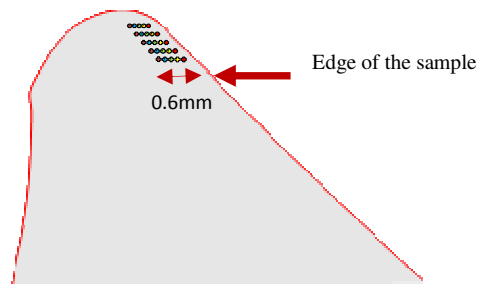


Figure 3-27: Schematic of patterns for micro-hardness test

3.3.6. Tool design change

One of the most important parameters for designing a die is the radius of the die that must be large enough to facilitate the plastic flow of the material avoiding stress concentration that may reduce the useful life of the tools [103]. Fishbone analysis was used to narrow down the causes of die deformation. The result showed that the main cause of die plastic deformation might be because of fillet's radius. The fillet radius was 1.5mm. It was decided to run a simulation for a series of different radius between (2-3mm) to find a suitable radius which can eliminate the deformation while creating a measurable amount of wear. Obviously high-stress concentration on the sharp corners of the die increases the chance of die failure. Therefore, the radius of 2mm showed a promising result based on the simulation results as stress concentration reduced immensely while a still measurable amount of wear was noticed. The simulation result on 3mm tool showed a reduction in both stress concentration and wear. It could be due to sliding velocity reduction. To confirm this a practical trial had to be performed on a 2mm radius tool. Figure 3-28 shows the comparison between 1.5 mm and 2mm insert.

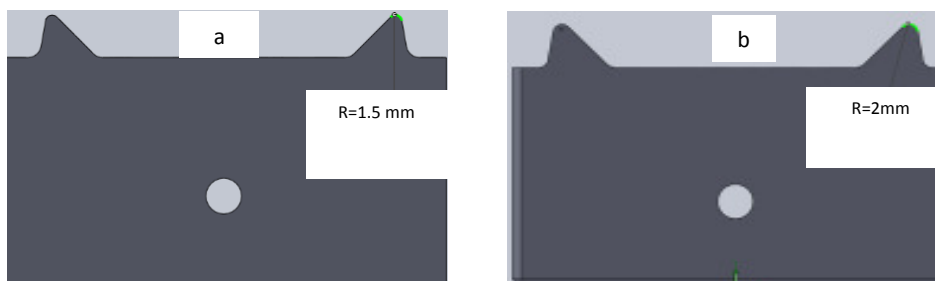


Figure 3-28: a)1.5mm insert b)2mm insert

3.3.7. Wear map trials

For constructing a wear map series of simulations and forging trials were performed based on the design of experiments.

3.3.7.1. Design of experiments for wear map trials

The full factorial design of experiments was performed considering billets temperature and energy on screw press as two variables and each of these variables had 3 levels as shown in Table 3-10. The Minitab result showed 9 trials can give enough points to construct a wear map.

Table 3-10: Full factorial design of experiments for wear map construction

Billets Temperature °C (3Levels)	% Screw Press Energy (3 Levels)
1050	5
1085	7
1120	10

3.3.7.2. 3D Finite Element Simulation

Nine simulations were run based on the results of the design of experiments. Inconel 718 billet H13 tool steel was used. 25 cycles of simulations were performed on 2mm inserts. The wear subroutine was embedded in 3D Rigid plastic FE model using 3D Deform software to calculate abrasive and adhesive wear using equations 3.1 and **Error! Reference source not found..** Hardness values for different temperatures were taken from the literature [81]. A tetrahedral mesh size of 0.6 mm was used in the contact area to increase the accuracy of the simulation. The Euler-Lagrangian incremental procedure where the mesh node point moves with corresponding material points was used [82]. The top die temperature was set at 250°C and the bottom die temperature was set at 230°C. The reason behind the temperature differences between top and bottom bolster is the mechanical setup of the Schuler screw press to prevent jam between the bolsters[4]. A friction coefficient of 0.3 and the heat transfer coefficient of 11 N/sec/mm/°C was used. Initial *K* value was considered 4.5E-06 which was taken from the calibration of the model at 1050 °C and 16KJ energy on a screw press.

Constants a , b , and c on the abrasive model were as $a=1$, $b=1$ and $c=2$ for tool steel. Constants d , e , and, f on adhesion model were 1 for Inconel 718. These values showed a good result after calibrating abrasive and adhesive models. Based on DOE in Table 3-10 nine series of simulation were performed.

3.3.7.3. **Forging trials**

Forging trials were set up according to the design of experiments. After setting the furnace to the forging temperature and setting the screw press energy to the required energy, 25 billets were placed inside the furnace to soak for 15 minutes. Graphite water-based lubricant was sprayed before and after the forging trial. Land thermal camera with the temperature range of 0-500 was set up and emissivity of 0.8[104] was used.

3.3.7.4. Tool and workpieces measurement

The same methods of measurements as the previous trials were used. The wear value obtained from CMM measurements on the billets and the inserts were also compared. A good agreement of 93 % for adhesive wear and 90% for abrasive wear on the billet and insert was established. This is an indication that the degradation of the billet surface reflects changes occurred on the insert. Figure 3-29a, demonstrates Scanning direction on the billets using CMM and Figure 3-29b shows the analysis on the billets 5, 10, 15, 20, 25 which were aligned to the first billet using commercial analysis software. The first billet was aligned to the insert's CAD file. This is an example where billets at the temperature of 1050°C were forged on H13 tool steel using 8KJ energy on a screw press.

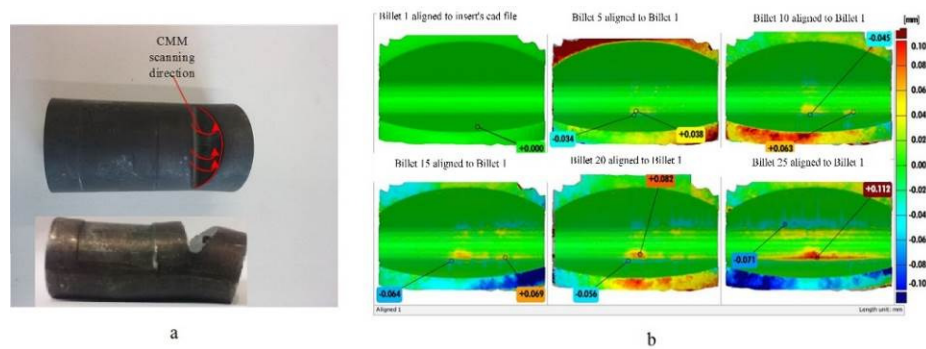


Figure 3-29. a) CMM Scanning direction on the billet after a forging trial (1050°C billet temperature and 8KJ energy on Screw press); b) CMM analysis aligning carried out for billets 5, 10, 15, 20, 25 which were aligned to the billet 1.

3.3.8. Wear map construction

Full factorial design of experiment measure responses at all combinations of the factor levels was used (Table 3-11) for wear map construction instead of a fractional factorial design that uses a subset of a full factorial design, so some of the main effects and two-way interactions are confounded and cannot be separated from the effects of other higher-order interactions. This based on the DOE, simulations and supporting forging trials were planned. Billets temperature and Screw press energy were considered as the two variables. The wear map was constructed considering abrasive and adhesive wear (μm) function of sliding velocity (mm/s) and contact pressure (MPa). Series of wear maps were produced using contact pressure and sliding velocity as two axis and abrasive and adhesive wear as a third axis. Then the data were presented in shapes of scatter plot and colour maps which were superimposed to create detailed wear maps using origin software.

Table 3-11: DOE plan for wear map construction

StdOrder	RunOrder	PtType	Blocks	Billet Temperature	Screw Press Energy
6	1	1	1	1085	16
13	2	1	1	1085	8
18	3	1	1	1120	16
8	4	1	1	1120	11.2
17	5	1	1	1120	11.2
12	6	1	1	1050	16
15	7	1	1	1085	16
11	8	1	1	1050	11.2
9	9	1	1	1120	16
7	10	1	1	1120	8
10	11	1	1	1050	8
2	12	1	1	1050	11.2
14	13	1	1	1085	11.2
4	14	1	1	1085	8
5	15	1	1	1085	11.2
1	16	1	1	1050	8
3	17	1	1	1050	16
16	18	1	1	1120	8

3.3.9. Nitrided and coated trials

Series of FE simulations followed by forging trials were performed on nitrided H13 tools to construct wear maps and for comparison purpose.

3.3.9.1. Simulation

The flow stress data for plasma nitrided H13 tool steel were taken from tensile tests on nitrided tensile samples which were performed at the AFRC (Advanced Forming Research Centre in Inchinnan) by the author. The tensile samples which the dimensions is shown on Figure 3-30 were sent to Bodycote Ltd Birmingham for plasma nitriding. The samples were nitrided to 0.1mm case depth . Tensile tests for stain rates of $0.001s^{-1}$ and $0.01s^{-1}$ at a temperature range of 230-400 °C using Zwick/Roell Z150 machine. E21 ASTM standard was followed for the test.

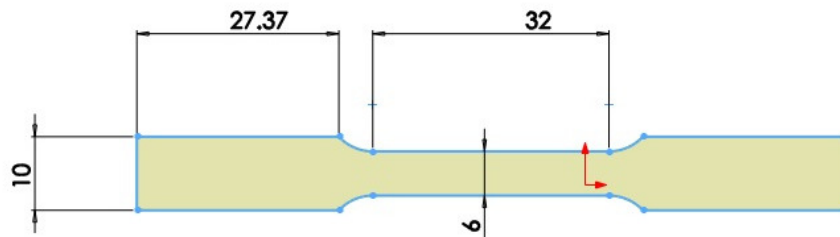


Figure 3-30: Nitrided tensile sample dimension

The flow stress model of Tabular data format was used $\bar{\sigma} = (\bar{\epsilon}, \dot{\bar{\epsilon}}, T)$ 3.3). A Dura Scan 70 G5 Vickers microhardness tester was used to characterise local scale hardness distribution. Cross section of tensile samples after the tensile test at different temperatures and strain rates shown in Figure 3-31a were used for the hardness test. The hardness results in different temperature have been plotted in Figure 3-31b.

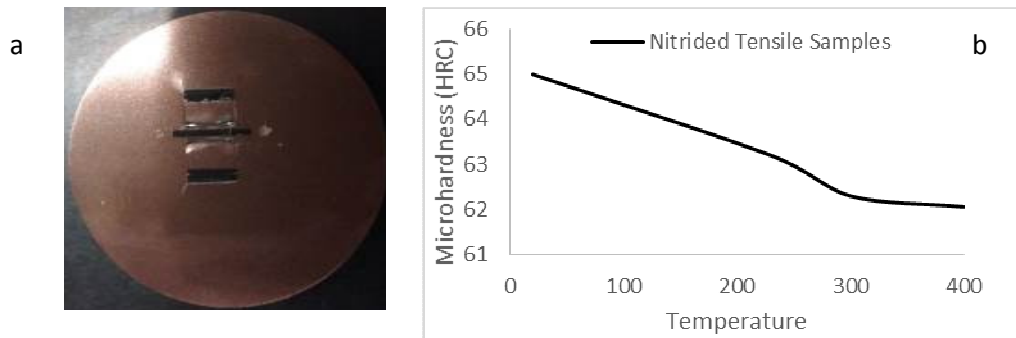


Figure 3-31 a) Picture of cross section b) Hardness on nitrided tensile samples at the different tensile test temperature

Nitrided H13 material data taken from tensile tests at temperature ranges of 230-400 °C and stain rates of $0.001s^{-1}$ and $0.01s^{-1}$ were extrapolated to 0.5 strain as shown in Figure 3-32.

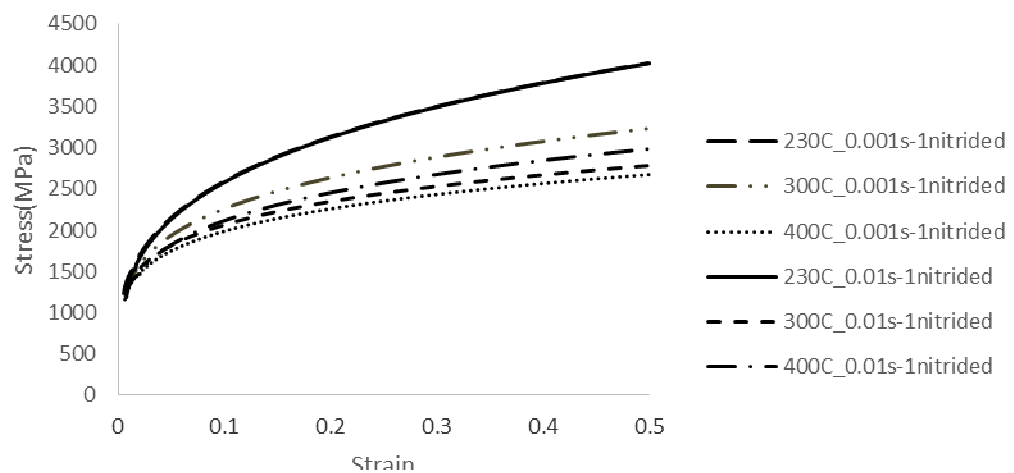


Figure 3-32: Nitrided Stress strain curves at temperture range of 230-400 °C and strain rates of $0.001s^{-1}$ and $0.01s^{-1}$

Nine simulations were run based on the full factorial design of experiment shown in Table 3-10. These were followed by nine practical forging trials then the affected tools and billets wear measured using CMM. To calibrate the wear model the steps shown in Figure 3-9 were followed. The tetrahedral mesh size of 0.6 mm was used on the contact area to increase the accuracy of the simulation. The

Euler-Lagrangian incremental procedure was used as it was used previously for not nitride simulation. Billet temperature was set base on DOE and bottom die temperature set to 230 °C, while the Top die temperature set at 250 °C. The reason behind the temperature differences between top and bottom bolster is the mechanical setup of the Schuler screw press to prevent jam between the bolsters[4]. The screw press works based on the energy input so energy on screw press was set based on DOE. Die material data was taken from the result of tensile tests. The billet material data was taken from the Deform database. The friction coefficient of 0.29 and Heat transfer coefficient of 11 N/sec/mm/°C was used as stated previously in this document. The bottom die was constrained on the Y-axis.

3.3.9.2. **Forging trials**

Forging trials were set up according to the design of experiments. After setting the furnace to the forging temperature and setting the screw press energy to the required energy, 25 billets were placed inside the furnace to soak for 15 minutes. Graphite water-based lubricant was sprayed before and after the forging trial. Land thermal camera with the temperature range of 0-500 was set up and emissivity of 0.8[104] was used.

3.3.9.3. **Flow curve comparison between nitrided and un-nitrided tensile samples**

According to the literature [70] elongation reduces after nitriding on grade 40 and 40x steel but as there is no record of how H13 behaves. Therefore, the author performed additional tensile tests at the same temperature range and strain rates on un-nitrided samples for comparison purpose. The results are shown in Figure 3-33. It shows that the nitrided samples elongate at much higher stress.

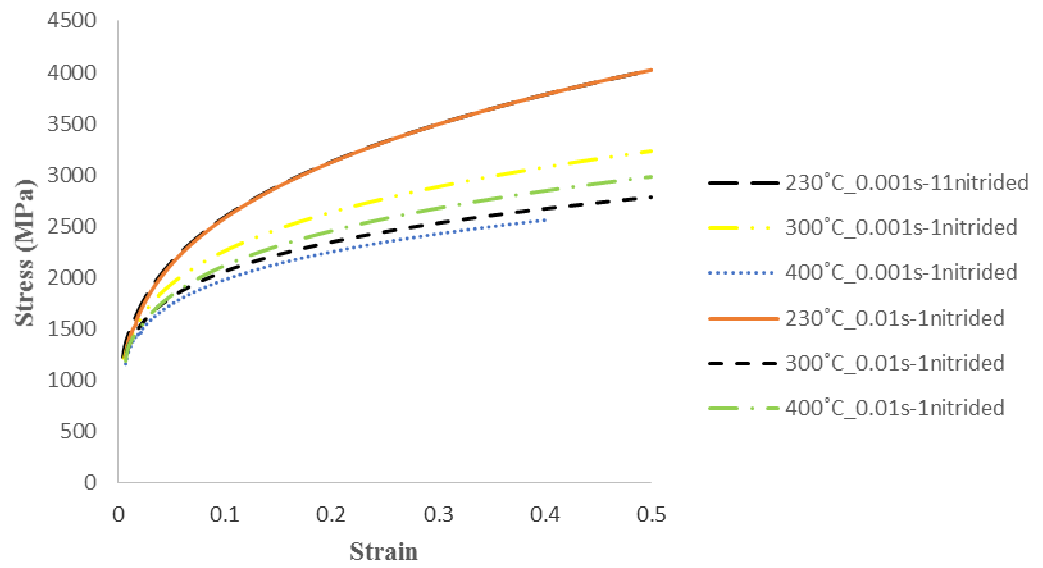


Figure 3-33: Flow curve comparison between nitrided and un-nitrided H13 tool steel at the temperature range of 230°C-400°C and strain rates of 0.001^{s⁻¹} and 0.01^{s⁻¹}

SEM image for a cross section of the nitrified tensile sample after the tensile test at 400°C and strain rate of 0.01s⁻¹ shown in Figure 3-34. The compound layer, $\epsilon\text{Fe}_{2-3}\text{N}$ phase and $\alpha\text{Fe}_{16}\text{N}_2$ precipitate are identified.

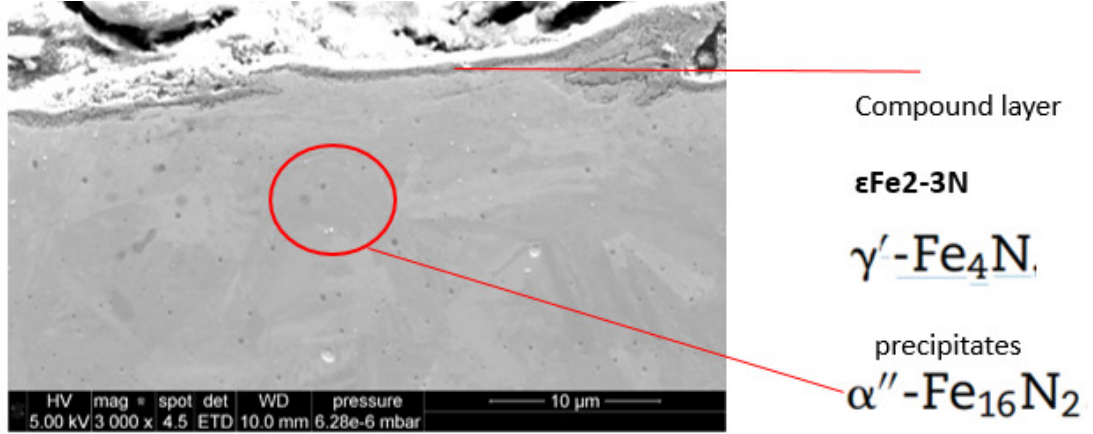


Figure 3-34: Nitrified tensile sample cross section

Chapter 4 Results

4.1. Tool Deformation

4.1.1. XRF (X-ray fluorescence)

XRF result in Table 4-1 shows the chemical composition of H13 tool after forging. 5.4 (Wt. %) of Ni proves that the transferred asperity from Inconel 718 billets was attached to the H13 insert. As when two solid surfaces are in contact, the interfacial bond may be stronger than the cohesive bond in the cohesively weaker of the two materials. In that case, on separation of the two solids, this results in the transfer of the cohesively weaker material to the cohesively stronger. As the focus of this work is on the deformation, therefore, the rest of this work has been devoted to investigating the deformation of H13 tool steel.

Table 4-1: H13 chemical composition after forging (Wt.%)

Si	Cr	Mn	Fe	Ni	Mo	V	Co	Cu
0.4	21.4	1.2	67.6	5.4	3.2	0.11	0.30	0.15

4.1.2. Simulation

After executing the elastoplastic simulation, one point on the stress concentration area was selected for loading and unloading part of the simulation using Deform 3D postprocessor as shown in Figure 4-1.

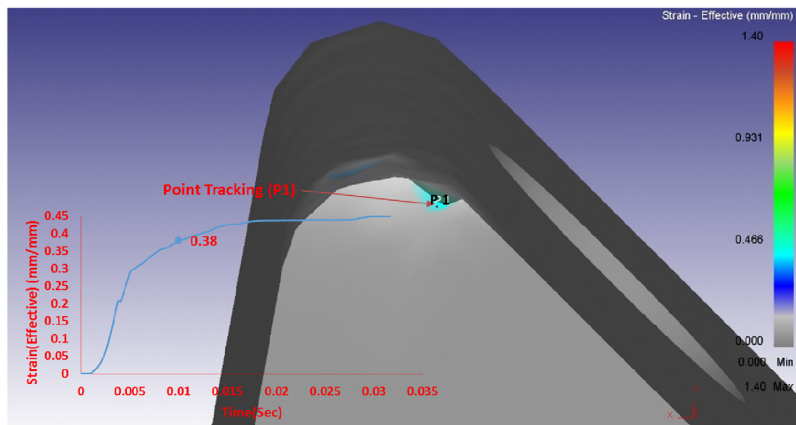


Figure 4-1: One point was selected with maximum stress concentration and high plastic strain of 0.38 on Deform 3D simulation post processor

The results obtained from the thermal camera [85] shows that the die temperature rises in the range of 350–400°C from the initial temperature of 230°C (Figure 4-2). The analysis carried out with the thermal camera were performed for every individual forging blow after removing forged part from the insert from the same point as indicated in Figure 4-1. Therefore, the result has been influenced by air cooling along with cooling caused by lubricants. An emissivity of 0.8 was used for recording the temperatures

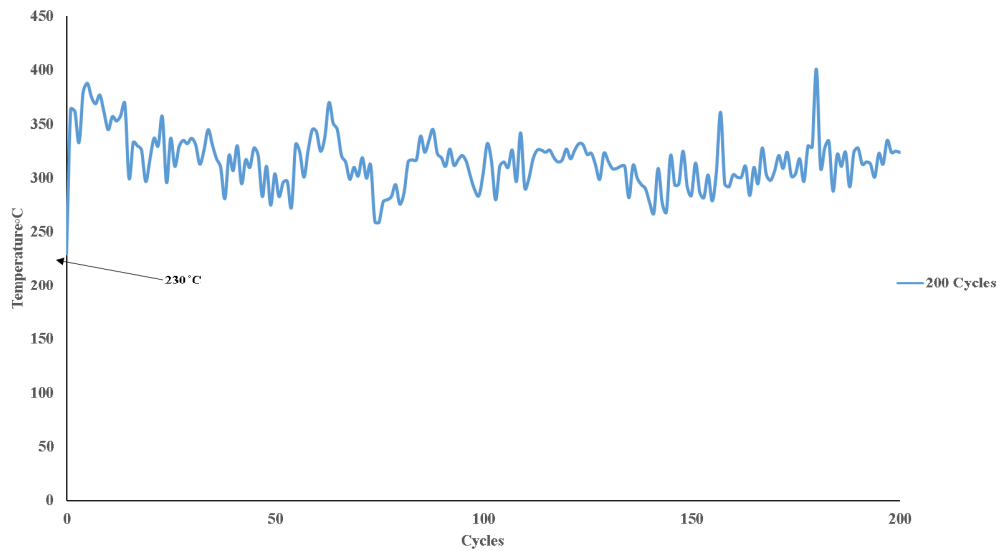


Figure 4-2: Land thermal camera results at an emissivity of 0.8 (± 2 °C accuracy) for 200 cycles of forging (0.035 s for each cycle).

By knowing H13 die temperature during the forging process from thermal camera results, the yield point at this temperature was identified as 1100 MPa from H13 tensile test results as shown in Figure 4-3. Figure 4-3a is true stress-strain curve for tensile test at a strain rate of 0.1s^{-1} and temperature of 400 °C before extrapolation and Figure 4-3b is the result of the same test after extrapolation to 0.5 strain using power law.

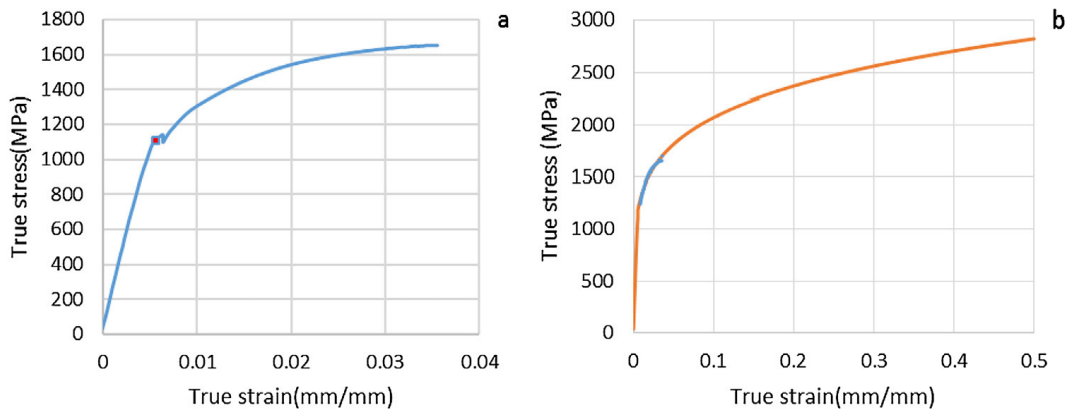


Figure 4-3: a) The tensile test at a strain rate 0.1 s^{-1} and $400 \text{ }^\circ\text{C}$ b) The result after extrapolation to 0.5 strain using power law for the same tensile test.

Therefore, from the stress-strain curve in Figure 4-3 and effective stress curve in which was taken from the simulation result confirms that the material has yielded during the forging process. Furthermore, in wear analysis of dies, at the regions where high effective stresses may occur, the plastic deformation of dies must be also considered[105].

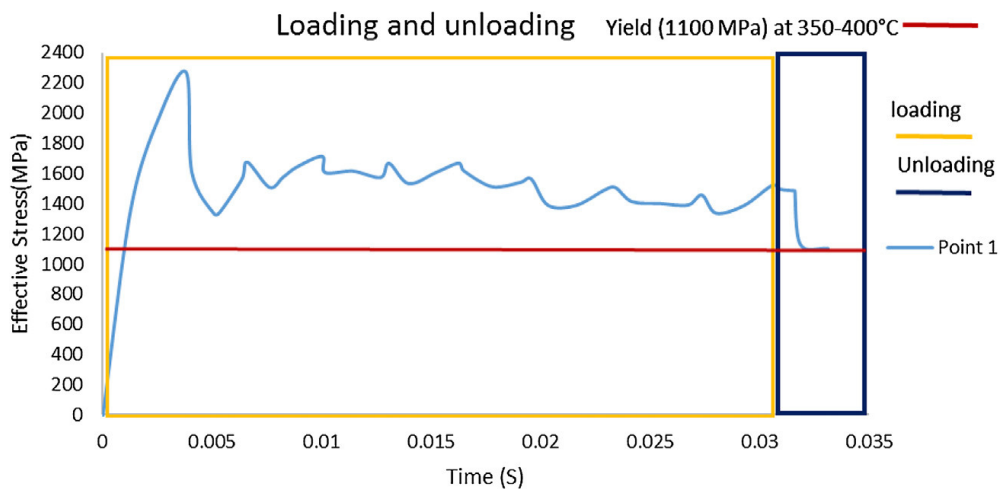


Figure 4-4: Effective stress results from the simulation: an elastoplastic model shows that the yield stress of H13 tool steel was exceeded during forging.

The simulation also shows a high plastic strain of 0.38 (Figure 4-1) after one cycle of forging Inconel 718 on H13 tool steel. This high level of strain alongside with the thermal softening can cause deformation all the way through the forging

process. After hot deformation or during the dwell period between each blow or in final cooling, the material experiences recovery or recrystallization[106]. Static recrystallization (SRX) occurs when new nuclei which are free from the strain form and grow to new grains at the expense of the deformed material [107]. The SRX happens when the strain level is below the critical strain for dynamic recrystallization. The critical microstructural condition, for example, high dislocation density, which occurs when stress in some regions on the surface is much higher than the average stress in the lattice, promotes dynamic recrystallization (DRX). Under this condition, new grains are nucleated and grow while deformation is progressing. When strain level reaches the critical strain, nuclei which have been formed as a result of DRX, progress to metadynamics recrystallization (MDRX) which occurs by constant growth of the nuclei formed by DRX during straining [108].

4.1.3. Microstructure analysis

The high strain achieved on the FE simulation shows that H13 tool steel has gone through deformation. To confirm the simulation results two samples were prepared from deformed and brand-new tools. The same magnification was used, and an image was taken from the same area to increase comparison accuracy. Figure 4-5a shows tempered martensite microstructure which is expected as the tool was not used for any forging process. Figure 4-5b shows BSE images were taken from the samples prior and after forging. The magnified BSE image, including the evolution of the zones is depicted in Figure 4-6, where 1) deformation zone (16% deformation was calculated using image J, 656894 pixels of deform zone / 3864576 pixels all the image), 2) transition between deformation and recrystallization zone, 3) recrystallization zone, 4) transition between recrystallization zone and martensitic zone, 5) martensitic zone.

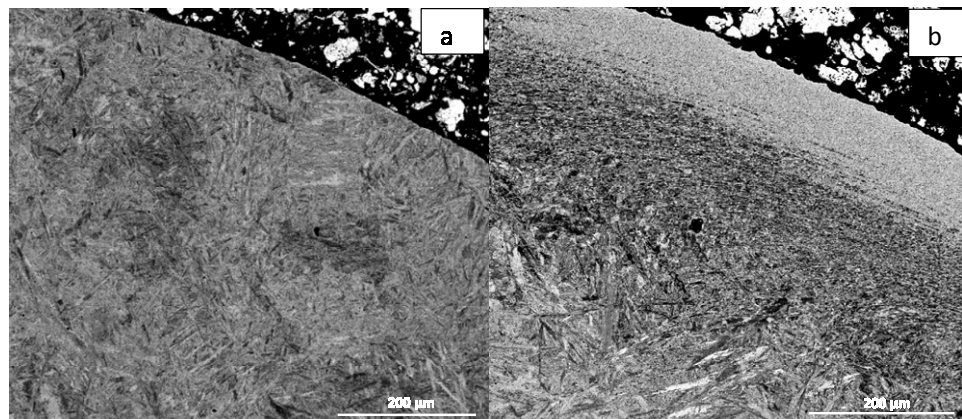


Figure 4-5: BSE images were taken from the H13 tool samples: a) Before forging, b) After forging

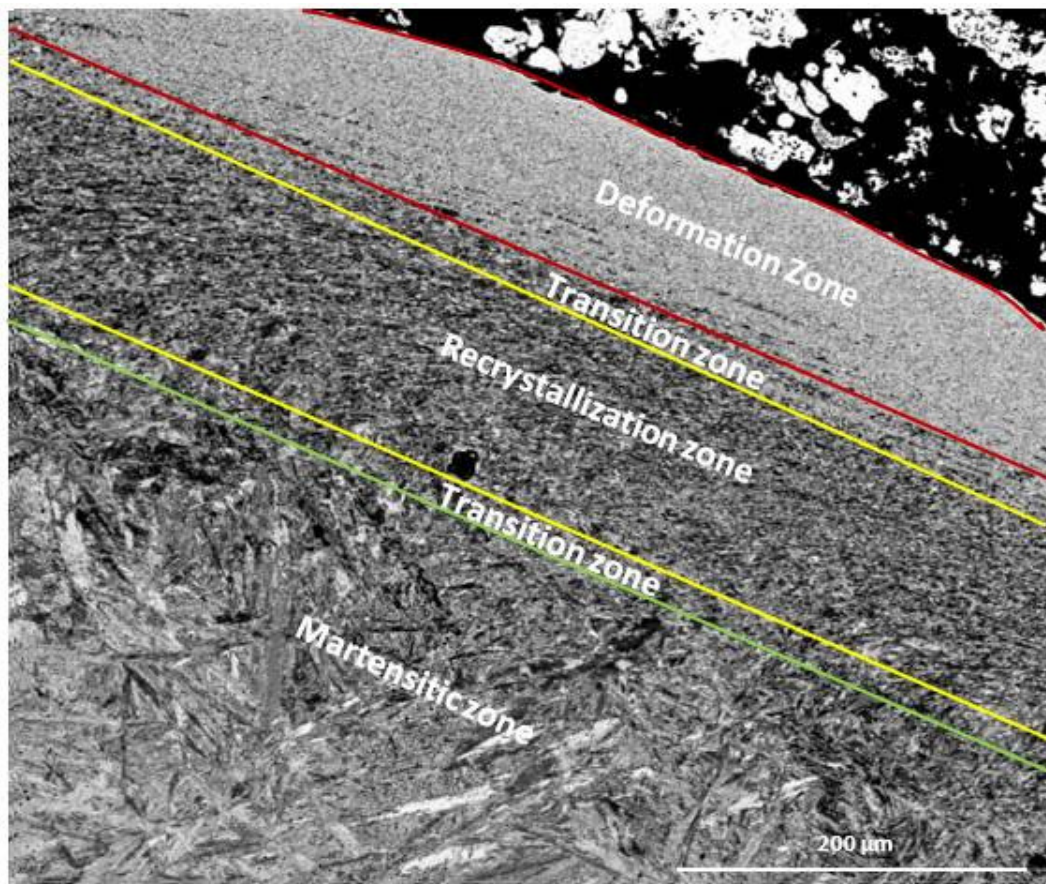
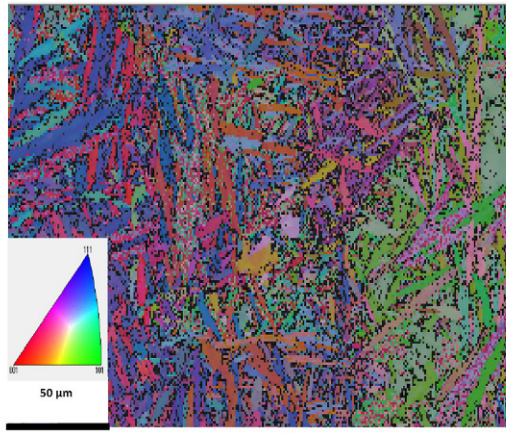
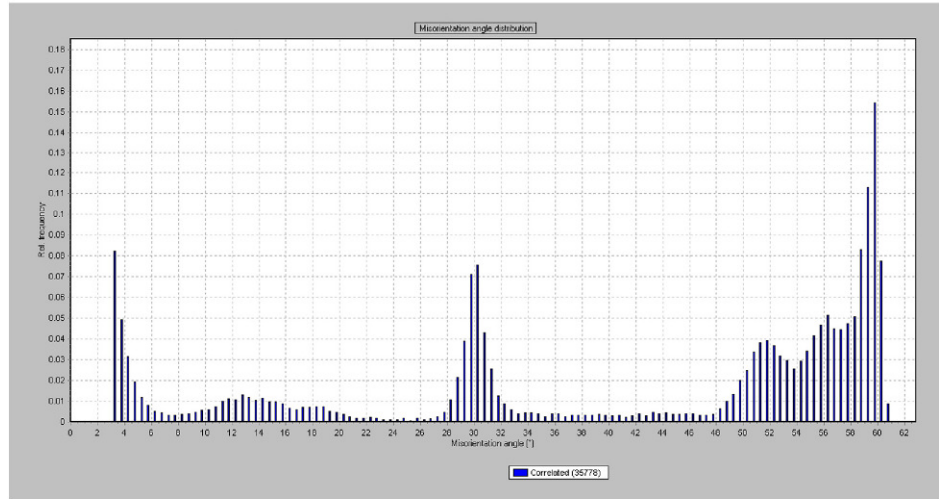


Figure 4-6: BSE images of different zones 1) deformation zone, 2) transition between deformation and recrystallization zone, 3) recrystallization zone, 4) transition between recrystallization zone and martensitic zone, 5) martensitic zone.

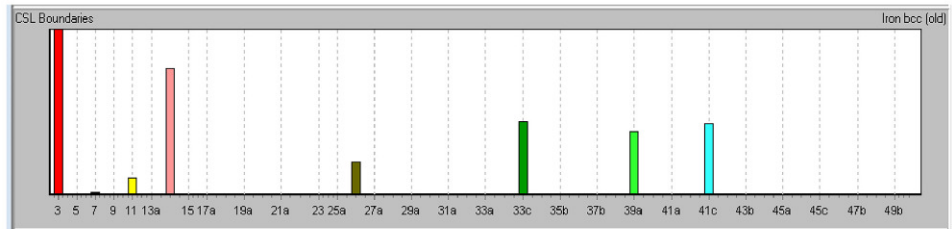
Figure 4-7 shows tempered martensite EBSD map plus analysis and Figure 4-8 shows EBSD maps and analysis of the deformed, recrystallized and martensitic zones obtained at depth of 0.6 mm. In body centered cubic structures (bcc), slip direction normally occurs on planes of the type $\{101\}$ and principal slip direction is along the plane $\{111\}[109]$. Figure 4-7a show the fully tempered martensite microstructure on before forging sample where different grain boundaries including special CSL boundaries of $\Sigma 39a$ were found. Figure 4-7b shows misorientation angles distribution histogram on before forging sample.



a



b

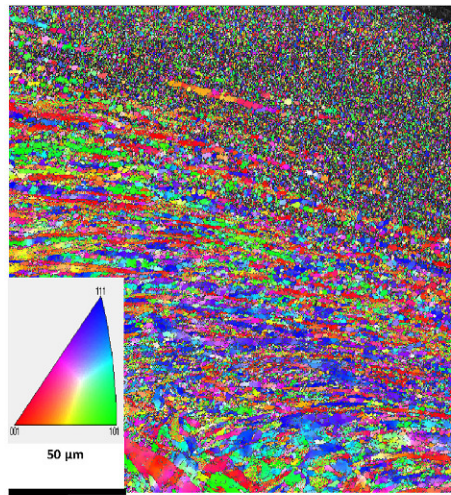


c

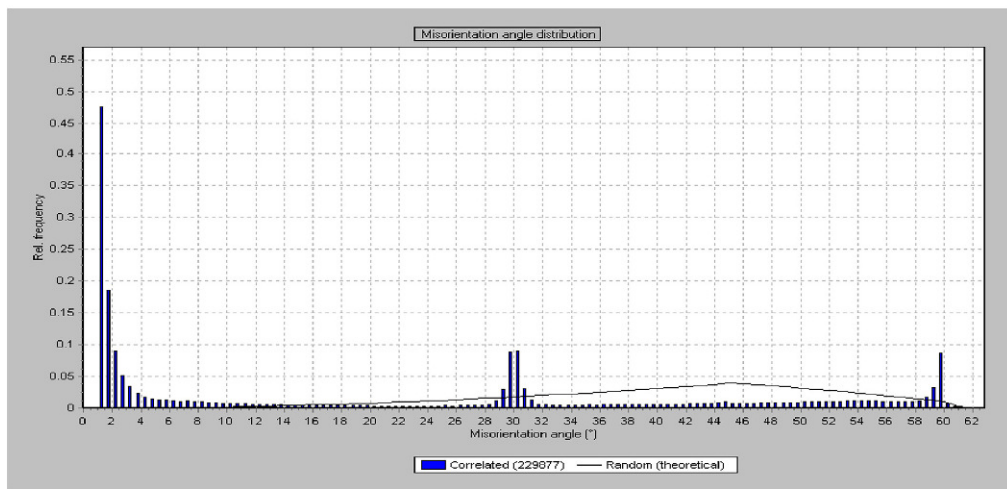
Figure 4-7 : a) IPF (Inverse pole figure) map which was obtained for the sample before forging, b) misorientation angles distribution histogram for the sample before forging, c) CSL (coincident site lattice) special boundaries distribution histogram for the sample before forging.

Figure 4-8a shows different zones including the deformation zone which has been transformed to recrystallized zone in some parts. Figure 4-8b shows the misorientation angles distribution on after forging sample, where an increased fraction of the low angle boundaries (LAB) represents the deformation zone and this is associated with different dislocation substructures caused by slip.

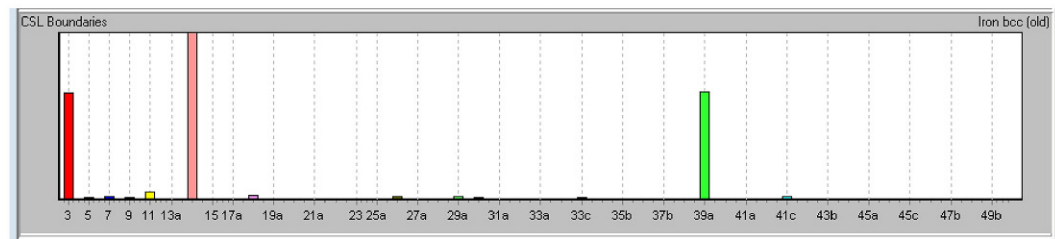
Furthermore, in the middle of misorientation angles graph, the peaks at 28–32° corresponds to special boundaries $\Sigma 39a$ which were created during martensitic lattice transformation when some of the boundaries are not perfectly matched to the rest and transforms to low angle and special boundaries. The high angle boundaries 58–60° correspond to twin boundaries [99].



a



b



c

Figure 4-8: a) IPF (Inverse pole figure) map which was obtained for the sample after forging, b) misorientation angles distribution histogram for the sample after forging, c) CSL (coincident site lattice) special boundaries distribution histogram for the sample after forging.

The result shows that deformation of the tempered martensite leads to the transformation of the initial low and high angle boundaries and formation of the substructure elements. The excessive load and high temperature on screw press cause further increase in dislocation density and transformation of low angle boundary to high angle boundary which has a positive effect on the nucleation of recrystallized grains. Comparison of the histograms depicted on Figure 4-7c with Figure 4-8c shows an increase in some of the boundaries including Σ 13a and Σ 39a and decrease of Σ 3, Σ 11, Σ 33 and Σ 41 which could be formed due to the high temperature and high strain, as misorientation angle is strongly dependent on the strain during high-temperature deformation [110]. The range of measured microhardness on not deformed tool (before forging) was 523–610 HV, while measured microhardness on the deformed tool shows completely a different range 301–600 HV. The results of the microhardness measurements on the deformed tool confirm the evolution of the microstructure and formation of the different zones. Colour map in Figure 4-9a showing the change of microhardness in different zones and Figure 4-9b shows a comparison between the change of microhardness before forging and after forging. Microhardness increases as indentation move away from the edge of the sample. Hardness measurement on pre-forging sample shows values of around 550–600 HV which indicates the suitability of this material under high thermal and load working conditions. As microhardness level depends on the microstructure in the measurement area, the non-uniform microhardness distribution confirms, therefore, the existence of different microstructure zones.

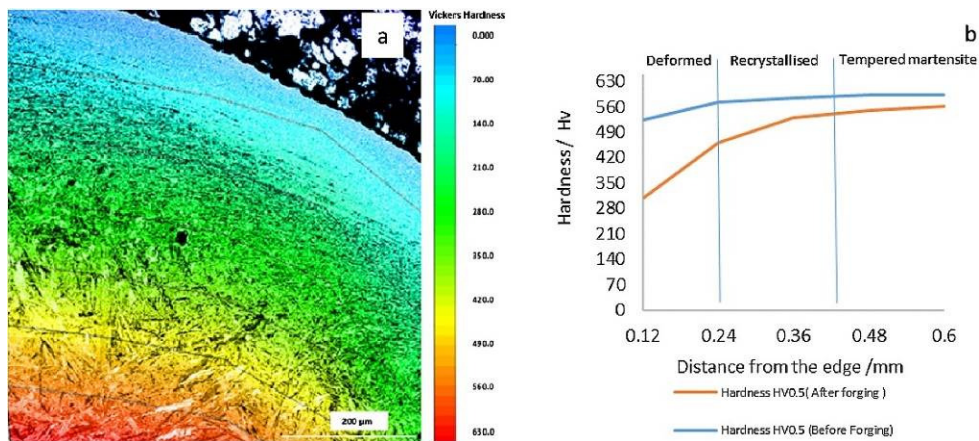


Figure 4-9: a) The colour map showing the change of microhardness in different zones using Origin software and b) Comparison between microhardness levels achieved on before forging and after forging samples.

The microhardness of as-quenched martensitic steels is strongly dependent on carbon content, especially for low and medium carbon steels. The low carbon content of 0.38% (Table 4-2) confirms the insignificant to zero percentage of retained austenite which increases the microhardness.

The microhardness could be preserved by the tempering at low temperature around 150–200°C as it was shown in [111].

Table 4-2: H13 chemical composition (wt.%) from certificate of conformity (COC) compared to the result of X-ray fluorescence analysis.

Conditions	C	Si	Mn	Cr	Mo	V
COC	0.4	1	0.4	5.2	1.4	1
Measured by XRF	0.38	1.2	0.5	5.5	1.75	0.89

4.1.4. Process Improvement

After finding deformation on H13 tool steel, DMAIC process improvement analysis was used to analyse the H13 tool failure and find the solution to minimise or rectify deformation. Cause and effect analysis were used as shown in Figure 4-10 to identify the problem. Fishbone diagram narrowed the problem to tool design. Therefore, it was decided to increase the radius of fillet from 1.5mm to

reduce the stress concentration on the die as failure usually happens in sharp corners. Other solution was to apply a uniform layer of lubricant. The third solution which was recommended after cause and effect analysis to nitride the tool. As previously mentioned, < 0.13 mm nitride layer has been recommended by ASM standard to therefore 0.1mm nitrided layer was applied to the surface.

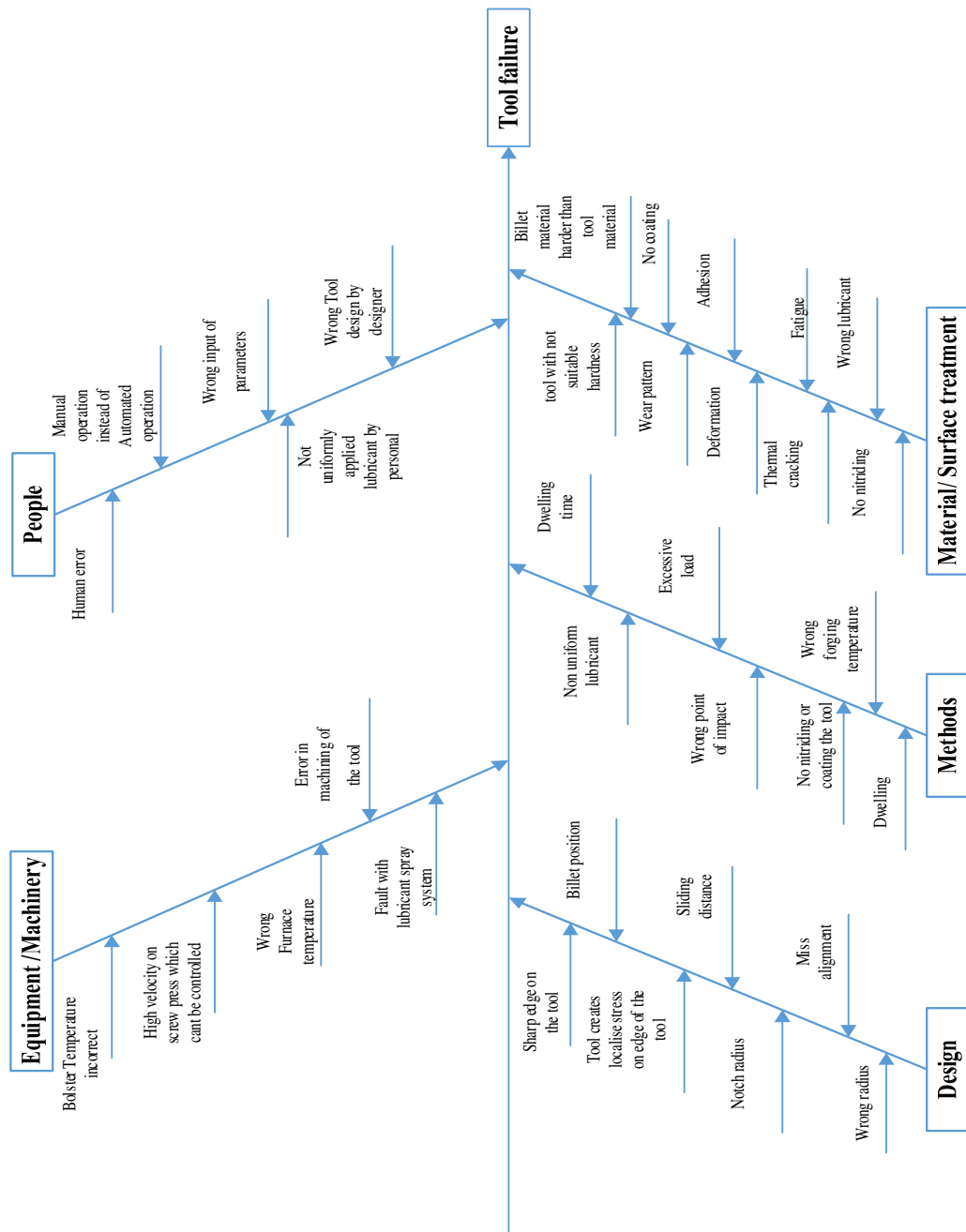


Figure 4-10: Fishbone analysis for H13 insert deformation

Series of Elastoplastic simulation were performing to observe the stress concentration as fillet radius increases. Simulation was performed for 2mm, 2.5mm and 3 mm fillet radius. However, as the aim of the project was to induce a measurable amount of wear (that can be measured by metrology equipment) after forging only 25 Inconel billets, 2mm fillet radius was chosen. The Figure 4-11 shows the induced wear after series of simulation using inserts of 1.5mm, 2mm, 2.5mm, and 3mm radius.

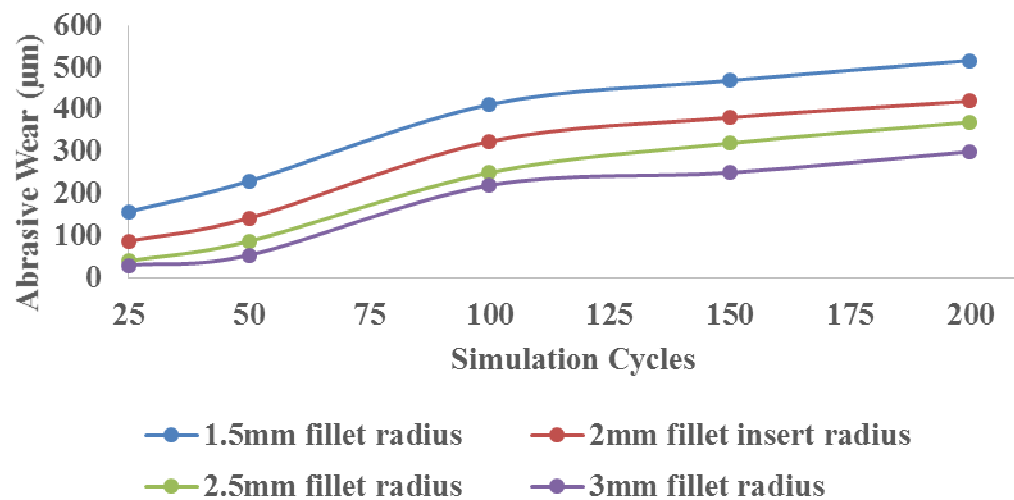


Figure 4-11: Comparison in wear induced using an insert with different radius

As 2mm radius could induce a measurable amount of wear (that can be measured by metrology equipment) after 25 cycles, therefore insert with 2mm radius were selected which has an effective stress below critical point of 1100 MPa at 350-400°C while produces a measurable amount of wear (that can be measured by metrology equipment) after forging 25 Inconel 718 billets as it shows in Figure 4-12 after running elastoplastic simulations for both 1.5 mm and 2 mm fillets Inserts.

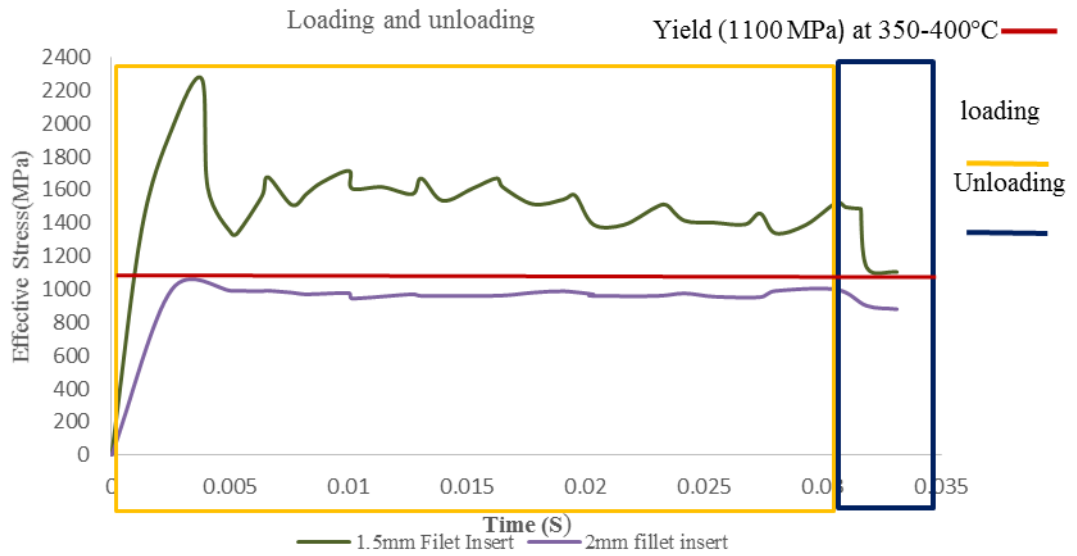


Figure 4-12: Effective stress comparison for both 1.5mm and 2mm fillet Inserts

Figure 4-13 shows changes of hardness in different zones for the insert with $R=1.5\text{mm}$ and there are three different zones while for the insert with $R=2\text{mm}$ there are not a clear boundary between the zones but more uniform microstructure.

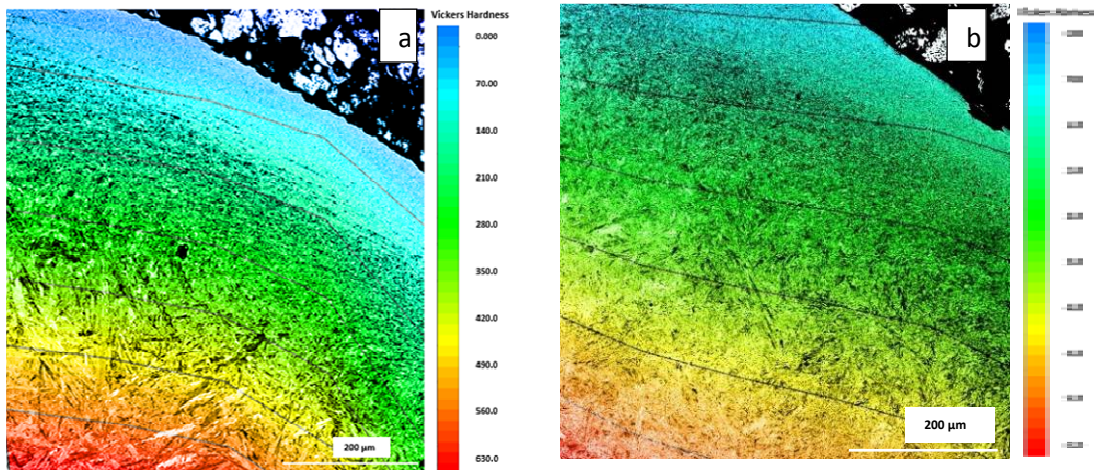


Figure 4-13: a) The colour map showing the change of microhardness in different zones for $R=1.5\text{ mm}$ insert and b) The colour map showing the change of microhardness in different zones for $R=2\text{ mm}$

4.1.5. Abrasive and Adhesive Wear Maps Analysis

For constructing wear maps, a series of simulations followed by practical trials were performed. As it mentioned in methodology removing dies after each blow wasn't practical. Therefore parts were measured instead of the tools assuming that they show the same wear pattern. The cmm wear measurement on the tools and the notch on the billets showed 90 % correlation. Each operation was 25 cycles. Therefore measured wear value on the notch of certain billets was compared with the simulation results. The wear value was taken from a similar position to increase the measurement accuracy.

The wear values predicted by the wear model and compared to the CMM measurement(Refer to Appendix B) showed 10- 20 % error between the wear values. These nine wear values were used to train the model(Comparison graphs are in Appendix A). This percentage was calculated comparing the wear results from simulation and CMM using equation $Error \% = ((ABS (Simulation - CMM) / ((Simulation + CMM) / 2))$ 4.1

$$Error \% = ((ABS (Simulation - CMM) / ((Simulation + CMM) / 2))$$

Then five simulations were run in addition to capturing the larger area for plotting wear maps as shown by alphabetic order of A-E on Table 4-3.

Table 4-3: Five additional abrasive wear were measured by running five additional simulations to fill the empty area of the scatter plot

Points	Billets Temperature (°C)	Energy on Screw Press (KJ)	Sliding Velocity (mm/s)	Contact pressure (MPa)	Simulation Abrasive Wear Depth (µm)
A	1125	12	170	690	110
B	1137	12.5	62	702	140
C	1137	12	64	480	152
D	1137	11.5	63	400	150
E	1125	11.5	170	402	149

Scatter plot was superimposed on the wear map as it shows in Figure 4-14.

The wear map shows mild, transition and severe regime at different sliding velocity and contact pressures. The wear map shows mild abrasive wear zone in very high sliding velocity and contact pressure which could be due to the creation of minor oxide layer which can act as a lubricant. While as sliding velocity reduces due to increase of oxide layer thickness and perhaps increase of thermal softening, mild abrasive zone moves to transition and severe zone. Change in wear regime also could be due to a change in wear mechanism. The wear usually has three different mechanisms, mechanical, oxide, and thermal wear. Mechanical wear happens when the contact pressure is only responsible for creating wear. While oxide wear happens when sliding velocity is mainly responsible for creating wear and mild to severe oxidation transition wear depends on the increase in temperature and contact time. Finally, contact pressure and sliding velocity are jointly responsible for creating thermal wear [112],[40].

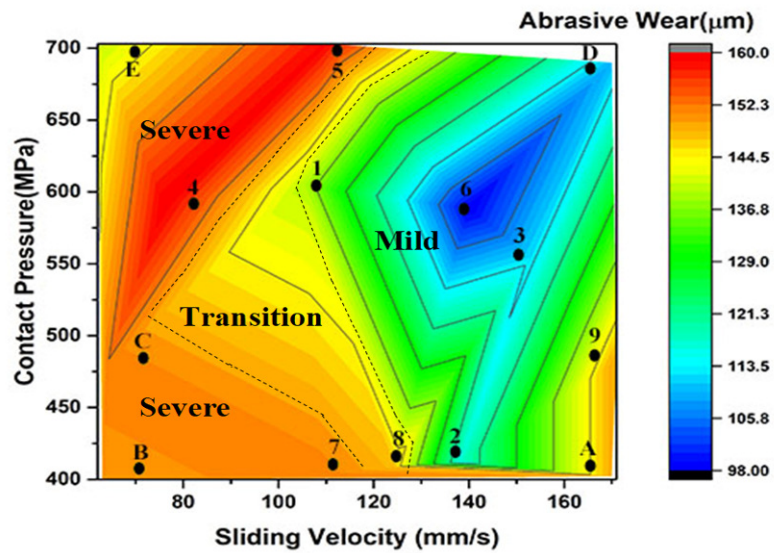


Figure 4-14: Abrasive wear for un-nitrided tool

Adhesive wear map in Figure 4-15 was constructed similar to

Figure 4-14, with the difference that three simulations were run in addition to nine simulations so wear map can cover a larger area. Nine abrasive wear values predicted by the wear model were compared to the CMM measurement which showed 16-23% error. The comparisons are at different energy in a screw press and different billet temperature. Wear map in Figure 4-14 shows that at a lower sliding velocity and lower load the contact between the two surface increase which increases the chance of thermal softening and severe wear.

Table 4-4: Nine adhesive wear values were predicted by the wear model which were compared to the CMM measurement. It showed 16- 23 % error. Then three additional simulations (A-C) was executed to increase the wear map coverage

Points	Billets Temperature (°C)	Energy on Screw Press (KJ)	Sliding Velocity (mm/s)	Contact pressure (MPa)	Simulation Adhesive Wear (µm)	Simulation and CMM Wear Measurement difference (%)
1	1050	8	90	624	115	16
2	1050	11.2	87	600	100	16
3	1050	16	155	625	95	19
4	1085	8	106	575	130	16
5	1085	11.2	112	523	93	22
6	1085	16	146	586	96	15
7	1120	8	116	364	143	22
8	1120	11.2	134	434	84	23
9	1120	16	288	742	89	20
A	1100	11.5	280	400	80	N/A
B	1080	11.8	200	560	85	N/A
C	1060	12	100	740	120	N/A

The scatter plot then was superimposed on the wear map. The map in Figure 4-15 shows mild, server and transition wear regimes.

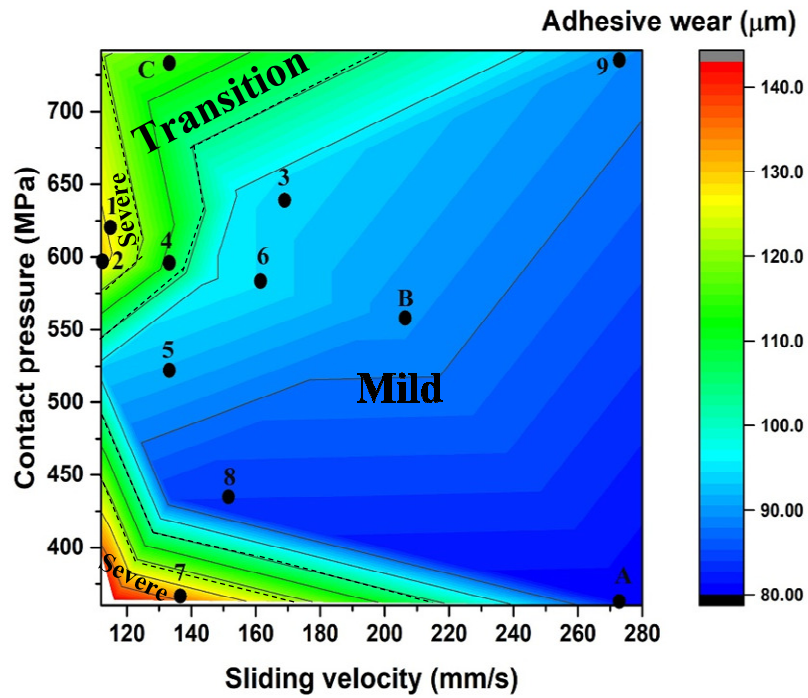


Figure 4-15: Adhesive wear for un-nitrided tool

The similar procedure for nitrided tools was implemented to construct an abrasive and adhesive wear map. The graphs for comparison between simulation prediction and practical measurement using Coordinate measurement machine (CMM) on nitrided tools are reported in appendix B. The wear map shows the large area of mild wear which indicates the existence of thin oxide layer. This follows by the transition wear that happens when oxide layers has build up, the asparity ditached form one surface will be attached to the other surface to bulup adhesive layer. This means adhesive wear moves from transition zone to a severe zone.

Table 4-5: Nine abrasive wear values measured by the wear model for the nitrided tool. It then was compared to the CMM measurement which indicates 16- 30 % difference between the measured wear values using these two methods.

Points	Billets Temperature(°C)	Energy on Screw Press (KJ)	Sliding Velocity (mm/s)	Contact pressure (MPa)	Simulation Abrasive Wear depth(μm)	Simulation and CMM Wear Measurement difference (%)
1	1085	16	180	560	54	18
2	1120	16	151	522	42	24
3	1050	11.2	123	629	64	25
4	1050	16	120	627	51	30
5	1085	11.2	115	597	53	19
6	1050	8	100	690	51	25
7	1085	8	102	583	79	27
8	1120	8	114	427	43	16
9	1120	11.2	80	528	46	21

Four additional abrasive wear were measured by running three additional simulations to fill the empty area of scatter plot. It is shown in Table 4-6.

Table 4-6: Abrasive wear values for four additional simulations

Points	Billet Temperature(°C)	Energy on screw press (KJ)	Sliding Velocity (mm/s)	Contact Pressure (MPa)	Abrasive Weardepth(μm) for nitrided tool
A	1066	12	178	690	50
B	1087	11.5	178	425	40
C	1066	12	80	690	43
D	1083	11.5	80	425	51

Scatter plot was superimposed on the wear map (Figure 4-16). The wear map shows mild, transition and severe regime at different sliding velocity and contact pressures.

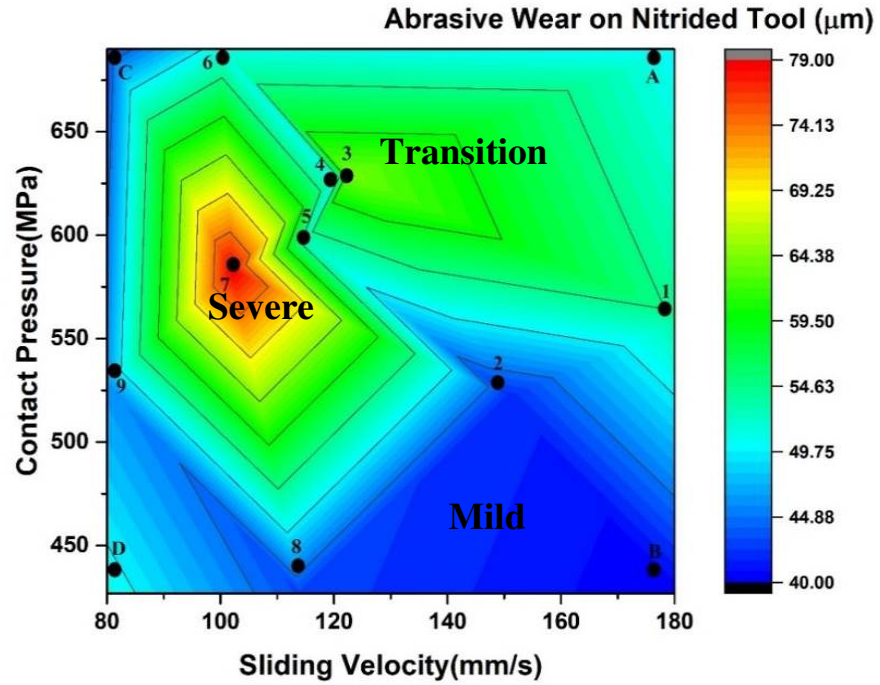


Figure 4-16: Abrasive wear on the nitrided tool

In Figure 4-16, shows the improvement in wear regimes in all the areas after nitriding compared to the un-nitrided tool. Mild wear is spread in different areas at different load and sliding velocity which could be because of the accumulation of a thin layer of oxide which acts as a lubricant.

Nine predicted adhesive wear values on nitrided tool were compared to CMM measurements. It indicated that 15-30 % error between the two which means 70-85 % agreement. Simulation data and comparison values are shown in Table 4-7.

Table 4-7: Nine adhesive wear values were predicted by the wear model for nitrided tool. It then was compared to the CMM measurement which showed 15- 34 % error.

Points	Billets Temperature(°C)	Energy on Screw Press (KJ)	Sliding Velocity (mm/s)	Contact pressure (MPa)	Simulation Adhesive Weardepth(µm)	Simulation and CMM Wear Measurement difference (%)
1	1085	16	180	553	20.65	24
2	1050	16	160	515	58.87	27
3	1085	11.2	118	613	37.27	30
4	1050	8	101	600	18.72	30
5	1120	11.2	122	553	30.7	15
6	1085	8	119	528	19.97	27
7	1050	11.2	138	480	23.91	22
8	1120	8	107	510	37.79	30
9	1120	16	80	570	37.22	30

In order to increase the captured area by plotted wear map four additional simulation (shown by A-D) were run at different billet temperatures and different energy on screw press. The Table 4-8 shows the data .

Table 4-8: Adhesive wear values for four additional simulations on the nitrided tools

Points	Billet Temperature(°C)	Energy on screw press (KJ)	Sliding Velocity (mm/s)	Contact Pressure (MPa)	Adhesive Weardepth(µm) for nitrided tool
A	1124	11.8	178	625	19
B	1124	11.6	178	480	36
C	1135	11.8	80	625	31
D	1135	11.6	80	480	37

Scatter plot was super imposed on the wear map as it shown on
4-17.

Figure

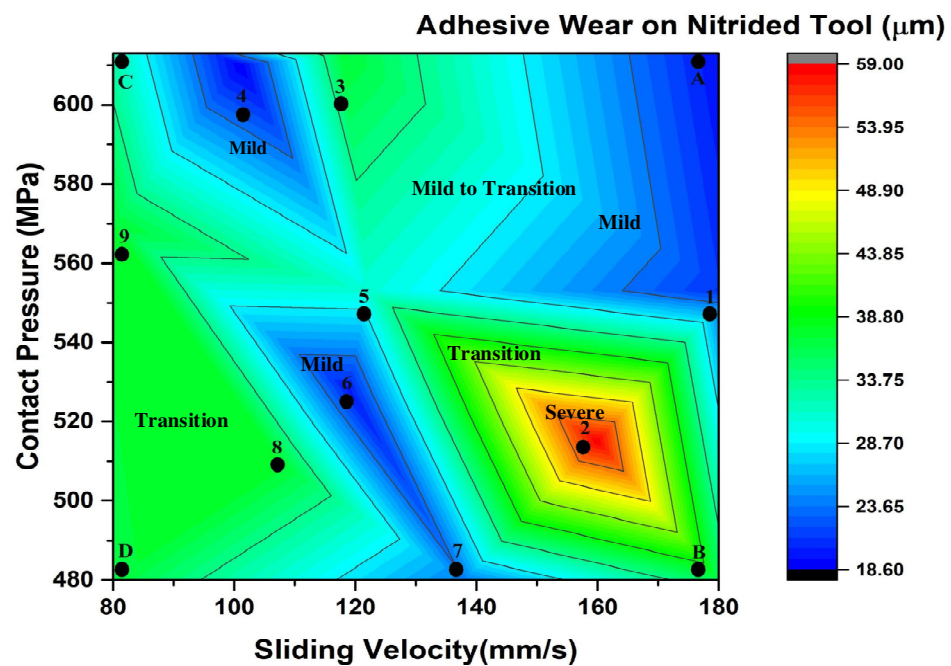


Figure 4-17: Adhesive wear on nitrided tool

Figure 4-17 shows 55-59 μm adhesive wear in severe wear regime at high sliding velocity and low to medium contact pressure where thermal and mechanical wear are both responsible for tool degradation. While only thermal wear has a bigger influence on creating adhesive wear in a nitrided tool. The amount of adhesive wear compared to 120-140 μm adhesive wear on un-nitrided tool in severe regime shows the improvement of tool surface after plasma nitriding.

Chapter 5 Discussion and Conclusion

The aims of this work were to:

1. Generating of series of wear maps using the computational model supported by physical trials
2. Establish a cost-effective benchmarking method to test different types of surface treatments

The preceding chapters have reported the work associated with a series of objectives designed to achieve these aims. Each of these activities has contributed to knowledge in the following specific areas of process and material science:

1. A computational process for the generation of wear model
2. Identification of H13 tool steel failure modes when forging Inconel 718
3. Experimental validation of the proposed wear model
4. Characterisation of H13 die material
5. Development of a repeatable measurement methodology for Wear
6. Generate Wear Maps for specific billet materials and die geometry
7. Limitations of the computationally generated wear maps

The following subsections briefly discuss the contributions and limitations associated with each of these.

5.1. A computational process for the generation of wear model

For generating wear map subroutines for abrasive and adhesive wear models (equation 2.4, 2.5) were embedded into the DEFORM 3D software. The parameters were inputted into the models including estimated wear coefficients. Different temperatures and loads provided estimated wear values for these sets of parameters. Then a series of practical trials were performed to calibrate the model. The new wear coefficients were embedded into the simulations to predict the outcome of the new forging operations. These wear values were used to plot a series of abrasive and adhesive wear maps.

5.2. Identification of H13 tool steel failure modes when forging Inconel 718

According to the literature abrasive and adhesive are considered as dominant failure modes in open die forging, however, other failure modes like plastic deformation might interact with these failures. The result of forging series of Inconel 718 billets on H13 tool steel showed that the H13 tool steel fails to perform well at high temperature and high energy of screw press. Nitriding of 0.1 mm case depth protects the surface against the abrasive and adhesive wear and avoiding the sharp corners in the design phase can prevent the die from deformation.

5.3. Experimental Validation of the proposed wear model

As discussed in the preceding chapters the proposed wear model was embedded in DEFORM FE simulation software to run a series of simulations based on the full factorial design of experiments. The predicted wear results then were compared with wear measurement results of the practical trials to validate the wear model. The comparison between the FE simulations and physical trials showed a good correlation of 80-90% for abrasive wear on un-nitrided tools and 70-84% on nitrided tools. While the correlation of 80-85% for adhesive wear on un-nitrided tools and 70-85% on nitrided tools was achieved.

5.4. Characterisation of H13 die material

As stated in the preceding chapters forging Inconel 718 on H13 insert with radius of 1.5 mm, deformed the H13 insert plastically which had to be investigated. For this purpose, SEM, EBSD and micro-hardness analysis were used. The SEM investigation confirmed the deformation of the insert and highlighted three different zones, deformed, recrystallised and martensitic, as well as transition zones between each zone within the microstructure. The EBSD results showed a large fraction of LAB which represents the deformation zone and is believed to be associated with different dislocation substructures caused by slip,

while the 28–32° angles correspond to special boundaries $\Sigma 39a$. The $\Sigma 39a$ boundaries were created during martensitic transformation. The HAB 58–60° corresponds to the twin boundaries. Comparison of the EBSD results before and after forging sample showed an increase of $\Sigma 13a$ and $\Sigma 39a$ boundaries and a decrease of $\Sigma 3$, $\Sigma 11$, $\Sigma 33$ and $\Sigma 41$ which is due to microstructure transformation caused by excessive load and high temperature and the fact that orientation angle is strain dependent. The range of measured microhardness on not deformed tool (before forging) was 523–610 HV, while measured microhardness on the deformed tool shows completely a different range 301–600 HV. The results of the microhardness measurements on the deformed tool confirm the evolution of the microstructure and formation of the different zones.

5.5. Development of a repeatable measurement methodology for wear

Establishing a repeatable failure measurements method using CMM was established measuring the change in die and workpiece (notch in the billet). As measuring the change in die after each forging cycle was proven impossible and measuring the changes in the workpiece (notch in the billet) was practical therefore workpiece (notch in the billet) was measured. The repeatability of $\pm 5\%$ was achieved using this method. The notch on the billets was scanned using 0.7 probe and points were recorded every 0.05 mm. By using this method changes throughout the forging operation was monitored.

5.6. Limitations of the computationally generate wear maps

The limitations of this method are listed below:

1. This process was not automated due to the failure of the robotic cell. Therefore, changing the parts and applying lubricant was done manually which introduced variability to the result.

2. Tool removal and measurement after each cycle was not possible. This limited access to more data on the changes in the tool during the forging operation.
3. The notch on the billets was scanned using 0.7 probe and points were recorded every 0.05 mm (the minimum distance possible). However, decreasing the measurement distance could have increased accuracy.

5.7. Conclusion

The aim of this work was to create a series of abrasive and adhesive wear maps for H13 tool steel, using FE simulations following forging trials. For physical trials, Inconel 718 billets were forged on H13 tool steel. It was confirmed by microstructure analysis that the forging tool had undergone plastic deformation. Therefore, based on the result of cause and effect analysis the tool design was considered the main cause of this failure, so tool design was changed. Series of trials were performed as per as design of experiments on the new dies. The comparison between the wear values which were predicted by FEM simulation and measured by the coordinate measurement machine showed an error of 10-20% for abrasive wear and 15-20% for adhesive wear. The good correlation between FE simulations and CMM results from forging trials show that the abrasive and adhesive wear models presented in this paper are applicable to hot forging processes.

The produced wear regime maps are supported by FE simulation along with the forging trials and have been shown to be representative of wear characteristic of H13 tool steel in a production environment. The produced wear maps illustrate that changes in the wear regime from mild wear to transition and severe wear are caused by small changes in velocity and contact pressure. The results show that at high sliding velocity more material is transferred from the billets to the inserts than vice versa. This suggested that the increase of adhesion wear, compared to abrasive wear, due to the formation of the oxide layer. At low sliding velocity change of wear regime from mild wear to transition and severe wear, the regime is obvious.

It occurred due to thermal softening and heat checking and builds up an oxide layer. The thin oxide layer which protected the tool by acting as a lubricant starts to break up and appear as wear particles. Lower adhesive wear in severe wear regime of nitrided tool compared to severe adhesive wear regime on the un-nitrided tool was observed. This is at high sliding velocity and low to medium contact pressure where oxide, thermal and mechanical wear are both responsible for tool degradation. While oxide, thermal wear has an influence on creating adhesive wear in the un-nitrided tool at low sliding velocity and contact pressure. The unusual spread of mild and transition wear regime could be due to the constant movement of material from one surface to another. This means that detached material from the billet which has been attached to the tool can move back to its origin. This proves that the nitrided layer protects the tools against adhesive wear. Abrasive wear map comparison shows the reduction in abrasive wear regimes in all the areas after nitriding compared to the un-nitrided tool. Mild wear is spread in different areas at different load and sliding velocity which could be because of the accumulation of a thin layer of oxide.

The produced wear maps have been used to optimise the forging process of Inconel 718 billets on H13 dies. The wear measurement method which has been introduced in this thesis is being established as a benchmarking method in Advanced Forming Research Centre. Furthermore, this methodology was used to compare the wear result of forging Inconel 718 billets on H13 tool steel covered by cobalt-based alloy (Stellite 21®)[77]. The result showed the promising result of adhesive and abrasive wear reduction after using this type of additive material and practicality of methodology which is being introduced in this thesis.

These wear maps can be used by industries to minimise tool wear. This methodology can be successfully applied to develop an understanding of the die life through comparison of different die materials, lubricants, and coatings.

5.8.Future work

The extended forging trials would help to better understand the H13 material behavior. FE model wear prediction has been compared with tool wear in open die forging so comparison with other forging processes will validate the model and proves the applicability.

- Further microstructure study using and using TCM, EDS analysis on the nitrided tool can give a better inside of nitriding.
- Using different angle on the sharp edge of the die could help create a database for designing
- Using a different set of parameters for the design of experiments
- Using the setup for trying different types of lubricants and coating
- Modify the simulation on DEFORM 3D to implement the effect of lubricants and coating
- Additional trials on additive layering

Chapter 6 References

- [1] B. -a. Behrens and F. Schaefer, “Prediction of wear in hot forging tools by means of finite-element-analysis,” *J. Mater. Process. Technol.*, vol. 167, no. 2–3, pp. 309–315, Aug. 2005.
- [2] S. Wilson and A. T. Alpas, “Wear mechanism maps for TiN-coated high speed steel,” *Surf. Coatings Technol.*, vol. 120–121, pp. 519–527, 1999.
- [3] S. C. Lim, “Recent developments in wear- mechanism maps,” vol. 31, no. 98, pp. 87–97, 1998.
- [4] J. Marashi, E. Yakushina, P. Xirouchakis, R. Zante, and J. Foster, “An evaluation of H13 tool steel deformation in hot forging conditions,” *J. Mater. Process. Technol.*, vol. 246, pp. 276–284, 2017.
- [5] T. Altan, G. Ngaile, and G. Shen, *Cold and Hot Forging: Fundamentals and Applications, Volume 1*. 2005.
- [6] T. Altan, B. Lillg, and Y. C. Yen, “Manufacturing of Dies and Molds,” 2000.
- [7] Z. Gronostajski and M. Hawryluk, “The main aspects of precision forging,” *Arch. Civ. Mech. Eng.*, vol. 8, no. 2, pp. 39–55, 2008.
- [8] O. Barrau, C. Boher, R. Gras, and F. Rezai-Aria, “Analysis of the friction and wear behaviour of hot work tool steel for forging,” *Wear*, vol. 255, no. 7–12, pp. 1444–1454, Aug. 2003.
- [9] C. A. V. L. I and T. U. Delft, “Advanced Techniques for Die and Mold Manufacturing,” vol. 42, no. 1, 2000.
- [10] ASM, “Failure Analysis and Prevention,” *Technology*, vol. 2, p. 3470, 2001.
- [11] S. R. R. I.A.Inman, “Temperature Versus sliding.pdf.” *Wear Journal*, 2006.

- [12] H. B. Bj, "Investigation of the compound layer and diffusion zone of pulsed plasma nitrided," 2013.
- [13] T. A. s. Kobayashi, "Metal forming and the finite element method," 1989. [Online]. Available: <http://www.slideshare.net/GonzaloSantiago/metal-forming-and-the-finite-element-method>. [Accessed: 23-Jul-2014].
- [14] M. Hawryluk, "Review of selected methods of increasing the life of forging tools in hot die forging processes," *Arch. Civ. Mech. Eng.*, vol. 16, no. 4, pp. 845–866, 2016.
- [15] M. Hawryluk and J. Jakubik, "Analysis of forging defects for selected industrial die forging processes," *Eng. Fail. Anal.*, vol. 59, pp. 396–409, 2016.
- [16] Manufacturing library, *Manufacturing Process*. 2001.
- [17] T. Altan, "Die and Mold Specifications," vol. 3336. 2001.
- [18] J. Marashi, J. Foster, and R. Zante, "Defining a Method of Evaluating Die Life Performance by Using Finite Element Models (FEM) and a Practical Open Die Hot Forging Method," *ESAFORM 2016 Proc.*, 2016.
- [19] E. by G. E. Dieter, H. A. Kuhn, S. L. Semiatin, and G. E. Dieter, *Handbook of Workability and Process Design (Google eBook)*. ASM International, 2003.
- [20] Srivastava S Indian Oil Corporation, "2nd international symposium on fuels and lubricants.," *Publ. Publ. Allied*, 2000.
- [21] ASM International Edited by Prasad .Y.V.R.K; Rao. K.P; Sasidhar.S, "ASM Forming and Forging," vol. 14, no. 9 Edition, pp. 80–90, 1993.
- [22] G. Yong and D. Han, "Review of Applications of Vanadium in Steels," pp. 1–11, 2010.
- [23] I. Mutlu, E. Oktay, and S. Ekinci, "Characterization of microstructure of H13 tool steel using ultrasonic measurements," *Russ. J. Nondestruct. Test.*,

vol. 49, no. 2, pp. 112–120, 2013.

- [24] X. H. CUI, J. SHAN, Z. R. YANG, M. X. WEI, S. Q. WANG, and C. DONG, “Alloying Design for High Wear-Resistant Cast Hot-Forging Die Steels,” *J. Iron Steel Res. Int.*, vol. 15, no. 4, pp. 67–72, 2008.
- [25] G. Byrne, “the Detection of Alpha Prime in,” vol. 100, no. 7025, pp. 1–10.
- [26] M. A. Saroosh, H. C. Lee, Y. T. Im, S. W. Choi, and D. L. Lee, “High cycle fatigue life prediction of cold forging tools based on workpiece material property,” *J. Mater. Process. Technol.*, vol. 191, no. 1–3, pp. 178–181, 2007.
- [27] P. F. . Bariani, G. . Berti, T. . Dal Negro, and S. Masiero, “Experimental evaluation and FE simulation of thermal conditions at tool surface during cooling and deformation phases in hot forging operations,” *Cirp Ann. Technol.*, vol. 51, no. 1, pp. 219–222, 2002.
- [28] C. Y. H. Lim, S. C. Lim, and K. S. Lee, “Wear of TiC-coated carbide tools in dry turning,” *Wear*, vol. 225, pp. 354–367, 1999.
- [29] K. Kato, “Micro-mechanisms of wear - wear modes,” *Wear*, vol. 153, no. 1, pp. 277–295, 1992.
- [30] M. O. Alam and A. S. M. A. Haseeb, “Response of Ti-6Al-4V and Ti-24Al-11Nb alloys to dry sliding wear against hardened steel,” *Tribol. Int.*, vol. 35, no. 6, pp. 357–362, 2002.
- [31] H. Kato, T. S. Eyre, and B. Ralph, “Wear mechanism map,” *Acta Metall. Mater.*, vol. 42, no. 5, pp. 1703–1713, May 1994.
- [32] H. C. Lee, B. M. Kim, and K. H. Kim, “Estimation of die service life in hot forging, considering lubricants and surface treatments,” *Proc. Inst. Mech. Eng. Part B J. Eng. Manuf.*, vol. 217, no. 7, pp. 1011–1022, 2003.
- [33] M. Z. Z. Gronostajski, M. Kaszuba *, M. Hawryluk, “Diagram of development of the various degradation.pdf.” .

- [34] J. A. Williams, "Wear and wear particles—some fundamentals," *Tribol. Int.*, vol. 38, no. 10, pp. 863–870, 2005.
- [35] Bhushan, *Introduction to Tribology*, 2 Edition. 2013.
- [36] M. Irani and A. K. Taheri, "Effect of forging temperature on homogeneity of microstructure and hardness of precision forged steel spur gear," *Mater. Chem. Phys.*, vol. 112, no. 3, pp. 1099–1105, 2008.
- [37] Z. Gronostajski, M. Kaszuba, S. Polak, M. Zwierzchowski, A. Niechajowicz, and M. Hawryluk, "The failure mechanisms of hot forging dies," *Mater. Sci. Eng. A*, vol. 657, pp. 147–160, 2016.
- [38] K. Arakawa, "Effects of wear on contact area and dynamic sliding velocity," *Wear*, vol. 328–329, pp. 552–555, 2015.
- [39] J. H. Beynon, "Tribology of hot metal forming," *Tribol. Int.*, vol. 31, no. 1–3, pp. 73–77, 1998.
- [40] J. A. (John A. Williams, *Engineering tribology*. Oxford University Press, 1994.
- [41] K. D. Tozetti, E. Albertin, and C. Scandian, "Abrasive size and load effects on the wear of a 19.9% chromium and 2.9% carbon cast iron," *Wear*, vol. 376–377, pp. 46–53, 2017.
- [42] K. Kato, "Koji Kato.pdf." *Tribology International Vol 30-No 5*, pp. 333–338, 1997.
- [43] K. Lange, L. Cser, M. Geiger, and J. A. G. Kals, "Tool Life and Tool Quality in Bulk Metal Forming," *CIRP Ann. - Manuf. Technol.*, vol. 41, no. 2, pp. 667–675, 1992.
- [44] M. Science, "The Relationship between Constant Friction Factor and Coefficient of Friction in Metal Forming Using Finite Element Analysis SH. Molaei, M. Shahbaz, R. Ebrahimi *," vol. 1, no. 2, pp. 14–22, 2014.
- [45] E. Felder and J. L. Montagu, "Friction and wear during the hot forging of

steels,” *Tribol. Int.*, vol. 13, no. 2, pp. 61–68, 1980.

- [46] C. Choi, A. Groseclose, and T. Altan, “Estimation of plastic deformation and abrasive wear in warm forging dies,” *J. Mater. Process. Technol.*, vol. 212, no. 8, pp. 1742–1752, 2012.
- [47] D. H. Kim, B. M. Kim, and C. G. Kang, “Die service life considering wear and plastic deformation in hot forging process,” *Key Eng. Mater.*, vol. 274–276, pp. 187–192, 2004.
- [48] J. Hodowany, G. Ravichandran, a Rosakis, and P. Rosakis, “Partition of plastic work into heat and stored energy in metals,” *Exp. Mech.*, vol. 40, no. 2, pp. 113–123, 2000.
- [49] M. J. Anderson, K. McGuire, R. C. Zante, W. J. Ion, A. Rosochowski, and J. W. Brooks, “Identifying the dominant failure mode in the hot extrusion tooling used to forge nickel based superalloy,” *J. Mater. Process. Technol.*, vol. 213, no. 1, pp. 111–119, 2013.
- [50] ASM Handbook Committee, *Volume 14-ASM Forming and Forging*. 1993.
- [51] J. H. Kang, I. W. Park, J. S. Jae, and S. S. Kang, “A study on die wear model of warm and hot forgings,” *Met. Mater.*, vol. 4, no. 3, pp. 477–483, 1998.
- [52] I. Sallit, C. Richard, G. Beranger, D. Kircher, and H. Michaud, “Experimental Study of Wear Behaviour of Hot Forging Tool Steels Under Dry Conditions: 40CrMoV13 Against C35E,” *Tribol. Lett.*, vol. 12, no. 3, pp. 147–154, 2002.
- [53] M. R. Soleymani Yazdi, G. Seyed Bagheri, and M. Tahmasebi, “Finite Volume Analysis and Neural Network Modeling of Wear During Hot Forging of a Steel Splined Hub,” *Arab. J. Sci. Eng.*, vol. 37, no. 3, pp. 821–829, Feb. 2012.
- [54] T. A. Colby Dahl, “Wear Map formula Tulsyan.pdf.” 2003.

- [55] DH.KIM, "Estimation of die service life against plastic deformation and wear during hot forging processes." 2005.
- [56] J. A. Williams, "Wear modelling: Analytical, computational and mapping: A continuum mechanics approach," *Wear*, vol. 225–229, no. I, pp. 1–17, 1999.
- [57] J. R. Hird and J. E. Field, "A wear mechanism map for the diamond polishing process," *Wear*, vol. 258, no. 1–4 SPEC. ISS., pp. 18–25, 2005.
- [58] T. H. C. Childs, "The sliding wear mechanisms of metals, mainly steels," *Tribol. Int.*, vol. 13, no. 6, pp. 285–293, 1980.
- [59] T. S. Eyre, "Wear Mechanisms," *Powder Metall.*, vol. 24, no. 2, pp. 57–63, Jan. 1981.
- [60] N. C. Welsh, "Frictional heating and its influence on the wear of steel," *J. Appl. Phys.*, vol. 28, no. 9, pp. 960–968, 1957.
- [61] R. Lewis and U. Olofsson, "Mapping rail wear regimes and transitions," *Wear*, vol. 257, no. 7–8, pp. 721–729, 2004.
- [62] S. Wilson and A. T. Alpas, "Effect of temperature and sliding velocity on TiN coating wear," *Surf. Coatings Technol.*, vol. 94–95, pp. 53–59, 1997.
- [63] H. So, D. S. Yu, and C. Y. Chuang, "Formation and wear mechanism of tribo-oxides and the regime of oxidational wear of steel," *Wear*, vol. 253, no. 9–10, pp. 1004–1015, 2002.
- [64] L. Cerroni and H. Kerl, "Primary cutaneous follicle center cell lymphoma," *Leuk. Lymphoma*, vol. 42, no. 5, pp. 891–900, 2001.
- [65] P. Marklund and R. Larsson, "Wet clutch friction characteristics obtained from simplified pin on disc test," *Tribol. Int.*, vol. 41, no. 9–10, pp. 824–830, 2008.
- [66] T. Materials, "The Materials Information Company," *Technology*, vol. 2, p. 3470, 2001.

- [67] K. Tkacz-Śmiech, B. Bożek, L. Sapa, and M. Danielewski, “Viscosity Controlled Interdiffusion in Nitriding,” *Diffus. Found.*, vol. 10, pp. 28–38, Jun. 2017.
- [68] T. H. E. N. Process, “An Introduction to Nitriding,” pp. 1–13, 2003.
- [69] J. Lesage, D. Chicot, O. Bartier, M. A. Zampronio, and P. E. V De Miranda, “Influence of hydrogen contamination on the tensile behavior of a plasma ion nitrided steel,” *Mater. Sci. Eng. A*, vol. 282, no. 1–2, pp. 203–212, 2000.
- [70] V. F. Terent’ev *et al.*, “The effect of nitriding on fatigue strength of structural alloys,” *Mechanika*, vol. 64, no. 2, pp. 12–22, 2007.
- [71] D. Kundalkar, M. Mavalankar, and A. Tewari, “Effect of gas nitriding on the thermal fatigue behavior of martensitic chromium hot-work tool steel,” *Mater. Sci. Eng. A*, vol. 651, pp. 391–398, 2016.
- [72] T. Materials, “The Materials Information Company,” *Technology*, vol. 2, p. 3470, 2001.
- [73] “Nanosized precipitates in H13 tool steel low temperature plasma nitriding Zagonel et al . Nanosized precipitates in H13 tool steel low temperature plasma nitriding,” 2012.
- [74] K. S. Jung, R. E. Schacherl, E. Bischoff, and E. J. Mittemeijer, “Normal and excess nitrogen uptake by iron-based Fe–Cr–Al alloys: the role of the Cr/Al atomic ratio,” *Philos. Mag.*, vol. 91, no. 18, pp. 2382–2403, Jun. 2011.
- [75] G. Castro, A. Fernández-Vicente, and J. Cid, “Influence of the nitriding time in the wear behaviour of an AISI H13 steel during a crankshaft forging process,” *Wear*, vol. 263, no. 7–12 SPEC. ISS., pp. 1375–1385, 2007.
- [76] M. Deshpande and A. Groseclose, “Selection of Die Materials and Surface Treatments for,” pp. 1–23, 1971.

- [77] J. Foster, C. Cullen, S. Fitzpatrick, G. Payne, L. Hall, and J. Marashi, “Remanufacture of hot forging tools and dies using laser metal deposition with powder and a hard-facing alloy Stellite 21 ®,” 2018.
- [78] S. C. Lim, “The relevance of wear-mechanism maps to mild-oxidational wear,” *Tribol. Int.*, vol. 35, no. 11, pp. 717–723, 2002.
- [79] J. Fluhrer, “User ’ s Manual Table of Contents,” no. 614.
- [80] J. Bonet and R. D. Wood, *Nonlinear continuum mechanics for finite element analysis*. Cambridge University Press, 1997.
- [81] BenedykJ.C, “Fe,” *High Perform. Alloy. Database*, 2008.
- [82] T. Euler-lagrange, “The Lagrangian Method,” *Introd. to Class. Mech. With Probl. Solut.*, 2008.
- [83] M. L. T. Cossio *et al.*, “Wear Properties of Plasma Nitrided Inconel 718 Superalloy,” *Uma ética para quantos?*, vol. XXXIII, no. 2, pp. 81–87, 2012.
- [84] C. Yang and S. Zhao, “Research on Combined Hot Extrusion Forming Process of Alternator Poles,” vol. 2013, no. October, pp. 16–22, 2013.
- [85] L. Instrument, “ARC IMAGER ARC IMAGER,” *L. Therm. camera Stand.*, 2017.
- [86] S. Liners, J. A. Components, and O. R. Equipment, “321 Stainless Steel,” *AK Steel Data sheet*, pp. 3–5, 2012.
- [87] M. Royer and W. Chester, “Determining Capabilities To Manufacture Inconel 718 Die Forgings,” no. June, pp. 29–31, 2009.
- [88] ASM International Edited by Y.V.R.K. Prasad; K.P. Rao; S. Sasidhar, “Hot Working Guide: A Compendium of Processing Maps, Second Edition - Google Books,” *ASM international*, 2003.
- [89] O. Barrau, C. Boher, C. Vergne, and R. Gras, “INVESTIGATIONS OF

FRICITION AND WEAR MECHANISMS OF HOT FORGING TOOL STEELS,” pp. 95–111, 2003.

- [90] I. Nikulin, R. Kaibyshev, and V. Skorobogatykh, “High temperature properties of an austenitic stainless steel,” *J. Phys. Conf. Ser.*, vol. 240, p. 012071, 2010.
- [91] GOM, “Optical 3D Scanner For small and medium-size components Industrial Optical 3D Scanning First launched in 1995 , the ATOS series of 3D scanners has been continually developed always utilizing state-of-the-art technology . Today , optical 3D measuring techn,” *ATOS Core*, 2015.
- [92] J. Marashi, J. Foster, and R. Zante, “Defining a method of evaluating die life performance by using finite element models (FEM) and a practical open die hot forging method,” 2016, vol. 1769, no. 1, p. 130001.
- [93] M. Range and C. Temperature, “<Inconel alloy 718.pdf>,” 2013.
- [94] B. -a. Behrens, “Finite element analysis of die wear in hot forging processes,” *CIRP Ann. - Manuf. Technol.*, vol. 57, no. 1, pp. 305–308, Jan. 2008.
- [95] R. G, K. G, and K. R, “Tool Steels: 5th Edition,” p. 227, 1998.
- [96] J. K. Dennis and E. A. A. G. Mahmoud, “Wear resistance of surface-treated hot forging dies,” *Tribol. Int.*, vol. 20, no. 1, pp. 10–17, 1987.
- [97] R. Douglas and D. Kuhlmann, “Guidelines for precision hot forging with applications,” *J. Mater. Process. Technol.*, vol. 98, no. 2, pp. 182–188, Jan. 2000.
- [98] C. Miland and W. Panasiuk, “Increasing the life of forging tools: New materials, technologies and methods of investigation,” *J. Mech. Work. Technol.*, vol. 6, no. 2–3, pp. 183–191, 1982.

- [99] L. Qian, X. Feng, and F. Zhang, “Deformed Microstructure and Hardness of Hadfield High Manganese Steel,” *Mater. Trans.*, vol. 52, no. 8, pp. 1623–1628, 2011.
- [100] A. Medvedeva, J. Bergström, S. Gunnarsson, and J. Andersson, “High-temperature properties and microstructural stability of hot-work tool steels,” *Mater. Sci. Eng. A*, vol. 523, no. 1–2, pp. 39–46, 2009.
- [101] J. Bonet and R. D. Wood, “Nonlinear Continuum Mechanics for Finite Element Analysis,” *Commun. Numer. Methods Eng.*, vol. 24, no. 11, pp. 1567–1568, 1997.
- [102] Voort and Manilova, “metalurgic_tool steel.pdf.” Polzunov Central Boiler and Turbine Institute, St. Petersburg, Russia, 2000.
- [103] J. Cai, T. A. Dean, and Z. M. Hu, “Alternative die designs in net-shape forging of gears,” *J. Mater. Process. Technol.*, vol. 150, no. 1–2, pp. 48–55, 2004.
- [104] R. Siegel, “Emisivity,” *Therm. Radiat. Heat Transf. Fourth Ed.*, vol. 212, no. 100, p. 41, 2002.
- [105] S. Abachi, M. Akkök, and M. İlhan Gökler, “Wear analysis of hot forging dies,” *Tribol. Int.*, vol. 43, no. 1–2, pp. 467–473, Jan. 2010.
- [106] H. J. Mcqueen, “Static Recrystallization of Tool Steels 1 1,” pp. 4458–4463, 2007.
- [107] S. H. Zahiri and P. D. Hodgson, “The static , dynamic and metadynamic recrystallisation of a medium carbon steel,” *Mater. Sci. Technol.*, vol. 20, p. 458, 2004.

- [108] T. Sakai, A. Belyakov, R. Kaibyshev, H. Miura, and J. J. Jonas, “Dynamic and post-dynamic recrystallization under hot, cold and severe plastic deformation conditions,” *Prog. Mater. Sci.*, vol. 60, no. 1, pp. 130–207, 2014.
- [109] H. R. Piehler, “Crystal-Plasticity Fundamentals,” vol. 22, no. Ref 2, p. 6, 2009.
- [110] H. e. HU, L. YANG, L. ZHEN, W. zhu SHAO, and B. you ZHANG, “Relationship between boundary misorientation angle and true strain during high temperature deformation of 7050 aluminum alloy,” *Trans. Nonferrous Met. Soc. China (English Ed.)*, vol. 18, no. 4, pp. 795–798, 2008.
- [111] JOOST J. VLASSAK and W. D. NIX, “Measuring the Elastic Properties of Anisotropic Materials by Means of Indentation Experiments,” *J. Mech. Phys. Solids*, Vol. 42, no. September, 2016.
- [112] Y. Shi and X. Wu, “Research on Oxidation Wear Behavior of a New Hot Forging Die Steel,” *J. Mater. Eng. Perform.*, vol. 27, no. 1, pp. 176–185, 2018.


```

C  OUTPUT :
c    WI=WEAR(4,N) ! wear rate at the end of current step
c    WA=WEAR(5,N) ! accumulated wear depth upto the end of current step
C
    IMPLICIT DOUBLE PRECISION (A-H,O-Z), INTEGER (I-N)
C
C
    NWR=IABS(IWMD)
    GO TO (501,502,503,504,505,506,507,508,509,510),NWR
C
    501 CALL
    UWEAR1(VMC1,VMC2,VMC3,VMC4,VMC5,VMC6,DTMAXC,WI,WA)
    RETURN
    502 CALL
    UWEAR2(VMC1,VMC2,VMC3,VMC4,VMC5,VMC6,DTMAXC,WI,WA)
    RETURN
    503 CALL
    UWEAR3(VMC1,VMC2,VMC3,VMC4,VMC5,VMC6,DTMAXC,WI,WA)
    RETURN
    504 CALL
    UWEAR4(VMC1,VMC2,VMC3,VMC4,VMC5,VMC6,DTMAXC,WI,WA)
    RETURN
    505 CALL
    UWEAR5(VMC1,VMC2,VMC3,VMC4,VMC5,VMC6,DTMAXC,WI,WA)
    RETURN
    506 CALL
    UWEAR6(VMC1,VMC2,VMC3,VMC4,VMC5,VMC6,DTMAXC,WI,WA)
    RETURN

```



```

c   VMC2      ! w/p temperature
c   VMC3      ! sliding velocity
c   VMC4      ! pressure
c   VMC5      ! shear stress
c   VMC6      ! nodal area
c   DTMAXC    ! time step
c   WI=WEAR(4,N) ! wear rate at the previous step
c   WA=WEAR(5,N) ! accumulated wear depth upto the previous step
C   OUTPUT :
c   WI=WEAR(4,N) ! wear rate at the end of current step
c   WA=WEAR(5,N) ! accumulated wear depth upto the end of current step
C
      IMPLICIT DOUBLE PRECISION (A-H,O-Z), INTEGER (I-N)
C
C
      NWR=IABS(IWMD)
      GO TO (501,502,503,504,505,506,507,508,509,510),NWR
C
      501 CALL
      UWEAR1(VMC1,VMC2,VMC3,VMC4,VMC5,VMC6,DTMAXC,WI,WA)
      RETURN
      502 CALL
      UWEAR2(VMC1,VMC2,VMC3,VMC4,VMC5,VMC6,DTMAXC,WI,WA)
      RETURN
      503 CALL
      UWEAR3(VMC1,VMC2,VMC3,VMC4,VMC5,VMC6,DTMAXC,WI,WA)
      RETURN

```



```
c    WI=WEAR(4,N) ! wear rate at the end of current step
c    WA=WEAR(5,N) ! accumulated wear depth upto the end of current step
C
```

```
RETURN
```

```
END
```

7.2. Appendix B

7.2.1. Abrasive and adhesive wear comparison between simulation prediction results and practical measurements using Coordinate measurement machine (on tools without nitriding layer).

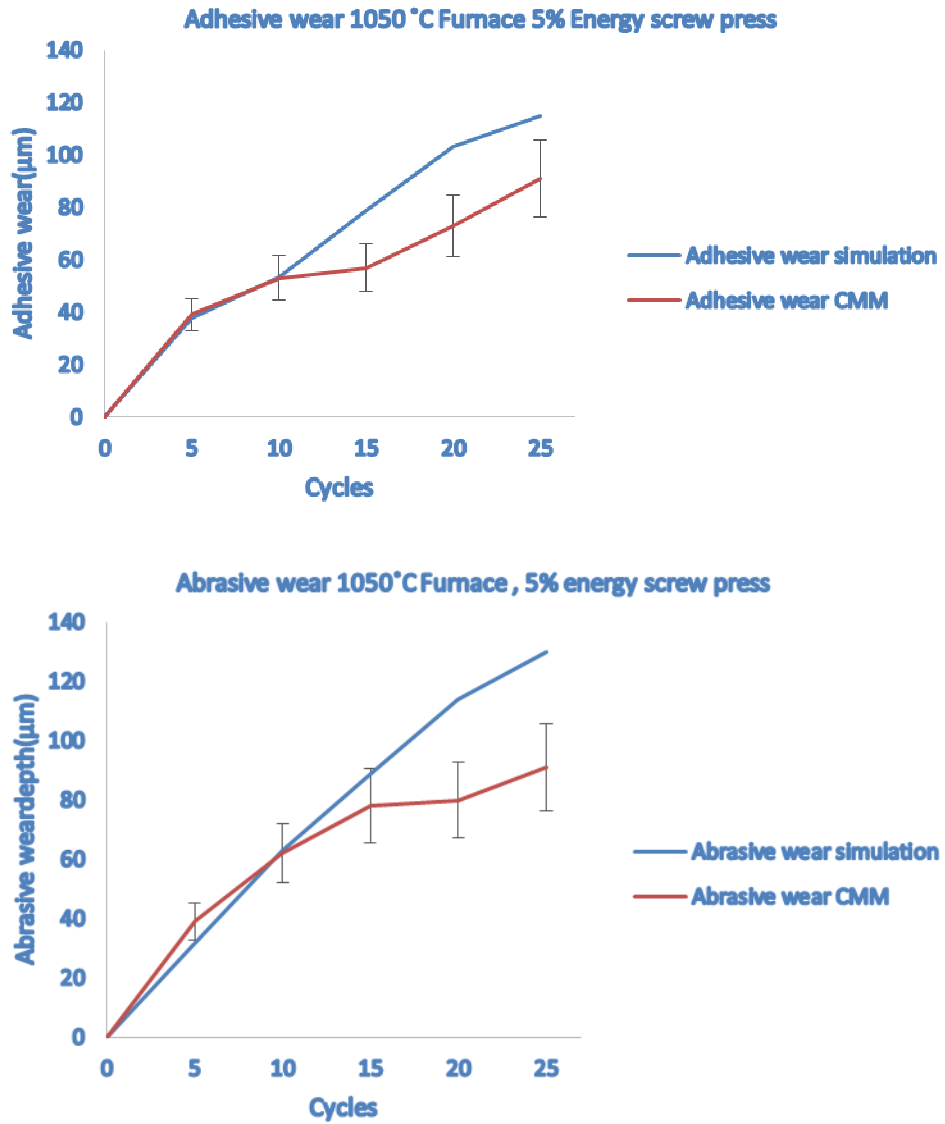


Figure 7-1 CMM measurement and simulation prediction comparison at 1050 °C furnace temperature and 5% of energy on screw press(8KJ) for abrasive and adhesive wear (Un-nitrided tool)

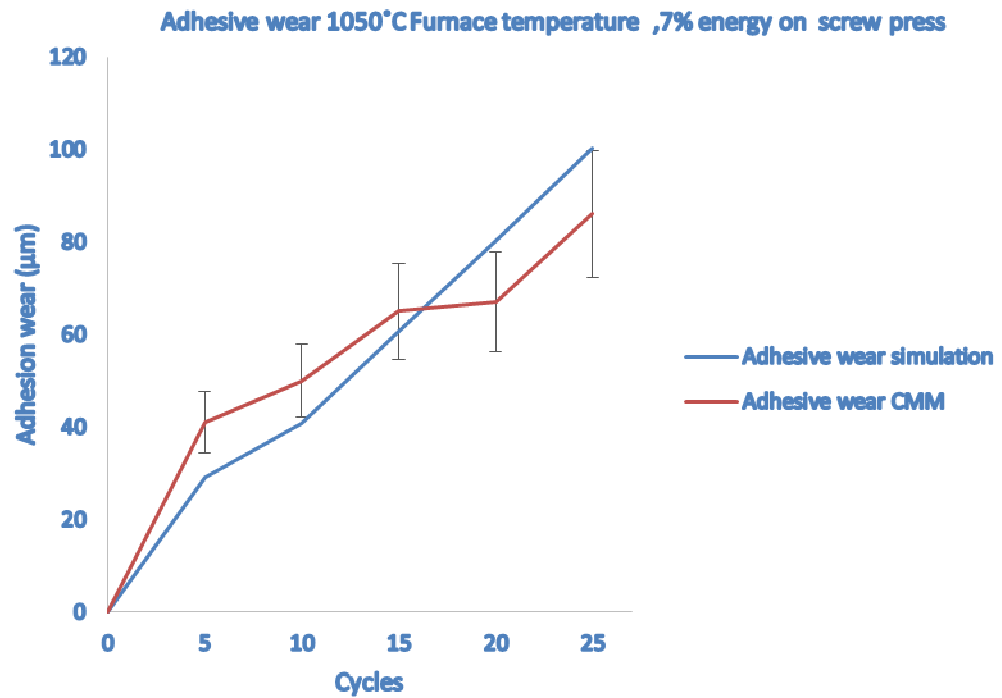
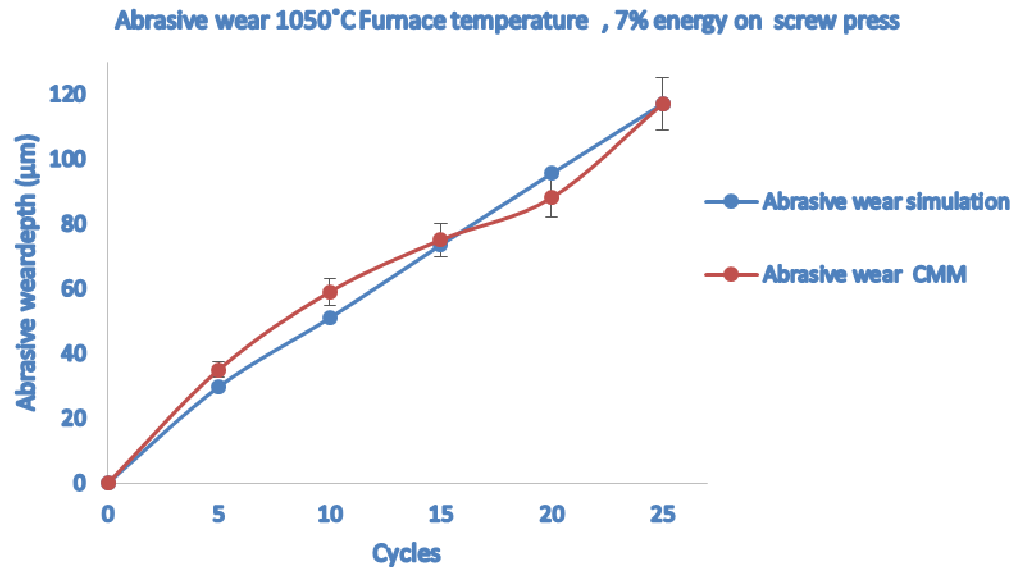


Figure 7-2. CMM measurement and simulation prediction comparison at 1050 °C furnace temperature and 7% of energy on screw press(11.2 KJ) for abrasive and adhesive wear (Un-nitrided tool)

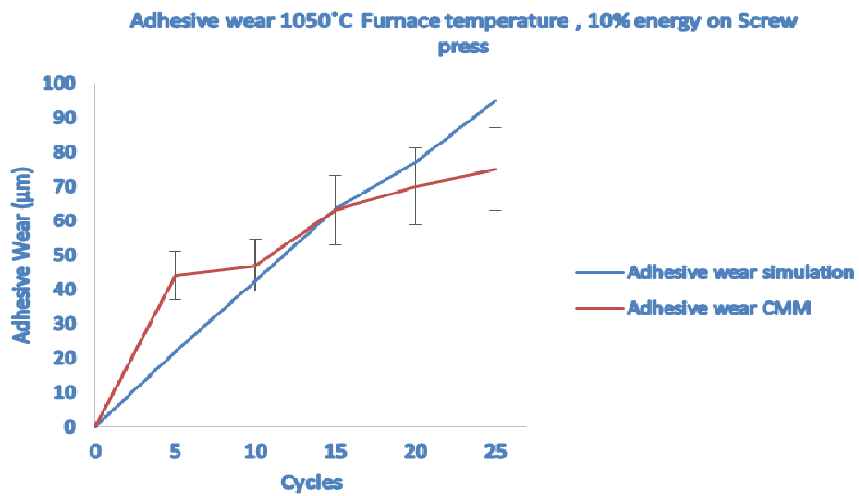
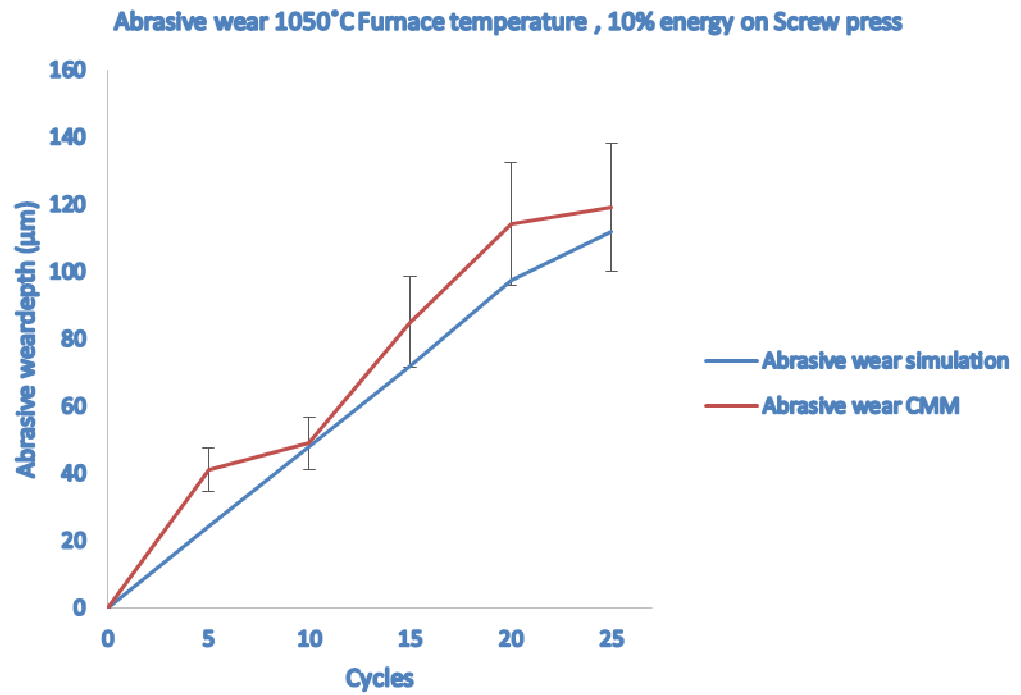


Figure 7-3. CMM measurement and simulation prediction comparison at 1050 °C furnace temperature and 10% of energy on screw press(16KJ) for abrasive and adhesive wear (Un-nitrided tool)

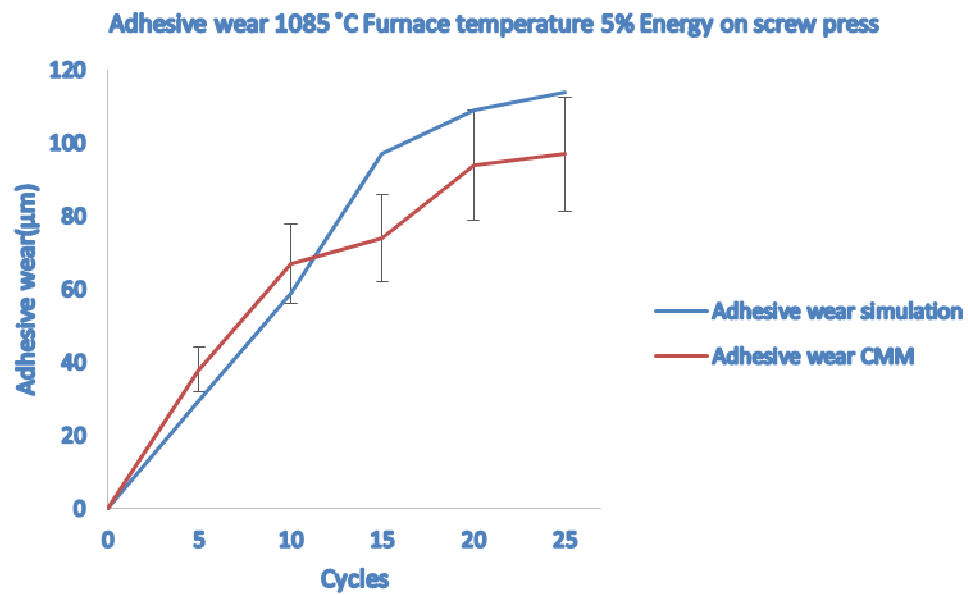
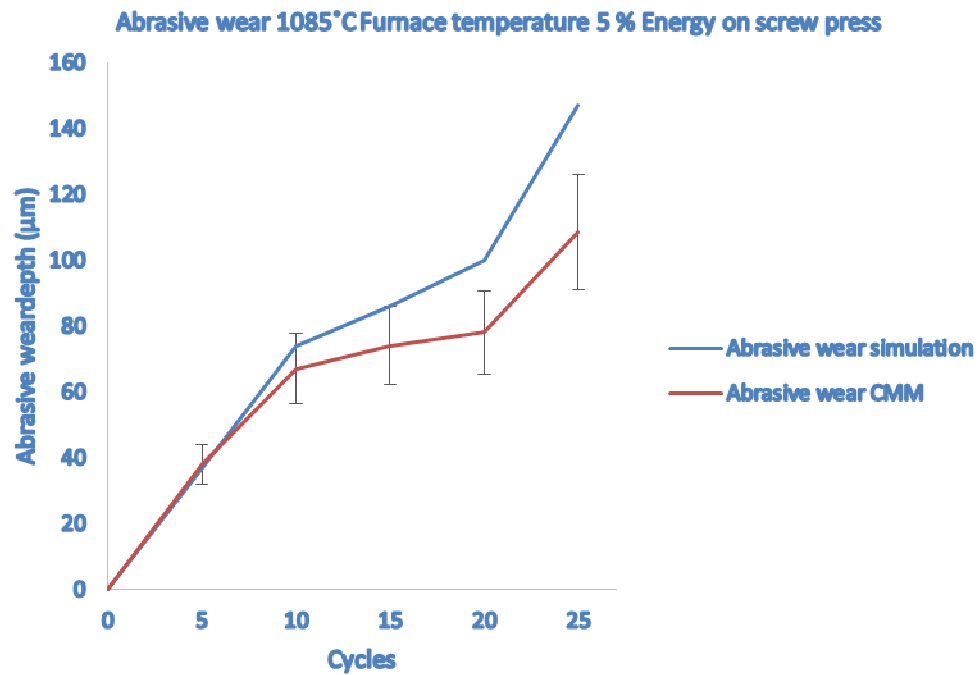


Figure 7-4. CMM measurement and simulation prediction comparison at 1085 °C furnace temperature and 5% of energy on screw press (8KJ)for abrasive and adhesive wear (Un-nitrided tool)

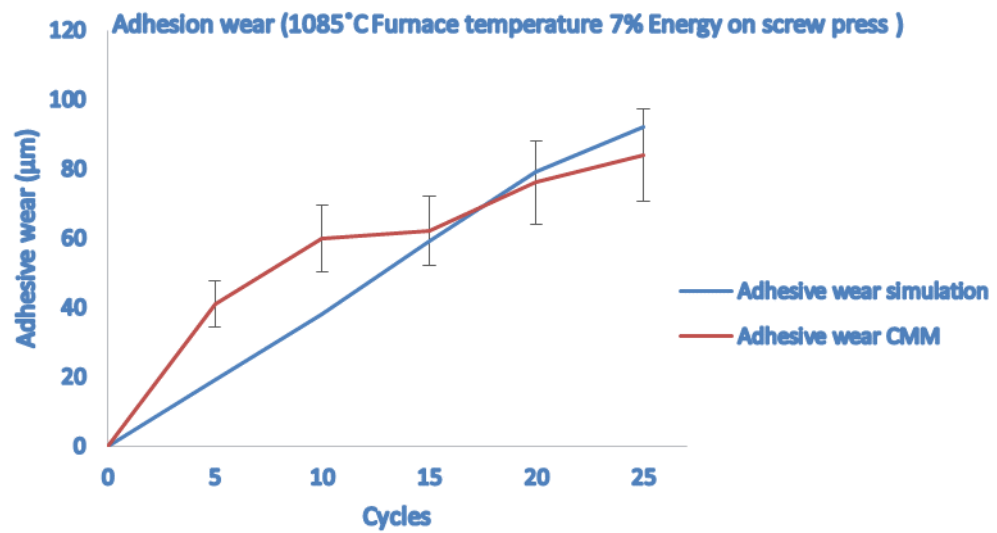
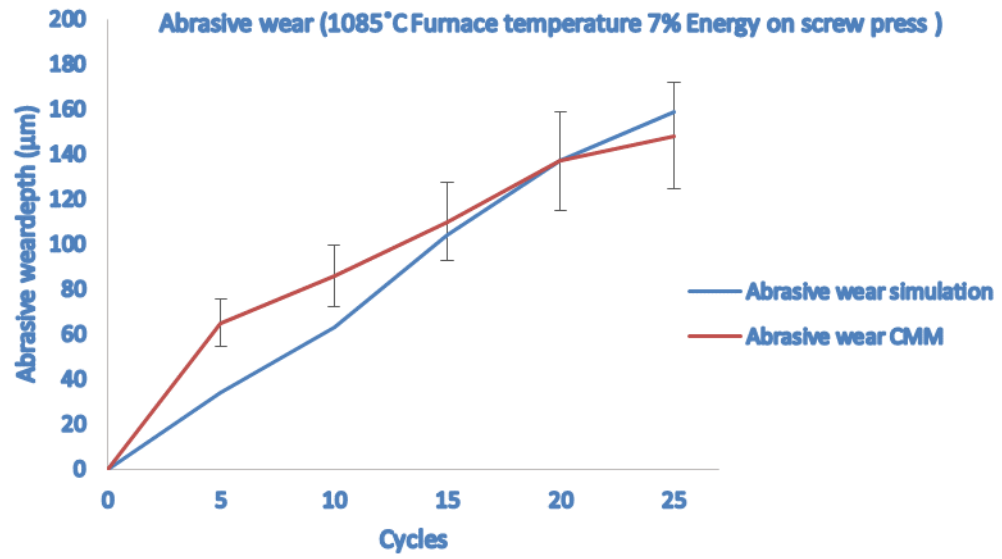


Figure 7-5. CMM measurement and simulation prediction comparison at 1085 °C furnace temperature and 7%(11.2KJ) of energy on screw press for abrasive and adhesive wear (Un-nitrided tool)

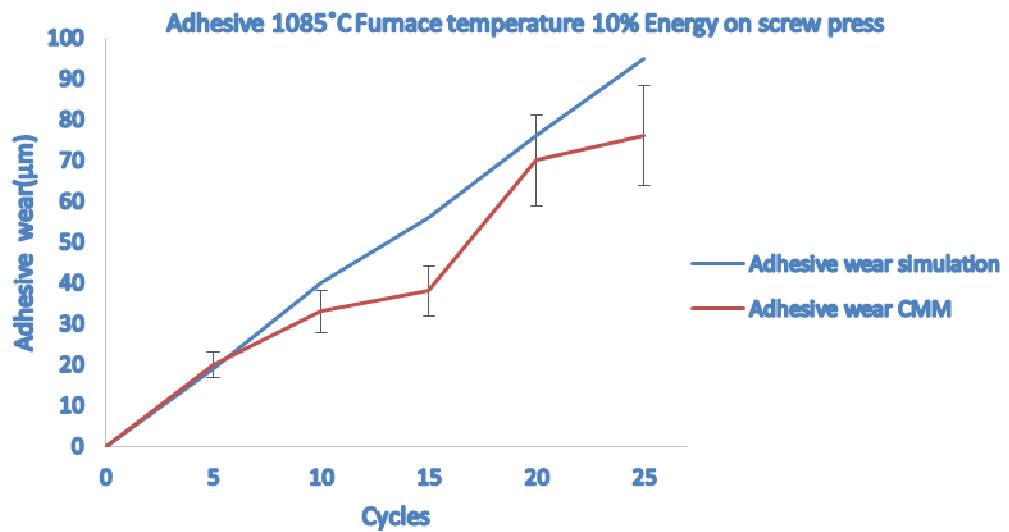
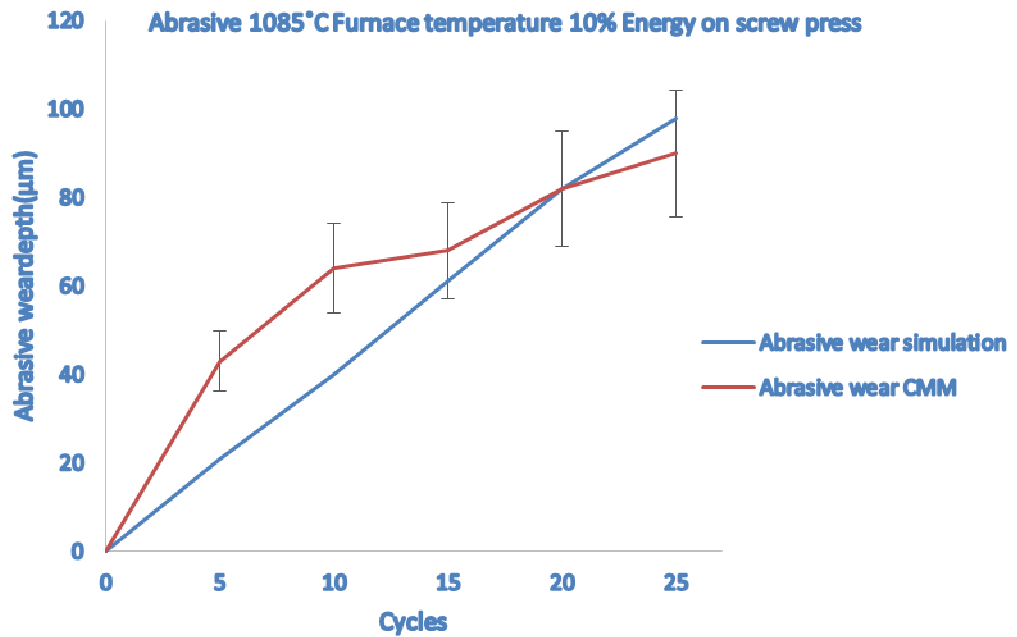


Figure 7-6. CMM measurement and simulation prediction comparison at 1085 °C furnace temperature and 10 % of energy on screw press(16KJ) for abrasive and adhesive wear (Un-nitrided tool)

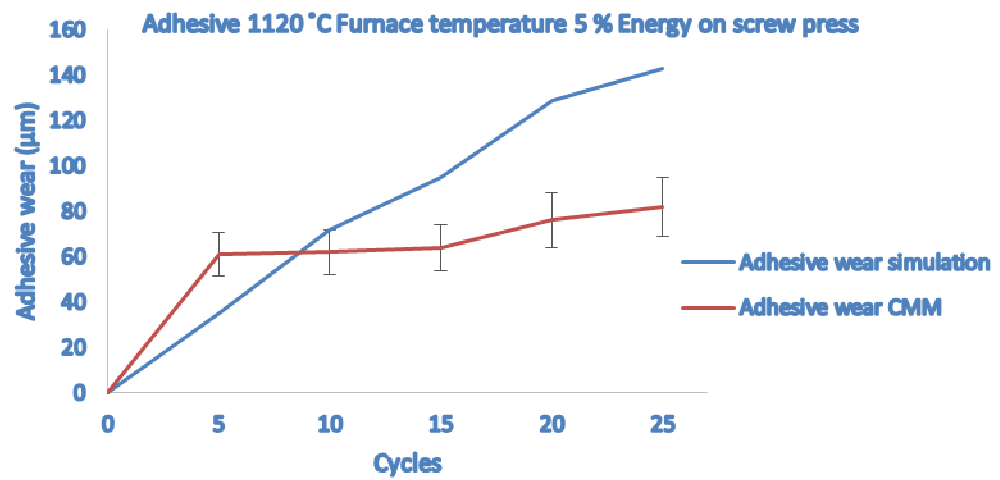
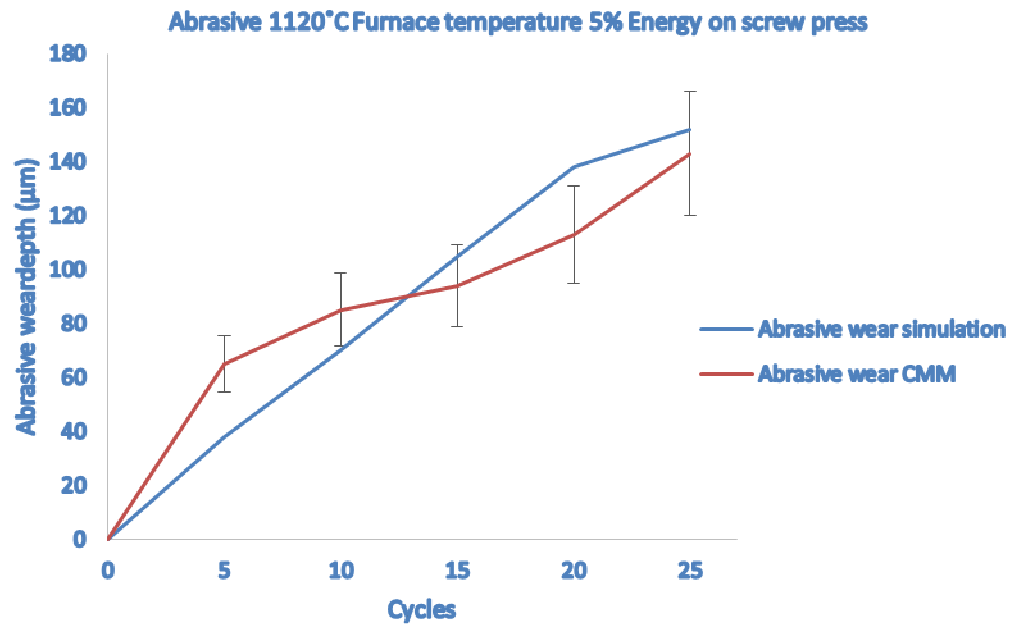


Figure 7-7. CMM measurement and simulation prediction comparison at 1120°C furnace temperature and 5 % of energy on screw press (8KJ)for abrasive and adhesive wear (Un-nitrided tool)

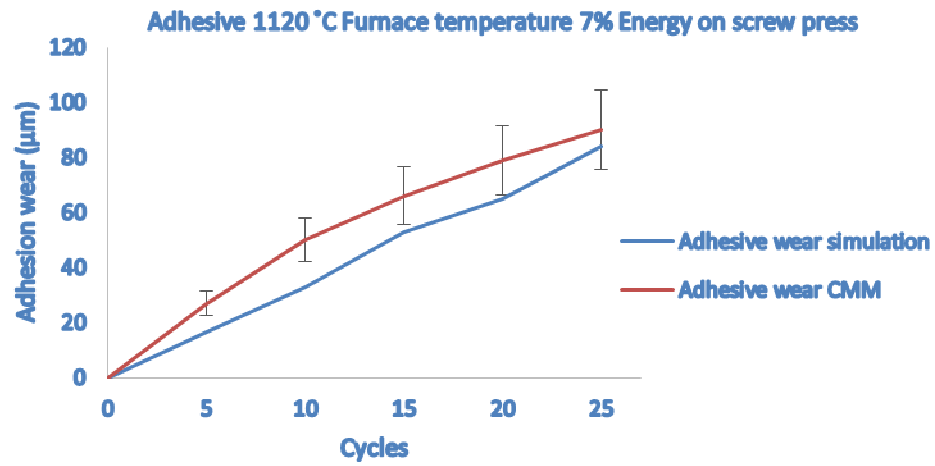
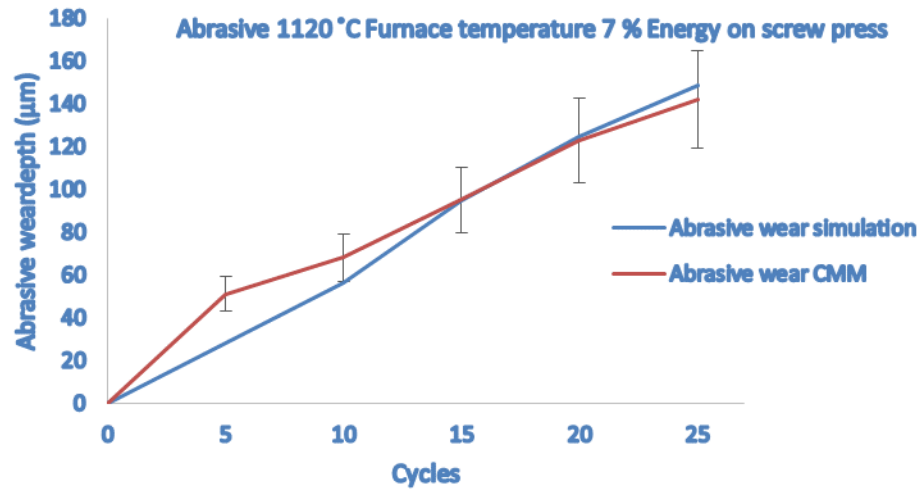


Figure 7-8. CMM measurement and simulation prediction comparison at 1120°C furnace temperature and 7 % of energy on screw press(11.2KJ) for abrasive and adhesive wear (Un-nitrided tool)

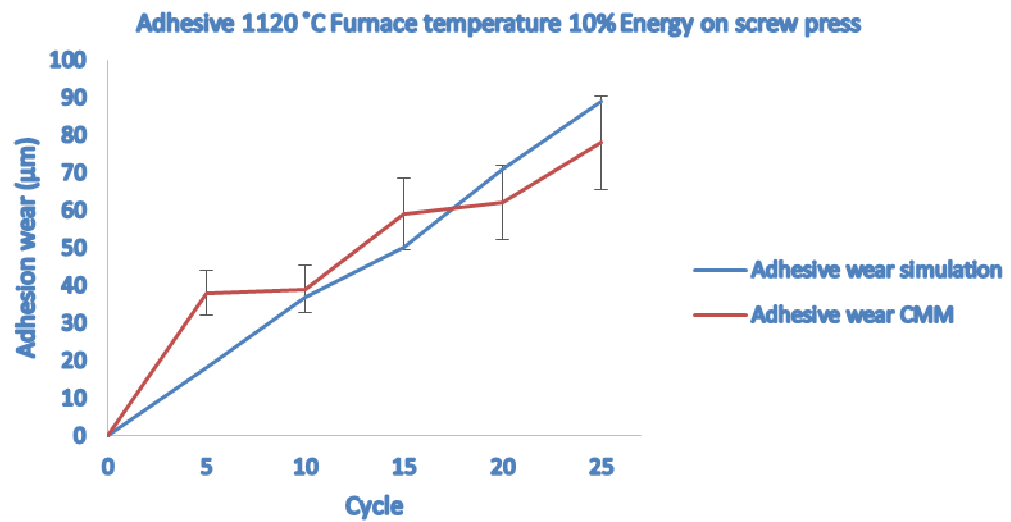
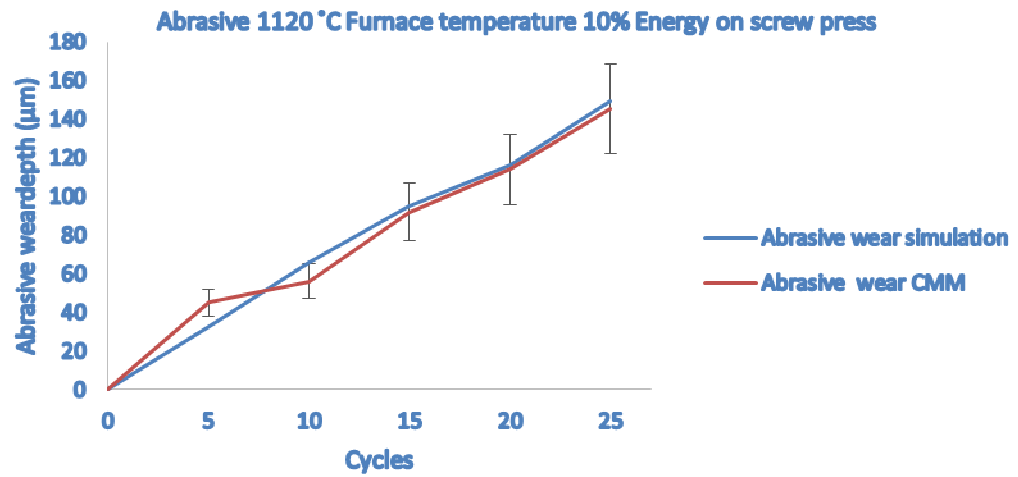


Figure 7-9. CMM measurement and simulation prediction comparison at 1120°C furnace temperature and 10 % of energy on screw press (16KJ)for abrasive and adhesive wear (Un-nitrided tool)

7.2.2. Abrasive and adhesive wear comparison between simulation prediction results and practical measurements using Coordinate measurement machine (on nitrided tools).

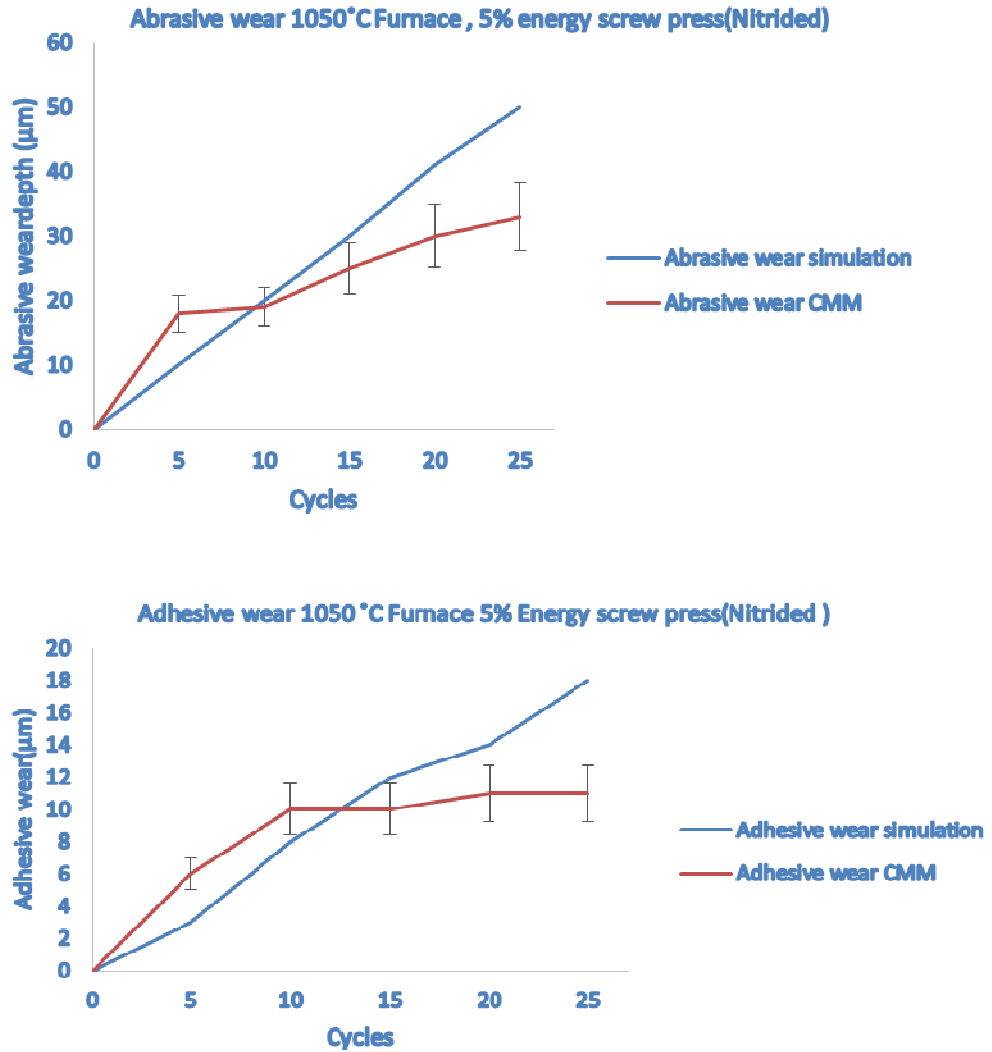


Figure 7-10. CMM measurement and simulation prediction comparison at 1050°C furnace temperature and 5 % of energy on screw press (8 KJ) for abrasive and adhesive wear (Nitrided tool)

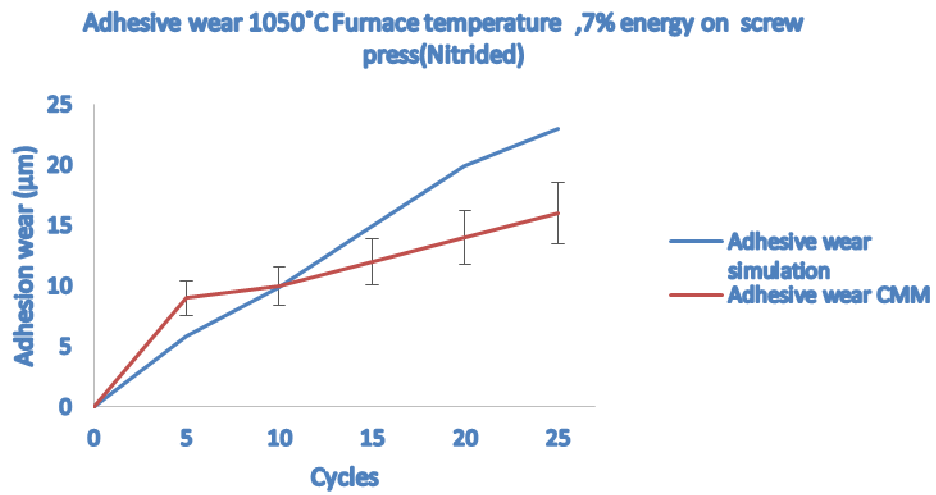
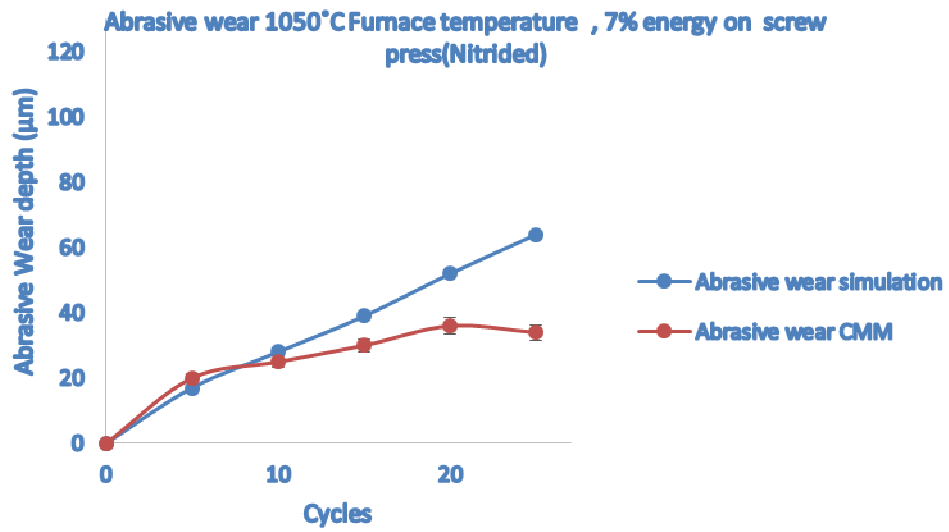


Figure 7-11.CMM measurement and simulation prediction comparison at 1050°C furnace temperature and 7 % of energy on screw press (11.2 KJ) for abrasive and adhesive wear (Nitrided tool)

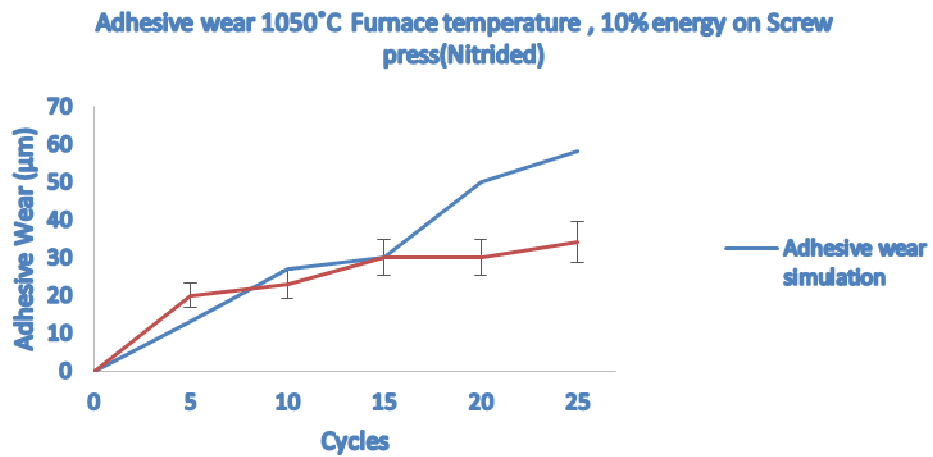
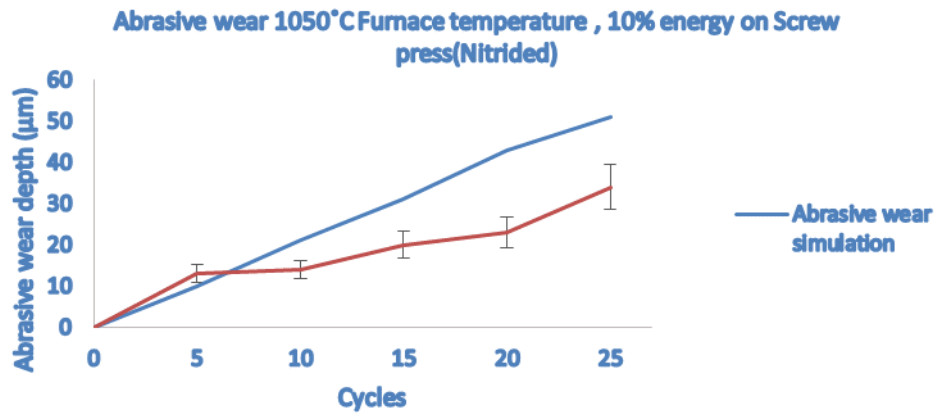


Figure 7-12. CMM measurement and simulation prediction comparison at 1050°C furnace temperature and 10 % of energy on screw press (16 KJ) for abrasive and adhesive wear (Nitrided tool)

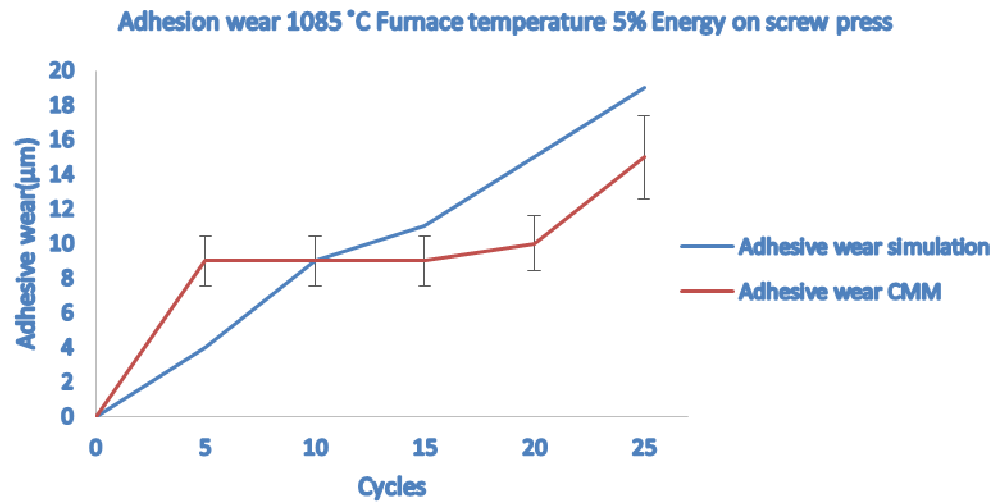
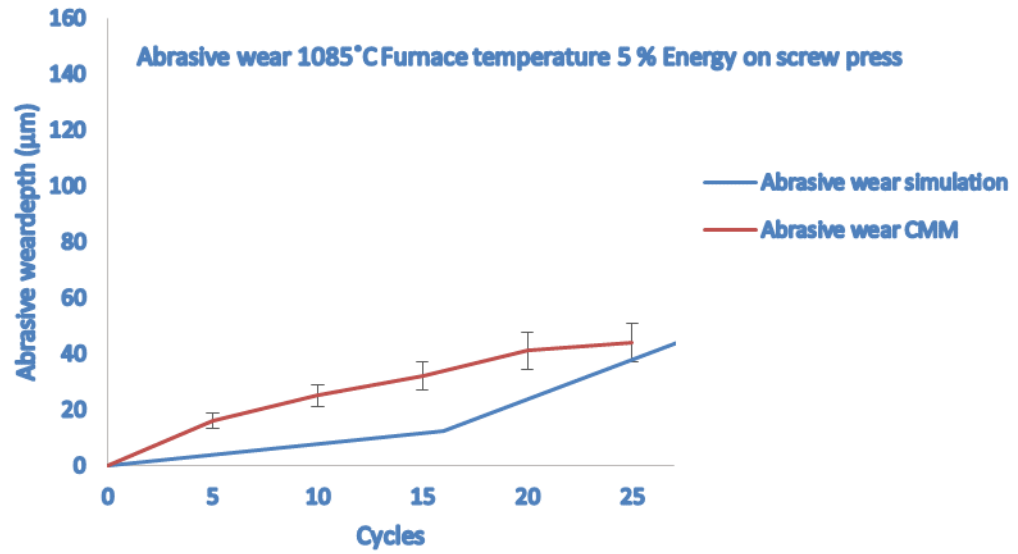


Figure 7-13. CMM measurement and simulation prediction comparison at 1085°C furnace temperature and 5 % of energy on screw press (8 KJ) for abrasive and adhesive wear (Nitrided tool)

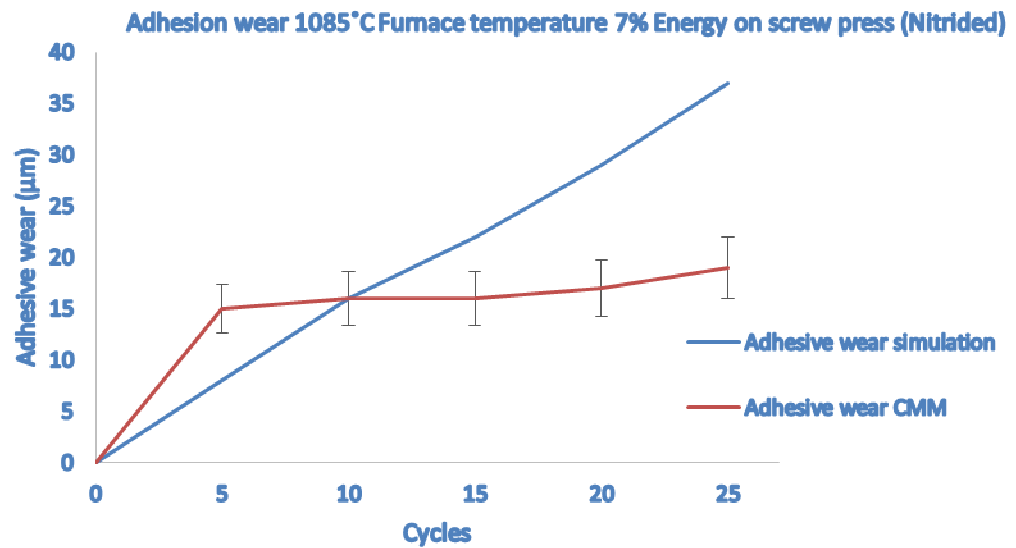
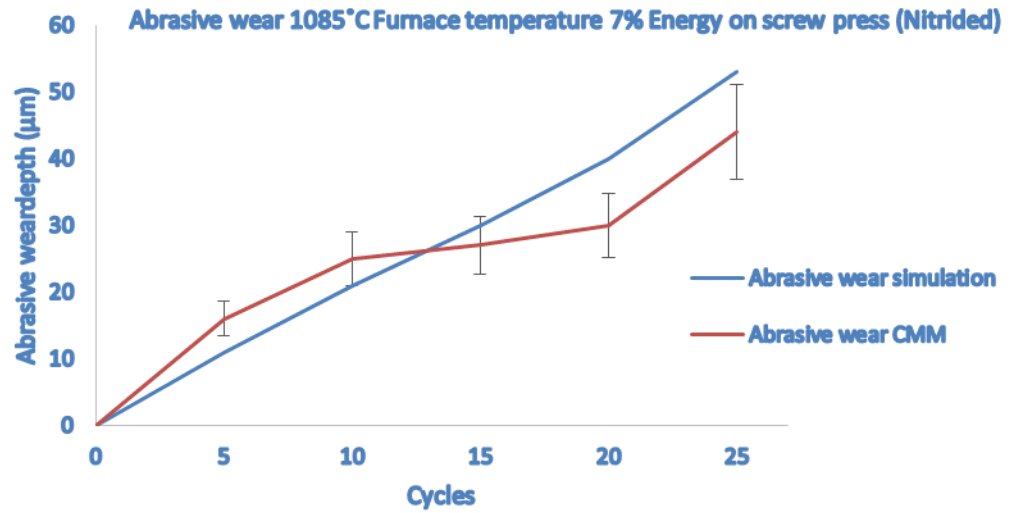


Figure 7-14. CMM measurement and simulation prediction comparison at 1085°C furnace temperature and 7 % of energy on screw press (11.2 KJ) for abrasive and adhesive wear (Nitrided tool)

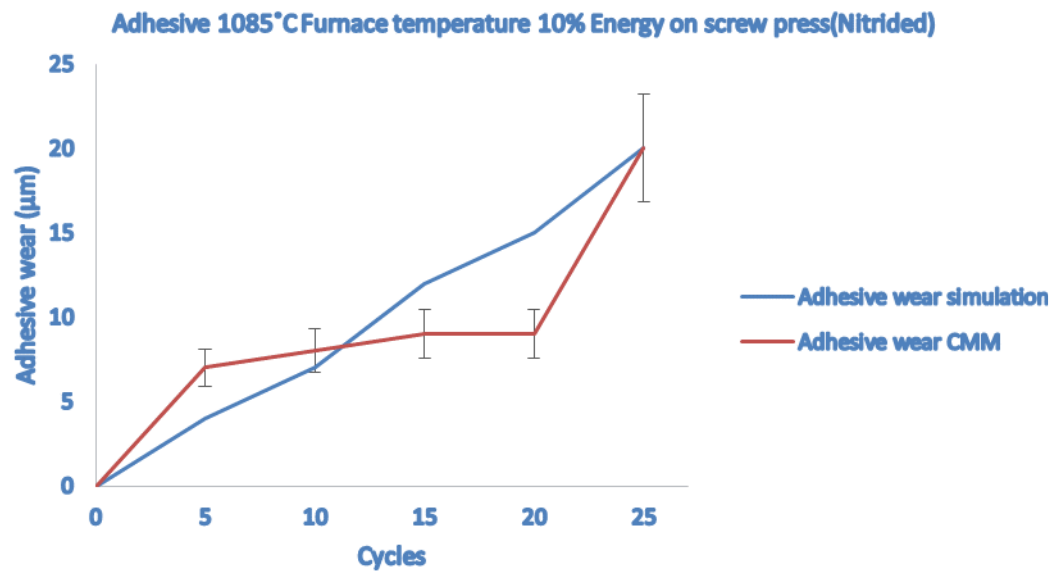
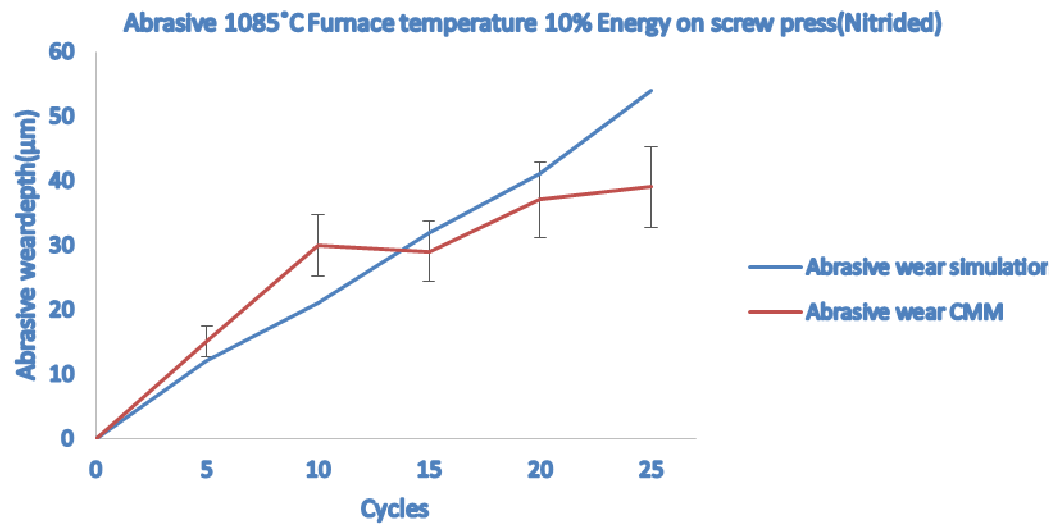


Figure 7-15. CMM measurement and simulation prediction comparison at 1085°C furnace temperature and 10 % of energy on screw press (16 KJ) for abrasive and adhesive wear (Nitrided tool)

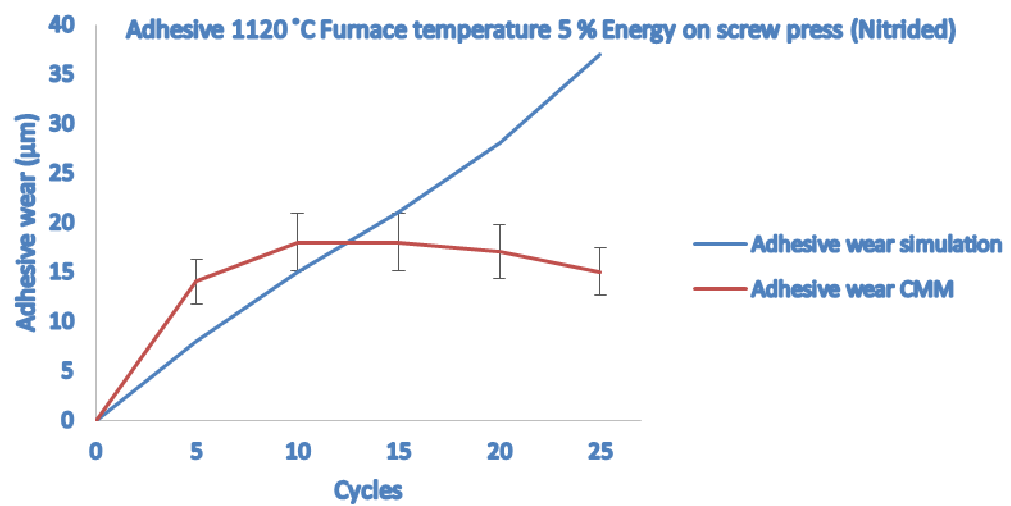
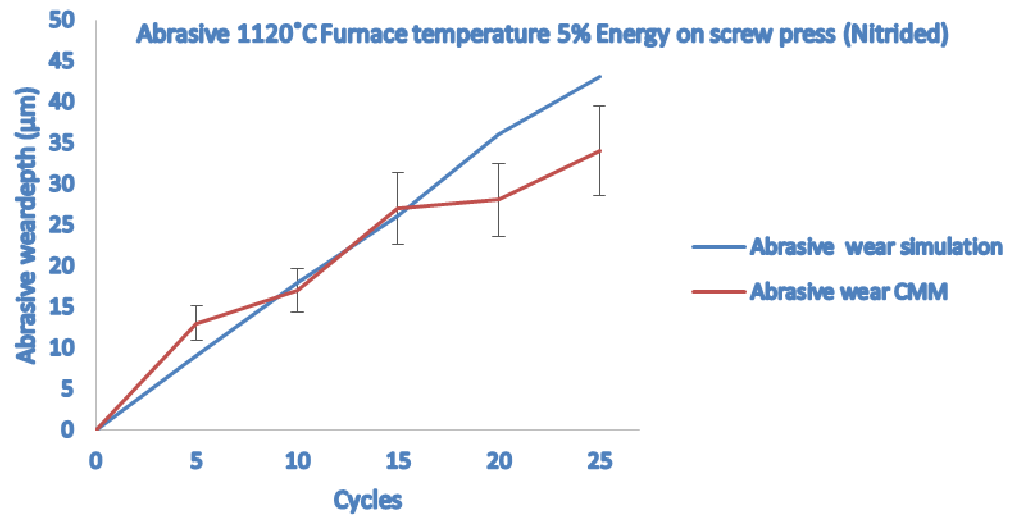


Figure 7-16. CMM measurement and simulation prediction comparison at 1120°C furnace temperature and 5 % of energy on screw press (8 KJ) for abrasive and adhesive wear (Nitrided tool)

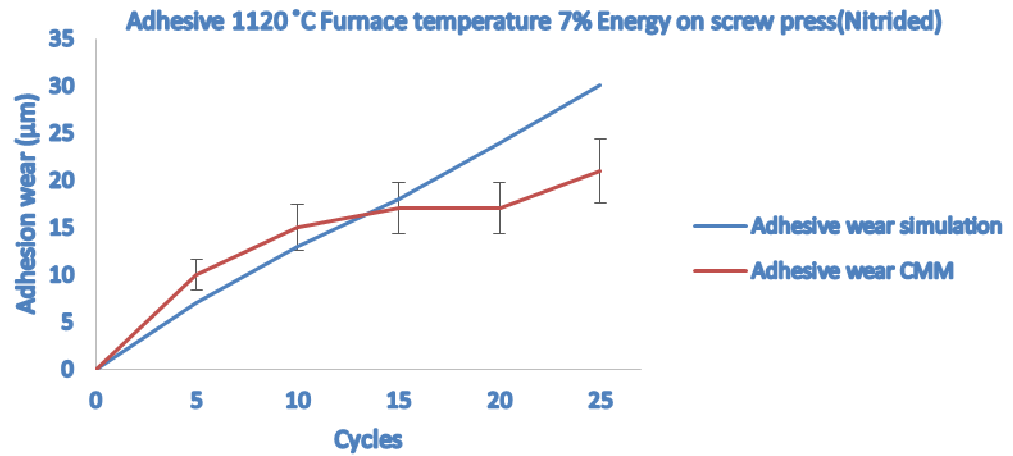
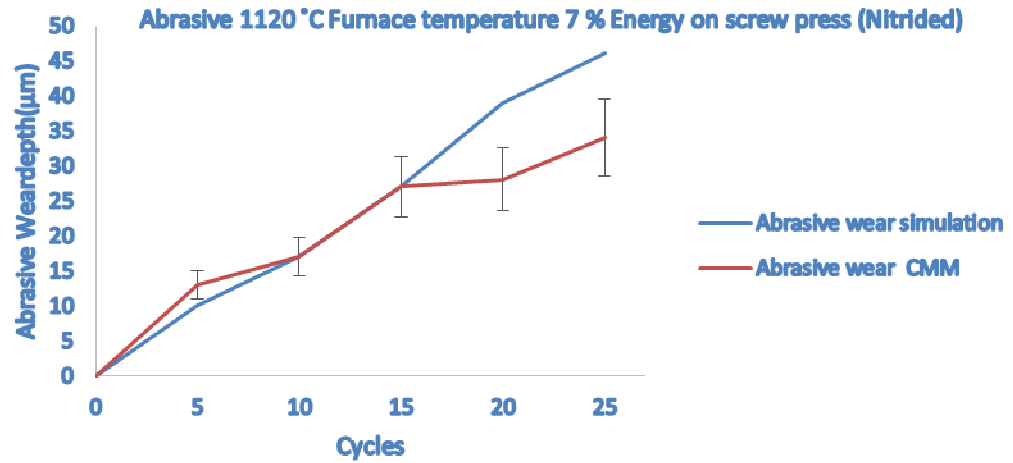


Figure 7-17. CMM measurement and simulation prediction comparison at 1120°C furnace temperature and 7 % of energy on screw press (11.2 KJ) for abrasive and adhesive wear (Nitrided tool)

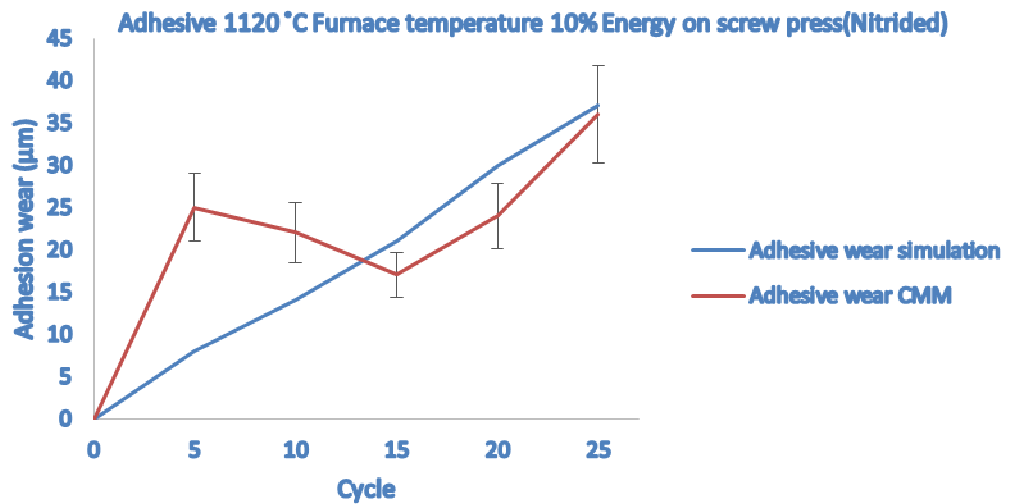
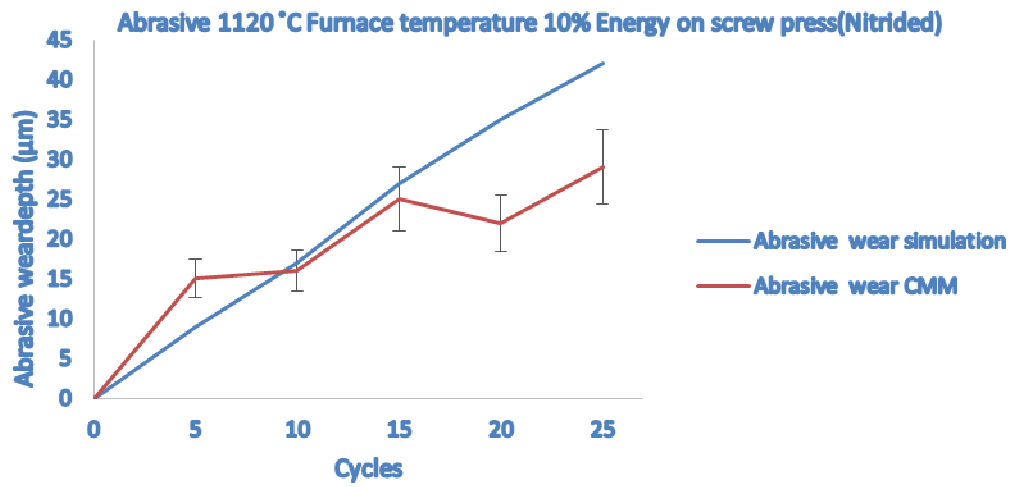


Figure 7-18. CMM measurement and simulation prediction comparison at 1120°C furnace temperature and 10 % of energy on screw press (16 KJ) for abrasive and adhesive wear (Nitrided tool)

7.3.Appendix C

7.3.1.Certificates of conformity and material data from the supplier




<p>GLASGOW SERVICE CENTRE 120 CANBUSLANG ROAD CANBUSLANG INVESTMENT PARK GLASGOW G32 8NB Telephone: 0141 6463730 Fax number: 0141 6418012</p> <p>Quotation prepared for 152904 UNIVERSITY OF STRATHCLYDE 85 INCHINNAN DRIVE RENFREWSHIRE</p> <p>PA4 9LJ</p>		<h1>RIGHTON</h1> <p>QUOTATION</p> <p>Page: 1 Our quotation no: 517275 Our reference . : 5427933 Date: 8/10/14 Your ref: ENQ JIM FOSTER</p> <p>Righton sales contact:- Martin Cowan</p>		
Qty	Item code	Description	Price	Extended
300 Each	79644	25MM 1.4541 ROUND BAR Lead Time: 5/7WDAYS SUPPLIED CUT TO SIZE : 50MM LONG	1.9500 Per Each	585.00
			Carriage Charges	25.00
			Sub Total	610.00
			VAT	122.00
			Total GBP	732.00
<p>Subject to market fluctuations & item availability Subject to our Standard Terms & Conditions of Sale</p>				
<p>Metals</p>  <p>aluminium stainless steel brass & bronze copper & copper nickel 17/4 PH, duplex & super duplex</p>		<p>Plastics</p>  <p>acrylic pvc foam polycarbonate aluminium composite sheet pet-g engineering plastics</p>		<p>Specialist suppliers to:</p> <p>marine naval & defence oil & gas aerospace</p> 
<p>Your Unbeatable Source For Metals & Plastics</p>				

Figure 7-19. Certificate of Conformity for Stainless steel 321

Stainless Steel (inc. High Performance) - 1.4541 / 321

Sheet 2B Finish

Properties

Stock		Chemical Properties	
Size (mm)	Weight/Sheet (kg)	Element	Chemical Composition %
2500 x 1250 x 0.9	24.00	Carbon (C)	0.08 max
2500 x 1250 x 1.2	23.50	Manganese (Mn)	2.00
2500 x 1000 x 1.5	30.00	Silicon (Si)	0.75
2500 x 1250 x 1.5	37.50	Phosphorus (P)	0.045
2500 x 1250 x 2.0	50.00	Sulphur (S)	0.03
2500 x 1250 x 2.5	62.50	Chromium (Cr)	17.0 - 19.0
2500 x 1250 x 3.0	75.00	Nickel (Ni)	9.0 - 12.0
		Nitrogen (N)	0.1
		Others	Ti+Cu+Hf min 0.70 max

Mechanical Properties	
Property	Value
Proof Stress	205 MPa min
Tensile Strength	515 MPa min
Elongation	40% min
Hardness Brinell	201 HB max

Physical Properties	
Property	Value
Density	7.9 g/cm ³
Modulus of Elasticity	200 N/mm ²
Thermal Conductivity	14.6 W/m.K
Specific Heat	500 J/g.K
Specific Electric Resistance	0.73 Ω.mm ^{2m}

Disclaimer

This data is indicative only and as such is not to be relied upon in place of the full specification. In particular, mechanical property requirements vary widely with temper, product and product dimensions. All information is based on our present knowledge and is given in good faith. No liability will be accepted by the Company in respect of any action taken by any third party in reliance thereon.

The information provided in this datasheet has been drawn from various recognised sources, including EN Standards, recognised industry references (printed & online) and manufacturer's data. No guarantee is given that the information is from the latest issue of those sources or about the accuracy of those sources.

Material supplied by the Company may vary significantly from this data, but will conform to all relevant and applicable standards.

As the products detailed may be used for a wide variety of purposes and as the Company has no control over their use, the Company specifically excludes all conditions or warranties expressed or implied by statute or otherwise as to dimensions, properties and/or fitness for any particular purpose, whether expressed or implied.

Advice given by the Company to any third party is given for that party's assistance only and without liability on the part of the Company. All transactions are subject to the Company's current Conditions of Sale. The extent of the Company's liabilities to any customer is clearly set out in those Conditions, a copy of which is available on request.

Figure 7-20. Stainless steel 321 material data from the supplier

CERTIFICATE OF CONFORMITY
Printed 29/02/16 13:11:10 Ref 05MC

ACCOUNT NO. 152904

UNIVERSITY OF STRATHCLYDE
ADVANCED FORMING RESEARCH CNTR
85 INCHINNAN DRIVE
INCHINNAN
RENFREW
PA4 9LJ

GLASGOW SERVICE CENTRE
0141 6463730

RIGHTON

GLASGOW SERVICE CENTRE
120
CAMBUSLANG ROAD
CAMBUSLANG INVESTMENT PARK
GLASGOW
G32 8NB
Tel: 0141 6463730
Fax: 0141 6418012
VAT Reg: GB 687 9071 77

CERTIFICATE NO: 5687319-00
PICK NOTE : 716290
CUST ORDER : NO 5013615
REQ SHIP DATE : 8/02/16
CARRIER : RIG Righton
CASH ON DELIV : NO
ORDER TYPE : CREDIT SALE
CONCESSIONS : NONE (UNLESS STATED)
EXPIRY OF MATL: INDEF (UNLESS STATED)

ITEM	REQD QTY	ORDER QTY	PICK QTY
905/5471553B 25MM DIA 718 INCONEL R/BAR 57 - Batch: 51777100/001 SUPPLIED CUT TO SIZE : 57.80 PER PIECE	57	57	57
	KG	LOT	LOT
		250 PCS @ 50MM LONG	

ADDITIONAL DETAIL (AS APPLIC):
SOURCES/WFS CERT REF NO.....:
MATERIAL CAST / HEAT NO.....:

SHIP TO:
UNIVERSITY OF STRATHCLYDE
ADVANCED FORMING RESEARCH CNTR
85 INCHINNAN DRIVE
INCHINNAN
RENFREW
PA4 9LJ

Certified that the supply of goods detailed hereon has been subject to our Quality System requirements in accordance with our ISO 9001 BSI Registration. Lot Traceable products are covered by the sources Certificate of Conformity or Test Certificate referenced hereon.

SIGNED: *Mark Cox*
DATE: 29/2/2016
PAGE: 1 FINAL

Registered in England No. 143811 Registered Office: 25 High Street, Chesham, Bucks HP11 3BQ

SUBJECT TO OUR TERMS AND CONDITIONS STATED OVERLEAF

Figure 7-21. Certificate of conformity for Inconel 718

Alloy 718 is a Nickel-Chromium based Superalloy

CHEMICAL COMPOSITION

Element	% Present
Nickel (Ni)	50.00 - 55.00
Chromium (Cr)	17.00 - 21.00
Niobium (Columbium) (Nb)	4.75 - 5.50
Molybdenum (Mo)	2.80 - 3.30
Aluminium (Al)	0.65 - 1.15
Copper (Cu)	0.20 - 0.80
Iron (Fe)	Balance

This details the main elements only

SUPPLIED FORMS

Please contact us with your requirements

CONTACT

Address:	Righton House Sraolyske Road Wilton Birmingham B6 7EY
Tel:	0121 356 1141
Fax:	0121 344 3210
Email:	marketing@righton.co.uk
Web:	http://www.righton.co.uk/

REVISION HISTORY

Datasheet Updated	15 January 2019
--------------------------	-----------------

DISCLAIMER

This Data is indicative only and as such is not to be relied upon in place of the full specification. In particular, mechanical property requirements vary widely with temper, product and product dimensions. All information is based on our present knowledge and is given in good faith. No liability will be accepted by the Company in respect of any action taken by any third party in reliance thereon.

Please note that the 'Datasheet Update' date shown above is no guarantee of accuracy or whether the datasheet is up to date.

The information provided in this datasheet has been drawn from various recognised sources, including EN Standards, recognised industry references (printed & online) and manufacturers' data. No guarantee is given that the information is from the latest issue of those sources or about the accuracy of those sources.

Material supplied by the Company may vary significantly from this data, but will conform to all relevant and applicable standards.

As the products detailed may be used for a wide variety of purposes and as the Company has no control over their use, the Company specifically excludes all conditions or warranties expressed or implied by statute or otherwise as to dimensions, properties and/or fitness for any particular purpose, whether expressed or implied.

Advice given by the Company to any third party is given for that party's assistance only and without liability on the part of the Company. All transactions are subject to the Company's current Conditions of Sale. The extent of the Company's liabilities to any customer is clearly set out in those Conditions; a copy of which is available on request.

[1 OF 1]

Figure 7-22. Inconel 718 Material data sheet from the supplier



BETA HEAT TREATMENTS LTD
 SUMMERTON ROAD, OLDBURY, WARLEY, WEST MIDLANDS, B69 2EL

Tel:0121 511 1190 Fax:0121 270 9605
 http://www.claytonholdings.com nw@claytonholdings.com

Customer Name
Cogne UK Ltd
 Uniformity Works
 Don Road
 Newhall
 Sheffield
 S9 2UD

CERTIFICATE OF CONFORMITY

Approval: C of C
 Certificate No: 25781,25782,25783,25784
 Date of Test: 20/09/2016
 Order No: w01-006609

Part No.	Dwg Iss.	Description of Process	Job No.	Qty	Weight	Material Spec	Batch ID / Serial No.
COGNE 52 - 54 HRC HARDEN & TEMPER 52/54 HRC COGNE BLOCKS	0	COGNE BLOCKS	0000026055	5	50	H13	L101-00 6608
100 70 x 45 mm							
COGNE 52 - 54 HRC HARDEN & TEMPER 52/54 HRC COGNE BLOCKS	0	COGNE BLOCKS	0000026054	20	510	H13	
122 x 132 x 202 mm							
COGNE 52 - 54 HRC HARDEN & TEMPER 52/54 HRC COGNE BLOCKS	0	COGNE BLOCKS	0000026053	12	306	H13	
122 x 132 x 202 mm = 12							
COGNE 52 - 54 HRC HARDEN & TEMPER 52/54 HRC COGNE BLOCKS	0	COGNE BLOCKS	0000026052	20	510	H13	
122 x 132 x 202 = 20							

TEST NAME	Lower Limit	Upper Limit
Rockwell HRC	52.0000	54.0000
52 _ _ _ _		
MD.DL		

Inspector(s)

Page 1 of 2
 FOOTER 2



Figure 7-23. Certificate of conformity for H13 Tool steel



COMPARABLE STANDARD

UNI	EURO NORM	W Nr	DIN	AFNOR	AISI/SAE	BS
X40CrMoV511KU	X40CrMoV511	1.2344	X40CrMoV51	Z40CDV5-1	H13	BH13

COMPOSITION

C	Si	Mn	Cr	Mo	V
0,40	1,0	0,4	5,2	1,4	1,0

CHARACTERISTICS OF THE PRODUCT

This steel grade can be obtained by the conventional process as well as electroslag remelting (ESR). The forging and thermal treatment practices produce a fine and homogeneous structure which guarantees characteristics of good machinability and good polishability during the manufacture of the die. After the thermal treatment, thanks to a more homogeneous distribution of Cr, Mo, V carbides, high levels of mechanical properties are reached, such as:

- high temperature mechanical strength (abrasion and compression)
- shock and thermal fatigue strength during the operation of the die.

This steel is characterized by good dimensional stability on thermal treatment, and is suitable for surface-hardening by nitriding.

PRODUCT APPLICATIONS

This steel, in view of its excellent range of characteristics, is particularly suitable for the manufacture of: - dies for die-casting of aluminium alloys, magnesium, etc. - dies and mandrels for the hot extrusion of aluminium alloys and steels - punches, dies, inserts for press-moulding, trimming tools, trimming shears, hot-shearing blades - moulds for plastic materials.

DELIVERY CONDITION

Annealed to HB ≤ 220.

HEAT TREATMENT

The steel is supplied in the annealed condition for optimum machinability, and after the rough-machining (+possible stress relieving) operations it is hardened and tempered to achieve the characteristics required by its applications.

Soft annealing: heating to 820 ± 860°C, holding at temperature, furnace cooling to 650°C (10°C hour), then cooling in stationary air.

Stress relieving: after rough-machining, heating to 600 ± 650°C, holding at temperature furnace cooling to 550°C, then cooling in stationary air.

Hardening: preheating to 700 ± 800°C, austenitization at 1000 ± 1030°C, air/oil-quenching or in thermal bath at 500 ± 550°C.

Tempering: heating to 540 ± 620°C, holding at temperature. Make at least 2 tempering treatments.

MECHANICAL CHARACTERISTICS

TEMP °C	180	200	300	400	500	600
DUREZZA HRC	55	55	54	54	56	48

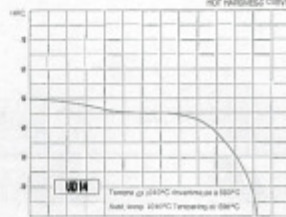
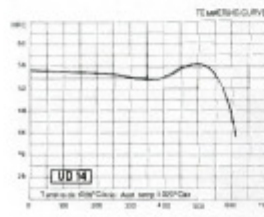


Figure 7-24. H13 Material data sheet from supplier